THE UNIVERSITY OF QUEENSLAND

AUSTRALIA

Microstructure Interpolation for Macroscopic Optimisation

Andrew Dale Cramer

BSc. MSc.

A thesis submitted for the degree of Doctor of Philosophy at The University of Queensland in 2017

School of Mathematics and Physics

Abstract

Recent advances in additive manufacturing now allow the physical construction of designs with features on the scale of tens of micrometres. It is impractical to design macroscopic objects with such feature sizes by hand, yet designs exploiting this new manufacturing ability can be produced through computational algorithms, such as with structural optimisation. While the computational ability of structural optimisation techniques is improving, the direct optimisation of a structure spanning two or more length scales is still difficult. Despite this, the new fine-scale manufacturing capability can be exploited using multiscale structural optimisation to find the best high resolution design for a particular application.

A multiscale design consists of microstructures which are repeatedly placed to create the design according to a macroscopic description. Previous work in multiscale optimisation has focused either on homogeneous microstructures that do not vary throughout the macroscopic design; analytically defined microstructures whose variation is well-known such as square lattices; or "top-down" multiscale design. In top-down multiscale design the macroscopic requirements at various locations prescribe the microstructural optimisation problems to be solved.

We seek to solve some of the issues associated with top-down multiscale designs while allowing

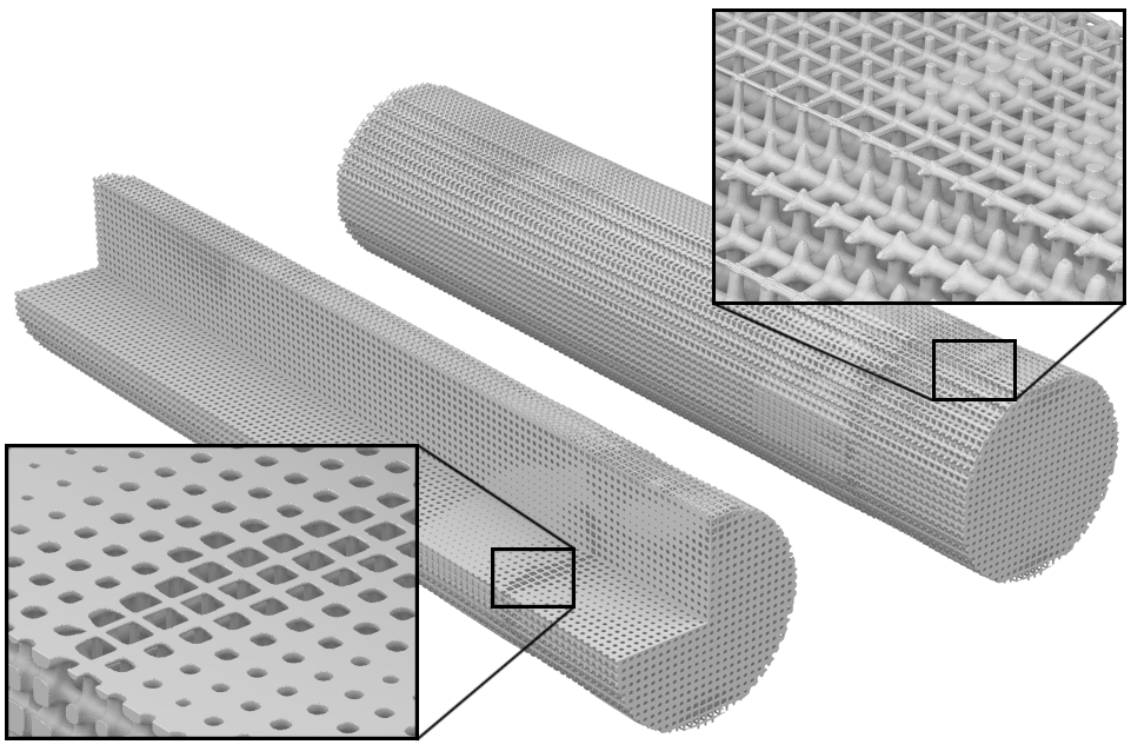

FIGURE 1: Interpolated microstructures are placed in a macroscopic domain to produce a two-scale design.

a wider space of microstructures than those that are analytically defined. We present a novel "bottom-up" method for multiscale structural optimisation over two length scales, which we call *microstructure interpolation for macroscopic optimisation* (MIMO). Shape interpolation, or morphing, between optimised microstructures produces a continuous set of microstructures that smoothly varies in both geometry and mechanical properties. The smooth set is used for macroscopic optimisation similar to the material distribution method (see Figure 1).

The output of any multiscale optimisation method must be transformed into a single unified description before a physical product can be manufactured. This transformation requires smooth transitions between the various microstructures to be well defined; the smoothness is assumed but not enforced in many existing top-down methods. The MIMO approach trades the generality of existing multiscale methods for a stronger unified interpretation: while the space of allowed microstructures is diminished compared to existing top-down methods, the microstructures vary smoothly throughout the design. This smoothness makes it clear how the microstructures can be transitioned between neighbouring macroscopic elements ensuring connectedness in the unified two-scale design. The MIMO method is also straightforward to apply to problems where a functionally graded material is desired.

In this thesis the MIMO method is developed and tested. We firstly perform shape interpolation between a number of elastically isotropic microstructures optimised for bulk modulus. They are parameterised by their volume fraction and vary in stiffness. The interpolated microstructures have smoothly varying effective macroscopic elastic properties close to the Hashin-Shtrikman bounds. These microstructures are then used in a number of 2D and 3D compliance minimisation problems. We find that the interpolated microstructures produce better objective values for 2D compliance problems than single-scale structural optimisation.

The MIMO method is then applied to the problem of minimising peak shear stress and bone resorption for femoral implants. Femoral implants are used in hip replacements, attaching the femur to the new hip socket. The intent of minimising the interface shear stress is to minimise the likelihood of mechanical failure of the interface between implant and bone. Applying the method of interpolated microstructures with a range of porous candidate microstructure families shows significant benefits over the use of unvarying microstructures for this optimisation problem. We also show that the choice of microstructure family is important, as is their orientation if the microstructure is anisotropic. A physical model is produced as a proof-of-concept, illustrating the feasibility of the method to produce manufacturable designs in 3D.

Finally, we generalise the MIMO method to use microstructures with a multi-dimensional parameterisation. Using multiple parameters allows spatial variation in the stiffness profile: the

stiffness in different directions may independently vary where before a sole parameter (the volume fraction) controlled all directions in concert. Here the Young's modulus in three orthogonal directions is used as the parameterisation. The femoral implant problem is revisited with this wider space of microstructures and the macroscopic optimisation is shown to make use of these new degrees of freedom.

MIMO is an efficient two-scale structural optimisation approach that allows tailoring of the microstructures for the problem at hand, and generates designs with a ready physical interpretation. It provides a broad search space with which to solve structural optimisation problems without forsaking practicality.

Declaration by Author

This thesis is composed of my original work, and contains no material previously published or written by another person except where due reference has been made in the text. I have clearly stated the contribution by others to jointly-authored works that I have included in my thesis.

I have clearly stated the contribution of others to my thesis as a whole, including statistical assistance, survey design, data analysis, significant technical procedures, professional editorial advice, and any other original research work used or reported in my thesis. The content of my thesis is the result of work I have carried out since the commencement of my research higher degree candidature and does not include a substantial part of work that has been submitted to qualify for the award of any other degree or diploma in any university or other tertiary institution. I have clearly stated which parts of my thesis, if any, have been submitted to qualify for another award.

I acknowledge that an electronic copy of my thesis must be lodged with the University Library and, subject to the policy and procedures of The University of Queensland, the thesis be made available for research and study in accordance with the Copyright Act 1968 unless a period of embargo has been approved by the Dean of the Graduate School.

I acknowledge that copyright of all material contained in my thesis resides with the copyright holder(s) of that material. Where appropriate I have obtained copyright permission from the copyright holder to reproduce material in this thesis.

Publications during candidature

Journal Articles

- Andrew D. Cramer, Vivien J. Challis, and Anthony P. Roberts. Microstructure interpolation for macroscopic design. *Structural and Multidisciplinary Optimization*, 53(3):489–500, 2016. doi: 10.1007/s00158-015-1344-7.
- Andrew D. Cramer, Vivien J. Challis, and Anthony P. Roberts. Physically Realisable Three Dimensional Bone Prosthesis Design with Interpolated Microstructures. *Journal of Biomechanical Engineering*. 139(3):031013, 2017. doi: 10.1115/1.4035481.

Conference Presentations

- Andrew D. Cramer. Microstructure Interpolation for Macroscopic Design. *The 51st ANZIAM Conference*, February, 2015.
- Andrew D. Cramer, Vivien J. Challis, and Anthony P. Roberts. Microstructure interpolation for macroscopic design with application to bone prosthetics. *11th World Congress of Structural and Multidisciplinary Optimization*, June, 2015.
- Andrew D. Cramer. Physically Realisable Three Dimensional Bone Prosthesis Design with Homogenised Microstructures. *The 52nd ANZIAM Conference*, February, 2016.

Publications included in this thesis

Publication 1

Andrew D. Cramer, Vivien J. Challis, and Anthony P. Roberts. Microstructure interpolation for macroscopic design. *Structural and Multidisciplinary Optimization*, 53(3):489–500, 2016. doi: 10.1007/s00158-015-1344-7.

The article is incorporated in Chapter 3.

A. D. Cramer	concept 30%, code developement 100%, running computations 100%, writing 90%
V. J. Challis	concept 35%, writing 10%
A. P. Roberts	concept 35%

Publication 2

Andrew D. Cramer, Vivien J. Challis, and Anthony P. Roberts. Physically Realisable Three Dimensional Bone Prosthesis Design with Interpolated Microstructures. *Journal of Biomechanical Engineering*. 139(3):031013, 2017. doi: 10.1115/1.4035481.

The article is incorporated in Chapter 4.

A. D. Cramer	concept 30%, code developement 100%, running computations 100%, writing 100%
V. J. Challis	concept 35%
A. P. Roberts	concept 35%

Contributions by others to the thesis

No contributions by others.

Statement of parts of the thesis submitted to qualify for the award of another degree

None.

Acknowledgements

Thanks go first to my two supervisors, Anthony Roberts and Vivien Challis. I am deeply grateful for the advice and help you both have given me. Tony, your eye on both the destination and applications helped me see the value in my work when I could not. Your enthusiasm for those broad connections encourages me and gives me confidence that this work was worth it. Viv, your technical help and advice cut short hours of searching and frustration. I laugh thinking of the many times the solution became self evident immediately after I sat down with you and explained the problem.

To my beloved, Rachel. Thank you for your continued, unwavering support. I'm truly blessed to have you at my side in this crazy journey. I hope I can love and support you, as you have me, along whatever path we take next.

Thank you Mum, Dad, and the rest of my family. Thanks for your love and care over all my years. I couldn't wish for a better family and I'm thankful for all you have taught me.

To Seb, you are by far my longest academic friend. Thanks for your encouragement, your chats and practical advice; whether about the maths or about the mechanics. Thanks also to all the others that I've shared offices and research groups with, in particular Kiran and Rob for making a bit of noise in 07-219. There's nothing like a few people sharing the experience to keep you going.

Finally, thank you my God. I don't understand your thoughts nor your plans. But thanks for holding on when I cannot.

Keywords

Structural optimisation, homogenisation method, interpolated microstructure, prosthesis design.

Australian and New Zealand Standard Research Classifications (ANZSRC)

ANZSRC code: 010207	Theoretical and Applied Mechanics	(50%)
ANZSRC code: 010303	Optimisation	(50%)

Fields of Research (FoR) Classification

FoR code: 0102	Applied Mathematics	(50%)
FoR code: 0103	Numerical and Computational Mathematics	(50%)

Contents

List of Figures xiii

List of Tables xv

List of Abbreviations xvii

1 Introduction 1
- 1.1 Classical Approaches to Structural Optimisation . . . 2
  - 1.1.1 Overview . . . 2
  - 1.1.2 The material distribution method and SIMP . . . 3
  - 1.1.3 Inverse Homogenisation . . . 4
- 1.2 Microstructures and Macroscopic Designs . . . 5
  - 1.2.1 Functionally graded materials . . . 5
  - 1.2.2 Multiscale structural optimisation . . . 6
  - 1.2.3 A New Method for Multiscale Optimisation . . . 8
- 1.3 Thesis Overview . . . 10

2 Background 13
- 2.1 Derivation of Linear Elasticity . . . 13
  - 2.1.1 Strain . . . 13
  - 2.1.2 Stress . . . 16
  - 2.1.3 The constitutive equation . . . 17
  - 2.1.4 Variational solution . . . 20
  - 2.1.5 Numerical solution . . . 21
- 2.2 Homogenisation of periodic microstructures . . . 23
- 2.3 The SIMP Method . . . 25
  - 2.3.1 Method description . . . 27
  - 2.3.2 Derivatives . . . 29
- 2.4 The Level Set Method . . . 29

3 Single Parameter Microstructure Interpolation 35
- 3.1 Introduction . . . 35
- 3.2 Development of Interpolated Microstructures . . . 37
  - 3.2.1 Optimisation of key microstructures . . . 37
  - 3.2.2 Microstructure interpolation . . . 39
  - 3.2.3 Microstructure evaluation . . . 40
- 3.3 Macroscopic Design Examples . . . 44
  - 3.3.1 Method . . . 44

3.3.2 Results . . . 46
3.4 Discussion . . . 46
3.4.1 Evaluation of MIMO designs . . . 46
3.4.2 Advantages of the MIMO approach . . . 55
3.4.3 MIMO applications and extensions . . . 56
3.5 Conclusion . . . 57

4 Application to Bone Prosthesis Design 59
4.1 Introduction . . . 59
4.2 Methods . . . 61
4.2.1 Microstructures . . . 61
4.2.2 Problem Domain . . . 65
4.2.3 Shear stress objective . . . 66
4.2.4 Resorption constraint . . . 67
4.2.5 Numerical and optimisation details . . . 68
4.3 Results and Discussion . . . 71
4.4 Conclusion . . . 73

5 Multiparametric Microstructure Interpolation 79
5.1 Introduction . . . 79
5.2 Microstructures . . . 80
5.2.1 Parameterisation . . . 80
5.2.2 Generation of key microstructures . . . 84
5.2.3 Microstructure interpolation . . . 87
5.2.4 Results . . . 89
5.3 Macroscopic Optimisation . . . 91
5.3.1 Optimisation problem . . . 92
5.3.2 Filling the microstructural space . . . 93
5.3.3 Other microstructural details . . . 94
5.4 Results and discussion . . . 97
5.5 Application to FGMs . . . 104
5.6 Conclusion . . . 105

6 Conclusion 109
6.1 Single Parameter Microstructure Interpolation . . . 109
6.2 Application to Bone Prosthetic Design . . . 110
6.3 Multiparametric Microstructure Interpolation . . . 111
6.4 Final Discussion . . . 112

Bibliography 115

List of Figures

1 Interpolated microstructures in a macroscopic design ii

1.1 A basic structural optimisation example 1
1.2 Homogenisation and inverse homogenisation illustration 4
1.3 Example of a functionally graded meta-material (Zhou and Li, 2008a) 6
1.4 A multiscale structural optimisation solution (Rodrigues et al., 2002) 7
1.5 Using microstructure interpolation for macroscopic design 9

2.1 Lagrangian specification of a flow field 14
2.2 Displacement field decomposition 15
2.3 Illustration of principal strains 16
2.4 Strain tensor derivation tetrahedron 17
2.5 Strain energy derivation hexahedron 18
2.6 Bilinear shape function example 22
2.7 SIMP optimisation example 26
2.8 SIMP heuristic illustration 28
2.9 Example of a level set function 30
2.10 A moving boundary represented as a level set in one dimension 32

3.1 Density to microstructure map illustration 36
3.2 One-dimensional boundary interpolation 39
3.3 Two-dimensional boundary interpolation 39
3.4 Microstructure interpolation example 41
3.5 Interpolated microstructure and Hashin-Shtrikman bounds comparison 41
3.6 Interpolated microstructure anisotropy 42
3.7 Interpolated microstructure property fitting 42
3.8 Schematics of the 2D macroscopic optimisation problems 47
3.9 Schematics of the 3D macroscopic optimisation problems 48
3.10 Optimised designs for the 2D problems 49
3.11 Optimised designs for the 3D bridge problems 50
3.12 Optimised designs for the 3D cantilever problems 51
3.13 Optimised compliance objective values for each test problem 53
3.14 Proportions of elements grouped by density 54

4.1 Visualisation of the microstructure sets used 62
4.2 Microstructure properties over varying volume fractions 64
4.3 Schematics of the domain used for the femoral implant problem 65
4.4 Prosthetic designs displaying volume fraction 70
4.5 Optimisation history for macroscopic optimisations 72

4.6 Stress distributions across the interface Π . . . 74
4.7 Shear stress averaged on circles around the interface surface Π . . . 75
4.8 Final design visualisations . . . 76
4.9 Final design prototype . . . 77

5.1 Two-dimensional directional dependence of Young's modulus . . . 82
5.2 Three-dimensional Young's modulus directional dependence . . . 84
5.3 Initial microstructure for the key microstructure optimisations . . . 85
5.4 Anisotropic key microstructure parameter space connectivity . . . 86
5.5 Trilinear interpolation neighbourhood . . . 88
5.6 Obtained microstructure parameter space . . . 90
5.7 Some of the optimised microstructures . . . 91
5.8 Error in interpolated effective material properties . . . 92
5.9 Example of an orthotropic cross structure (microstructure set F) . . . 95
5.10 Visual comparison of objective values of the new designs and the old . . . 96
5.11 Macroscopic design using microstructure set E with penalty . . . 99
5.12 Macroscopic design using microstructure set E without penalty . . . 100
5.13 Macroscopic design using microstructure set F axially aligned . . . 101
5.14 Macroscopic design using microstructure set F rotated . . . 102
5.15 Multiparametric design illustration . . . 103
5.16 Zoomed design showing slow and rapid variation . . . 103
5.17 A functionally graded design example . . . 105
5.18 Parameter set used for the functionally graded example . . . 106
5.19 Render of the functionally graded design example . . . 107

List of Tables

3.1 Compliance objective values 52

4.1 Descriptions of the four sets of microstructures considered 61
4.2 Objective and constraint results for $m = 1$ 69
4.3 Objective and constraint results for $m = 2$ 69

5.1 Macroscopic optimisation results, $m = 1$ 97
5.2 Macroscopic optimisation results, $m = 2$ 97

List of Abbreviations

CT	Computed Tomography
ESO	Evolutionary Structural Optimisation
FEA	Finite Element Analysis
FGM	Functionally Graded Material
GCMMA	Globally Convergent Method of Moving Asymptotes
GPU	Graphics Processing Unit
MIMO	Microstructure Interpolation for Macroscopic Optimisation
MMA	Method of Moving Asymptotes
RVE	Representative Volume Element
SIMP	Solid Isotropic Material with Penalisation
SLM	Selective Laser Melting
THR	Total Hip Replacement

Chapter 1

Introduction

Structural optimisation is the field concerned with designing the layout of a structure in order to optimise its physical properties in some way (Bendsøe and Sigmund, 2003). An example of such a design can be seen in Fig. 1.1, where the stiffness has been optimised subject to a vertical load on the right side with an immovable edge on the left and a specified maximum weight. Structural optimisation is an important and practical field, it can provide improvements in efficiency and economy giving important benefits to real engineering applications. For an example from industry, Airbus estimated that they saved approximately 1000kg on the A380 aeroplane using structural optimisation (Krog et al., 2004). This weight saving translates into significant cost reductions in fuel considering the service life and distance travelled of all A380 aeroplanes that have and will be produced.

In this introductory chapter we review the relevant literature. This includes the general field of structural optimisation, inverse homogenisation, functionally graded materials, and multiscale structural optimisation. At the end of the chapter an outline of the thesis is given, to guide the reader through the rest of the document.

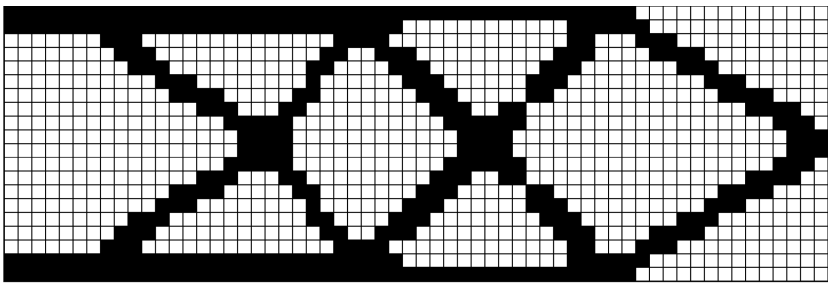

FIGURE 1.1: A basic structural optimisation example. The left edge is fixed (zero displacement) while a vertical load is applied in the centre of the right side. The layout of material, subject to a volume constraint, is then optimised for overall stiffness.

1.1 Classical Approaches to Structural Optimisation

Structural optimisation has a rich history. Rozvany (2001), Munk et al. (2015), and Bendsøe and Sigmund (2003) give a good overview of the field and its development. We briefly cover that history here.

1.1.1 Overview

Michell solved one of the earliest structural optimisation problems finding conditions on the layout of a frame of struts and ties to achieve the lightest possible result given allowed stresses (Michell, 1904). He found that in order to minimise the weight, frames should have their elements meet at right angles. Since this seminal article, much work has been done in the field examining a variety of methods and descriptions including frames, planar sections, plates and continuous structures (Bendsøe and Sigmund, 2003; Munk et al., 2015). Of interest to the ideas described in this thesis is the relatively general continuum optimisation problem which has been approached in a number of ways, including: with pure shape optimisation; a relaxed formulation with the material distribution method; heuristic evolution with evolutionary structural optimisation; and using level-set methods to describe and evolve designs.

In pure shape optimisation the boundary of the structure is parameterised and then optimised (e.g. Haftka and Grandhi, 1986). The method can be computationally expensive as at each stage a new mesh must be generated. In addition, topology changes can be difficult or impossible. Shape optimisation doesn't suffer from mesh influence and dependency as much as other methods however, and methods have been developed to allow changes in topology in shape optimisation (e.g. Eschenauer et al., 1994).

Evolutionary structural optimisation (ESO) optimises by removing material elements from the structure (and adding in the case of the bidirectional ESO) (Xie and Steven, 1993; Querin et al., 1998). Elements are removed when they are inefficient, with the quantification of efficiency depending on the problem. For example, in the case of stress minimisation, efficiency may in some cases be determined with the von Mises stress (Xie and Steven, 1994; Munk et al., 2015), so elements that are transferring less stress are removed while those transferring more stress are retained.

Level set methods are similar to shape optimisation methods, however instead of directly describing the surface it is implicitly determined from the level set of a control function (called a level-set function) (Sethian and Weigmann, 2000; Osher and Santosa, 2001; Wang et al., 2003; Allaire et al., 2004). A surface velocity is then determined that, when followed, optimises the

objective. This velocity is then used to evolve the control function. Hole nucleation is an issue in two dimensions, similar to shape optimisation, as forming a void inside a two dimensional object by continuous deformation would require a disconnection. While methods exist to counter this problem (e.g. Hackl, 2007), in three dimensions, which is arguably of more interest, topology changes happen naturally with the level set method (Allaire et al., 2004; Allaire and Jouve, 2005).

The material distribution method is of greatest concern here as it is the method that this thesis builds upon. As such, its development is covered in more detail in the following section, and the method itself is discussed in detail in Section 2.3. We also describe inverse homogenisation here as it forms an integral part of the basis for the thesis.

1.1.2 The material distribution method and SIMP

The material distribution method is an approach for optimising a structure where instead of allowing only solid material and void, the problem is relaxed to allow some sort of parameterised material. The structure is then described by the distribution of this meta-material allowing intermediate densities. Bendsøe and Kikuchi (1988) first used a square micro-lattice with varying volume fraction to maximise a macroscopic structure's stiffness with a material volume constraint. They found that the majority of the domain consisted of either the maximum or the minimum volume fraction.

As the microstructure was not widely used in the final solution, the square lattice used could be replaced with a simpler elastic law for a fictitious material so long as intermediate densities were sufficiently 'penalised' (Bendsøe, 1989; Rozvany et al., 1992). In particular, this led to the now commonly used material law called *solid isotropic material with penalisation* (SIMP) by Rozvany et al. (1992):

$$C_{ijkl}(\rho) = \rho^P C^0_{ijkl}, \tag{1.1}$$

where $\rho \in [0, 1]$ is the 'density' of material, and C^0_{ijkl} is the base material's stiffness tensor. So long as the exponent P is chosen to be high, areas of intermediate density are inefficient and optimal solutions consist only of solid and void (Rozvany et al., 1992). The material law is considered fictitious as there may not be a material that satisfies the relation. As the density map is only an intermediary to obtain a solid and void design, the lack of physical interpretation does not invalidate the method. Bendsøe and Sigmund (1999) did however show that for P large enough, microstructures consisting of ranked laminates exist that follow (1.1), thus physically justifying such a law.

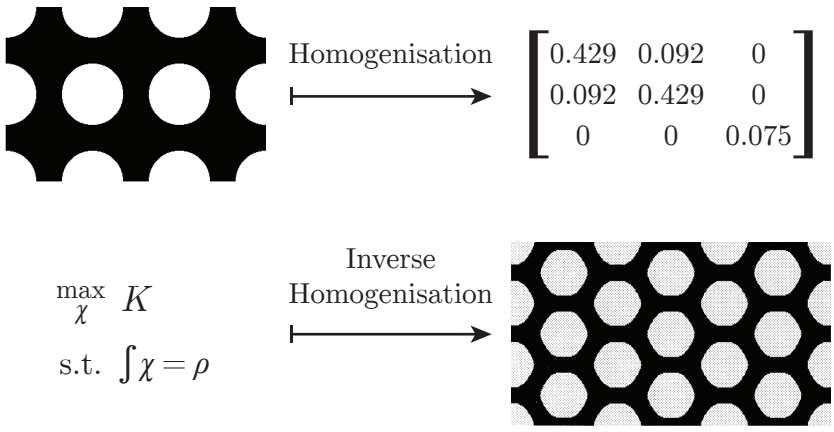

FIGURE 1.2: Homogenisation takes a microstructure and determines its effective material properties, such as its stiffness tensor (here displayed using Voigt's 3×3 notation). Inverse homogenisation either takes target effective properties and produces a matching microstructure, or optimises a microstructure for an effective property. The optimised microstructure above was found by Vigdergauz (1999), this image is a replication using inverse homogenisation (reproduced from Sigmund, 2000).

1.1.3 Inverse Homogenisation

Microstructures are structures on a much smaller length scale than the object that they are a part of. Microstructures include wood grain, metallic crystal grains and cement: all of these have details on a fine length scale, but are considered homogeneous in most macroscopic applications. Microstructures can be random, periodic, or quasi-periodic — where the deviation from a true periodic structure is over a larger length scale than the microstructures themselves. Homogenisation takes the description of a microstructure and determines 'bulk' or effective properties for how the material composed of such microstructures would behave.

Inverse homogenisation reverses this process: starting with effective properties, inverse homogenisation aims to find a periodic microstructure that would produce those properties (Fig. 1.2). Sigmund (1994) developed an inverse homogenisation method to construct two dimensional examples of extremal materials with negative Poisson's ratio and materials with zero eigen-values. Methods to optimise both continuum microstructure descriptions and microstructures described by a set of trusses and ties were developed. While the truss description naturally has a continuous nature, the continuum optimisation was relaxed and the base material had a continuously variable Young's modulus (or equivalently, plate thickness). The method was demonstrated to work in three dimensions by Sigmund (1995) using just the truss description, and some macroscopic examples were physically produced and tested. Sigmund

(1997) optimised continuum structures for thermoelastic expansion, making use of three material phases and a continuum description. Since then inverse homogenisation has been extended to optimise for many objectives and constraints including, for example, fluid permeability objectives (Guest and Prévost, 2006), and elastic isotropy constraints (Challis et al., 2008a). The work of Challis et al. (2008a) is also interesting due to the use of the level-set method to produce a continuum microstructure description. Zhou et al. (2011) extended the use of level-set methods to optimise a microstructure for negative electromagnetic permeability.

Inverse homogenisation allows the design of meta-materials with prescribed or optimised effective elastic properties. Once one can optimise a microstructure for effective elastic properties through inverse homogenisation, it is natural to want to optimise the use of microstructures continuously within a macroscopic domain.

1.2 Microstructures and Macroscopic Designs

This thesis is concerned with developing a method to intelligently combine macroscopic design and microstructure optimisation to facilitate the optimisation of macroscopic designs with fine-scale features. Zheng et al. (2014) have shown that it is possible to manufacture structures with feature sizes on the order of 10μm. Macroscopic objects with such a small minimum feature size are computationally infeasible to optimise directly — multiscale structures allow the exploitation of the new possibilities provided by additive manufacture. Efforts towards this combination of design scales can be broadly categorised into two areas: functionally graded materials, and multiscale optimisation. We extend this literature, presenting a new multiscale design approach.

1.2.1 Functionally graded materials

A *functionally graded material* (FGM) is a material whose properties change over a finite distance. Niino and Maeda (1990) for example examined the use of FGMs for handling very high thermal gradients in space-planes and the associated thermal stresses. Dunning et al. (2014) investigated FGMs for use in aircraft wings and found that being able to vary material properties along with the geometry benefited the aero-elastic performance. An overview of FGM optimisation can be found in Birman and Byrd (2007) along with an overview of the field in general.

Designing microstructures and thus designing meta-materials is a method that can be used for generating FGMs. Zhou and Li (2008a,b), for example, used structural optimisation to do just

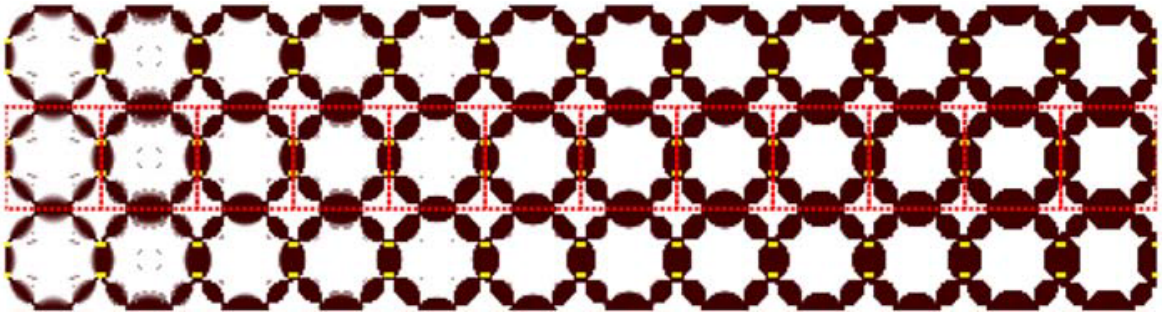

FIGURE 1.3: Example of a functionally graded meta-material (reproduced from Zhou and Li, 2008a). The dashed red squares indicate representative unit cells. The small yellow rectangles mark connections prescribed by pseudo-loads that ensure connectivity.

this, making a series of microstructures with a prescribed changing Young's modulus. Chief among Zhou and Li's concerns were the connectivity of the microstructures. They tested three methods for ensuring connectivity. The first method was simply to specify the connections between microstructures as a constraint to the optimisation, while the second was similar, supplying extra loading conditions at points called "pseudo-loads" (Fig. 1.3). Of course such methods reduce the allowed search space by presupposing the microstructure connections. The second method considered added a diffusion term to the optimisation where the diffusion was considered through all microstructures chained together. This method had the benefits that it did not prescribe the connections before the optimisation and that it also suppressed checkerboarding, a problem common to structural optimisation on a regular mesh. The diffusion method is only valid however for an FGM that varies the microstructures along one dimension only. More recently, Radman et al. (2013) ensured connectivity of base cells in an FGM by optimising each cell considering its two neighbours. When optimising cell j the cells $j-1$ and $j+1$ were considered with their sensitivities 'bleeding' into cell j through a sensitivity filter.

1.2.2 Multiscale structural optimisation

Multiscale optimisation forsakes a monolithic design approach for a multiscale description, having detail on a macroscopic level and also on the microscopic while optimising both. Multiscale structural optimisation is related to FGM design: both determine microstructures varying throughout a macroscopic domain. Instead of prescribing a functional gradient however, in multiscale structural optimisation the desired effective microstructural properties are determined through a macroscopic optimisation. An example of one such method is shown in Fig. 1.4. The methods allow the optimisation of two-scale designs on both scales simultaneously to best make use of new manufacturing capabilities.

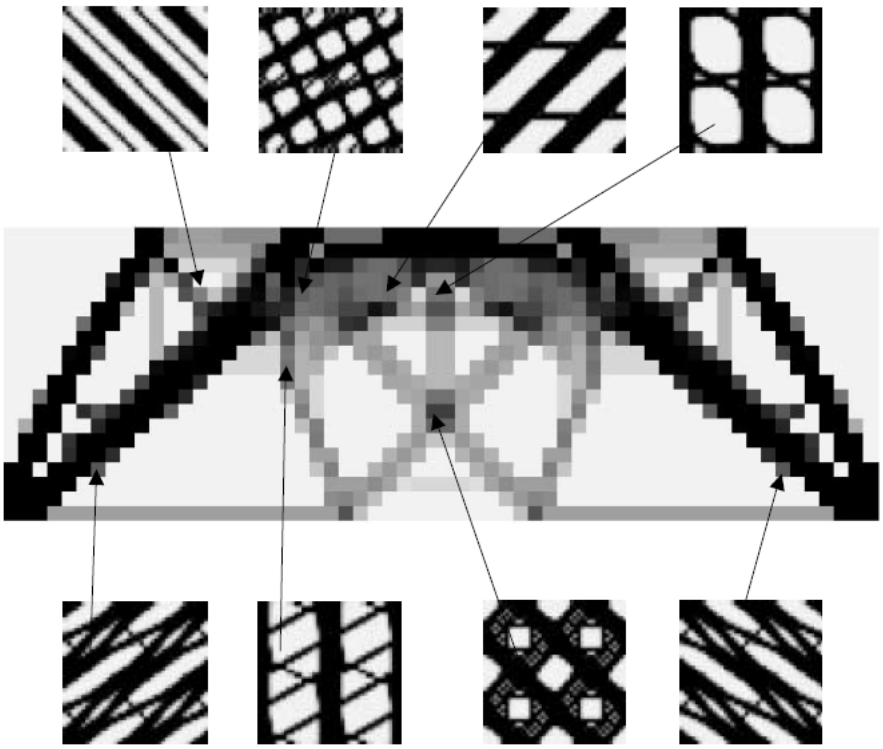

FIGURE 1.4: A multiscale structural optimisation solution (reproduced from Rodrigues et al., 2002). For each element in the design a microstructure is optimised. Four microstructure unit cells are shown for some example elements.

Early work in multiscale structural optimisation included that of Jog et al. (1994), who optimised a multiscale design consisting of rank-2 laminate microstructures where the layers were able to vary in material volume fraction throughout the macroscopic domain. While the overall microstructure could rotate, the individual layers were orthogonal to each other. One problem of ranked laminate microstructures is that they are difficult to produce due to their multiple length scales. With rank-2 laminates there are three length scales, the macroscopic, the first rank and the second.

Rodrigues et al. (2002) developed a method whereby a macroscopic structure could be optimised, consisting of general, single-scale microstructures. In this method, optimality criteria were found for the macroscopic design problem and the microscopic design problem. From the optimality criteria an update scheme was derived. The method was computationally feasible thanks to the decoupling of the micro-optimisation from the macro-optimisation, facilitating the use of parallel computation. Coelho et al. (2008) extended the work to three dimensions, again using optimality criteria.

During the development of this thesis, Sivapuram et al. (2016) have developed another method for full multiscale structural optimisation. They linearised the objective and constraints to

formulate a new way of decomposing the macroscopic and microscale design problems that allows parallelisation of the computations. Their approach can be generalised to any multiscale structural optimisation problem, which is in contrast to an optimality criteria approach which requires development of a suitable heuristic update scheme for the particular problem at hand. Also recently, Li et al. (2016) optimised the macroscopic density with a tentative SIMP-like law before optimising the microstructures with the level set method. Their focus was on developing multi-layered, functionally graded cellular materials.

1.2.3 A New Method for Multiscale Optimisation

While multiscale optimisation extends the complexity of allowed designs, manufacturability of the final design is typically not ensured. In particular, the connectivity of the geometry across neighbouring microstructures must be addressed as it has been with FGMs before multiscale designs may be built. For example, it is not clear how the microstructures in Fig. 1.4 connect and transition smoothly. Without resolving this issue a physical object cannot be produced and the designs produced by the method remain theoretical.

Recently, there has been some work trying to address such concerns in multiscale optimisation, for example, Deng et al. (2013) used a single microstructure geometry optimised concurrently with a macroscopic layout optimisation. As a single microstructure is used throughout the solid domain the connectivity problem is removed. Another example, developed concurrently to this thesis, is provided by Wang et al. (2016), who approached the problem by using a single control function whose level sets describe a set of microstructures. Both the control function and the macroscopic distribution were simultaneously optimised. While the microstructures were allowed to vary throughout the domain, the set of microstructures was restricted to those sets that can be described by a single control function.

Here, a method is developed that we have termed *microstructure interpolation for macroscopic optimisation* (MIMO). The MIMO method developed, tested and expanded in this thesis looks to solve the connectivity problem of two-scale designs by a return to the material distribution method combined with microstructures optimised prior to the macroscopic optimisation. Inverse homogenisation may only optimise a finite number of microstructures however, and so the method proposed combines similar microstructures with shape interpolation to provide a smooth continuum of microstructure possibilities (Fig. 1.5). It is a "bottom-up" design method whereby the microscopic scale provides options for the macroscopic scale optimisation, rather than a "top-down" design method where the macroscopic scale informs the microscopic optimisation. It trades the wide generality of the hierarchical method by Rodrigues et al. (2002), for surety of manufacture and a greater ability to hand-tailor the microstructures.

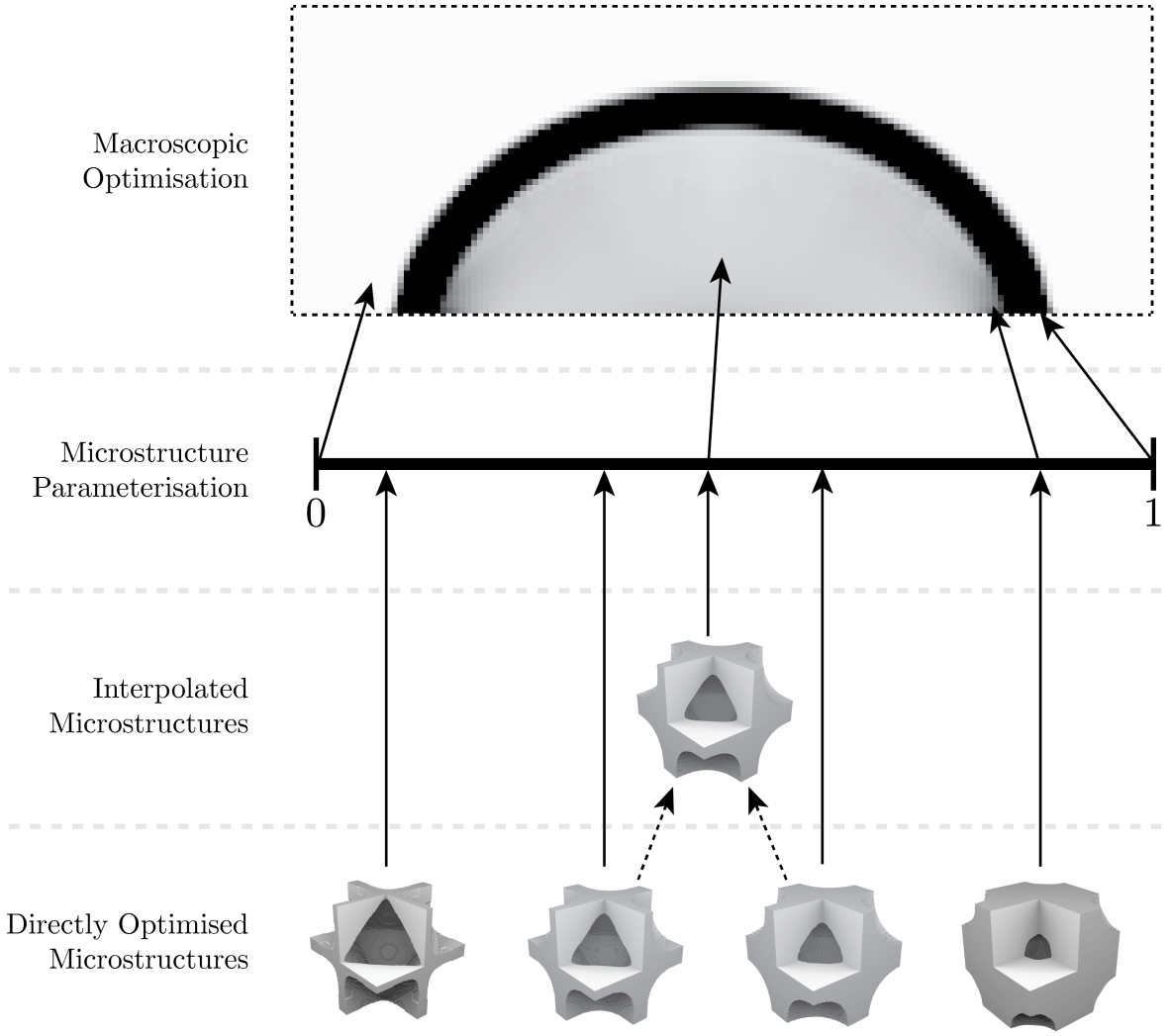

FIGURE 1.5: Illustration of using microstructure interpolation for macroscopic design (MIMO). Starting from the bottom: a discrete set of microstructures are optimised. These optimised microstructures are then interpolated between to produce a smoothly changing set of microstructures. The smoothly changing set of microstructures are parameterised and used in a macroscopic design optimisation. Figure is a schematic only.

The microstructure sets developed are parameterised in some way (e.g. by density). A vector field then maps locations in the macroscopic design domain to points in the microstructure parameter space, and thus to material properties for that location. If the design vector field is continuous and the microstructures are ensured to vary smoothly throughout the parameterisation, then the final design will have smooth and well defined geometry on all length scales. The smoothly changing geometry ensures connectivity of the microstructure unit cells addressing the need for physically interpretable multiscale designs.

By interpolating microstructure geometries the smoothness required is obtained while still allowing structures without closed form descriptions. It allows not only the square lattice of Bendsøe and Kikuchi (1988) that has a closed form description but also optimised microstructures, such as the extremal microstructures found by Sigmund (2000). As an added benefit the method is very efficient requiring no homogenisation calculations simultaneous to the macroscopic optimisation.

1.3 Thesis Overview

In Chapter 2 the mathematical background for the thesis will be reviewed. The derivation of the linear elastic equations is shown, along with the numerical method used to solve them here. Microstructure homogenisation for periodic microstructures is reviewed and some structural optimisation techniques are shown in more detail.

In Chapter 3 the MIMO method is developed and tested on compliance problems. Microstructures are restricted to be elastically isotropic, varying in only one parameter: density. Restricting ourselves to one dimension allows easy conceptualisation and evaluation of the microstructure set which is shown to be smooth not just in geometry, but also in material properties. It is shown that the method provides strong benefits in two dimensional compliance problems with small improvements in three dimensions.

Chapter 4 discusses the use of the MIMO method in bone prosthetic design for a hip replacement. The bone prostheses connect the remaining femur with the new hip joint and are called femoral implants. Work has been done in optimising the femoral implants to minimise the peak shear stress in the bone-prosthesis interface while reducing the adverse effect of bone resorption. Applying the MIMO method to this problem demonstrates improvements over homogeneous designs, validating the work of Kuiper and Huiskes (1997) and extending that of Arabnejad Khanoki and Pasini (2012), Chanda et al. (2015a), and others. A proof of concept model is also produced using additive manufacturing.

The use of multiparametric microstructure sets within the MIMO method is investigated in Chapter 5. A number of problems arise when the parameterisation is extended to multiple dimensions. The larger space of microstructures requires orders of magnitude more microstructures to be directly optimised in order to provide a basis for the microstructure interpolation. In addition, the space of allowed microstructures ceases to be a single dimensional interval and becomes a general shape in a higher dimension causing the limits of one parameter to be a function of the other parameters. These issues are addressed, and the optimised set is applied to the bone prosthesis problem investigated in Chapter 4. Some surprising results show that

the larger optimisation space may be difficult for the optimisation algorithm to manage. We also show how such a microstructure set may be applied to an FGM problem.

Finally, concluding remarks are given in Chapter 6.

Chapter 2

Background

In this chapter, we review linear elasticity and its derivation along with the numerical solution used. We also review some of the structural optimisation methods in more detail as these are the building blocks for the rest of the thesis. The purpose of this chapter is twofold. Firstly, it is always important to keep fresh in mind the fundamental pillars on which the theory stands and, secondly, it helps to clarify notation early so that in the subsequent chapters symbols such as C_{ijkl} (the stiffness tensor) may be used without explanation.

2.1 Derivation of Linear Elasticity

We begin by deriving the equations that govern linear elasticity. Linear elasticity is concerned with elastic solids that have only small displacements. That the material is elastic means that the reaction forces in the solid are dependent on the final configuration and not on the history of loading. Restricting to small displacements means that linear approximations can be used, greatly simplifying the theory and the techniques required to solve the resulting equations. Much of the following derivation is similar to that written by Love (1944) while taking advantage of modern vector notation.

2.1.1 Strain

Taking a Lagrangian view (Fig. 2.1), we describe the motion of the continuum using a displacement field $\boldsymbol{u}(\boldsymbol{x})$. A particle at $\boldsymbol{x}$ is displaced to the position $\boldsymbol{x}'$ with

$$\boldsymbol{x}' = \boldsymbol{x} + \boldsymbol{u}(\boldsymbol{x}). \tag{2.1}$$

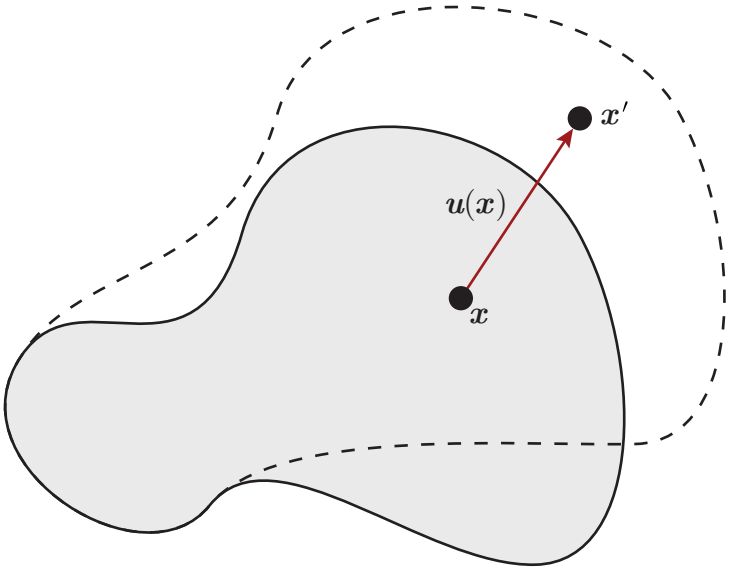

FIGURE 2.1: In a Lagrangian view the movement of material is tracked using its displacement from the initial position. As elsewhere in the chapter, the original continuum location is illustrated by the shaded region while the displaced continuum is shown with a dotted outline.

To the first order about $\boldsymbol{x}_0$ we have that

$$\begin{aligned}\boldsymbol{u}(\boldsymbol{x}) &= \boldsymbol{u}(\boldsymbol{x}_0) + (\boldsymbol{x} - \boldsymbol{x}_0) \cdot \nabla \boldsymbol{u}(\boldsymbol{x}_0) && (2.2)\\ &= \boldsymbol{u}(\boldsymbol{x}_0) + (\boldsymbol{x} - \boldsymbol{x}_0) \cdot \left(\frac{1}{2}(\nabla \boldsymbol{u} - (\nabla \boldsymbol{u})^{\mathrm{T}}) + \frac{1}{2}(\nabla \boldsymbol{u} + (\nabla \boldsymbol{u})^{\mathrm{T}}) \right) && (2.3)\\ &= \boldsymbol{u}(\boldsymbol{x}_0) + (\boldsymbol{x} - \boldsymbol{x}_0).(R + \varepsilon) && (2.4)\end{aligned}$$

where

$$R = \frac{1}{2}(\nabla \boldsymbol{u} - (\nabla \boldsymbol{u})^{\mathrm{T}}) \tag{2.5}$$

is an anti-symmetric second order tensor and

$$\varepsilon = \frac{1}{2}(\nabla \boldsymbol{u} + (\nabla \boldsymbol{u})^{\mathrm{T}}) \tag{2.6}$$

is a symmetric second order tensor. So a particle at $\boldsymbol{x}$ close to $\boldsymbol{x}_0$ is displaced to

$$\boldsymbol{x}' = \boldsymbol{x} + \boldsymbol{u}(\boldsymbol{x}_0) + (\boldsymbol{x} - \boldsymbol{x}_0) \cdot R + (\boldsymbol{x} - \boldsymbol{x}_0) \cdot \varepsilon. \tag{2.7}$$

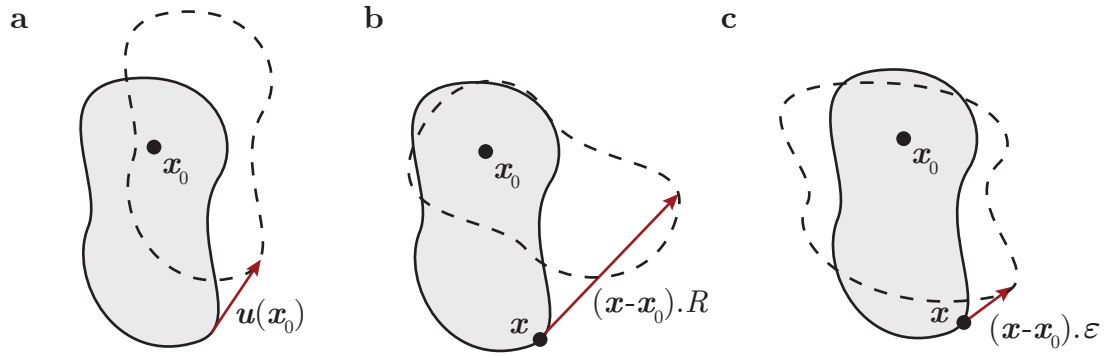

FIGURE 2.2: The displacement of material in a small region about $\boldsymbol{x}_0$ can be decomposed into: (**a**) a rigid body translation, (**b**) a rigid body rotation, and (**c**) deformation.

Now, a rotation about the origin and about the axis (a_1, a_2, a_3) by an angle of θ is a linear transformation. To the first order in θ, this transformation has the matrix

$$\mathrm{Rot}(\theta) = \begin{bmatrix} 1 & -a_3\theta & a_2\theta \\ a_3\theta & 1 & -a_1\theta \\ -a_2\theta & a_1\theta & 1 \end{bmatrix} \tag{2.8}$$

$$= I + \theta \begin{bmatrix} 0 & -a_3 & a_2 \\ a_3 & 0 & -a_1 \\ -a_2 & a_1 & 0 \end{bmatrix} \tag{2.9}$$

$$= I + R'. \tag{2.10}$$

Noting that R' is a general anti-symmetric matrix we may interpret the tensor R as a small rotation about the point x_0.

We can now interpret the terms on the right hand side of (2.7) to be, respectively: the original position, a rigid body translation, a rigid body rotation, and material deformation (Fig. 2.2). The material is expected to exert a force returning it to its original shape. This force, however, will not depend on any rigid body transformations and thus will depend solely on the deformation summarised in ε, which we call the *strain tensor*.

As ε is a symmetric tensor its eigenvectors are orthogonal. We may therefore construct a matrix P with the normalised eigenvectors, where $P^{-1} = P^{\mathrm{T}}$. Diagonalising ε gives

$$D = P^{-1}\varepsilon P = P^{\mathrm{T}}\varepsilon P. \tag{2.11}$$

However this transformation can also be seen as a rotation of basis, and so there exists an

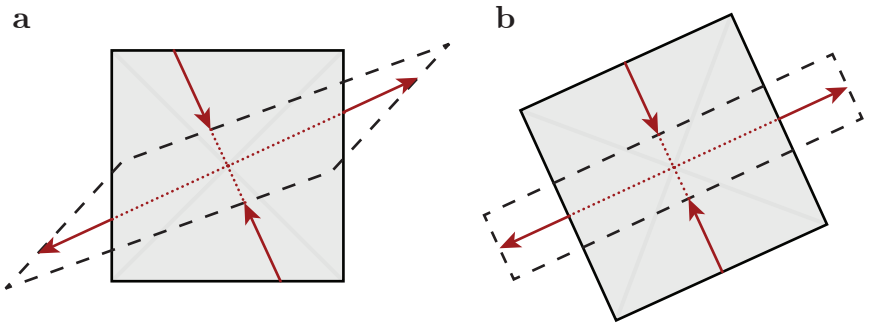

FIGURE 2.3: Both squares are deformed with the same (randomly chosen) strain tensor ε. While the deformation in (**a**) involves shearing the square, one can always rotate the square as in (**b**) such that it aligns with the eigenvectors of ε (dotted in red) illustrating the principal strains.

orthogonal basis where the strain tensor consists only of axial strains (compressions and extensions) without shear (Fig. 2.3); these eigenvectors and eigenvalues are called the *principal strains*.

2.1.2 Stress

Consider a tetrahedron inside the material with three of the faces having normals along the negative axes. That is, the normals are $-\boldsymbol{i}$, $-\boldsymbol{j}$, and $-\boldsymbol{k}$, with the fourth being $\boldsymbol{n}$. Set the surface stresses to be $\boldsymbol{T}_i$ and areas to be A_i (Fig. 2.4). As the object is at rest the forces must balance, giving

$$\boldsymbol{T}_4 = -\frac{A_1}{A_4}\boldsymbol{T}_1 - \frac{A_2}{A_4}\boldsymbol{T}_2 - \frac{A_3}{A_4}\boldsymbol{T}_3 \tag{2.12}$$

$$= -(\boldsymbol{n}\cdot\boldsymbol{i})\boldsymbol{T}_1 - (\boldsymbol{n}\cdot\boldsymbol{j})\boldsymbol{T}_2 - (\boldsymbol{n}\cdot\boldsymbol{k})\boldsymbol{T}_3. \tag{2.13}$$

Thus we see for an arbitrary surface inside the material the stress on that surface is a linear transformation of the surface normal. We can therefore define the second order stress tensor, σ, such that the stress on any intersecting plane with normal $\boldsymbol{n}$ is

$$\boldsymbol{T}_{\boldsymbol{n}} = \sigma\cdot\boldsymbol{n}. \tag{2.14}$$

Consider now a small cube with side length Δ. Now consider the torque τ_z on this cube about the z-axis. We have that

$$\tau_z = \sigma_{yx}\Delta^2\Delta - \sigma_{xy}\Delta^2\Delta. \tag{2.15}$$

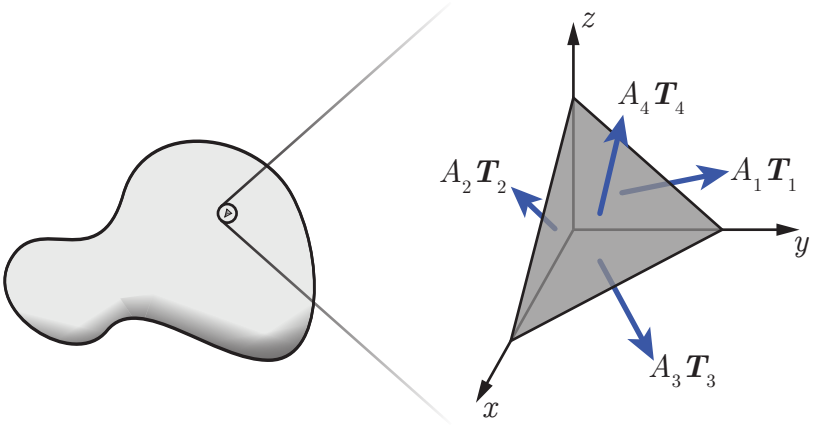

FIGURE 2.4: Consider a small tetrahedron inside the material continuum. The forces acting on each surface must sum to zero as the material is at rest.

The moment of inertia I_z about the same axis is

$$I_z = \int \sqrt{x^2 + y^2}\, dV = a\Delta^4 \tag{2.16}$$

where $a = \frac{8}{3}(\sqrt{2} + \operatorname{arcsinh}(1))$. The angular velocity ω_z satisfies

$$\dot{\omega}_z = \frac{\tau_z}{I_z} \tag{2.17}$$

$$= \frac{(\sigma_{yx} - \sigma_{xy})\Delta^3}{a\Delta^4}. \tag{2.18}$$

For $\dot{\omega}_z$ to remain bounded as $\Delta \to 0$ we require that $\sigma_{xy} - \sigma_{yx} = 0$. This argument can be repeated for each rotational axis to show that σ must be symmetric, with $\sigma_{ij} = \sigma_{ji}$. As σ is a symmetric tensor we may make the same diagonalisation argument as was made for ε to define the *principal stresses*. In general the principal stresses and principal strains may have different directions, although for an isotropic material one can show they will be the same.

2.1.3 The constitutive equation

We assume that the displacements are small and that the material behaves elastically. That is, we assume that the stress is a linear function of the strain to obtain a generalised form of Hooke's law linearly relating the stress to the strain,

$$\sigma = C : \varepsilon. \tag{2.19}$$

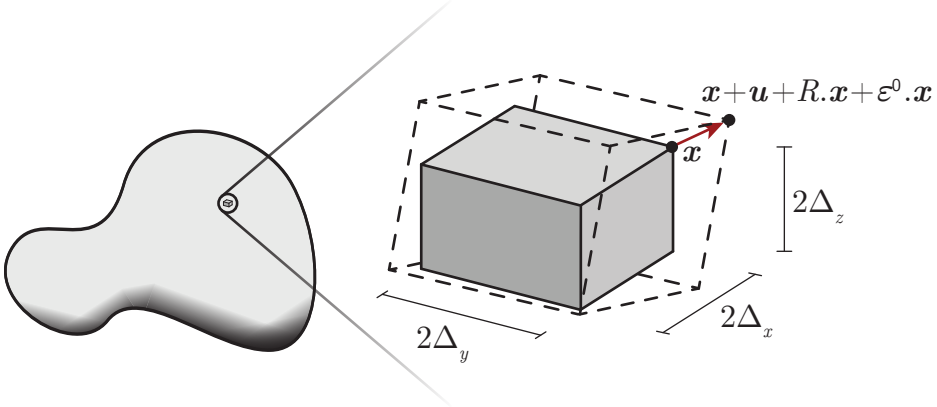

FIGURE 2.5: Consider a small hexahedron wholly contained in the material continuum. Each point inside that hexahedron is moved according to (2.22).

C is the fourth order *stiffness tensor* and describes the elastic response of a particular material to deformation. The inverse of the stiffness tensor is the *compliance tensor*, S_{ijkl} which satisfies

$$\varepsilon = S : \sigma. \tag{2.20}$$

As ε and σ are both symmetric we define the stiffness tensor to have the same symmetries, namely

$$C_{ijkl} = C_{jikl} = C_{ijlk}. \tag{2.21}$$

Using C to denote the stiffness tensor and S to denote the compliance tensor is an unfortunate notational quirk, however to switch the two or introduce new symbols would only serve to confuse the matter further.

When the material is deformed it stores *elastic energy*, we calculate this through the work done on a small hexahedron. Let the hexahedron have sides of length $2\Delta_x$, $2\Delta_y$ and $2\Delta_z$ (Fig. 2.5). Further, let the hexahedron be deformed such that the path $\boldsymbol{r}$ that a point will take from the position $\boldsymbol{x}$ is

$$r_i = x_i + t(u_i + R_{ij}x_j + \varepsilon^0_{ij}x_j), \tag{2.22}$$

where u_i is a rigid body translation and R a rigid body rotation. The strain is therefore

$$\varepsilon = t\varepsilon^0, \quad t \in [0, 1], \tag{2.23}$$

and the traction (force per area) on a surface is

$$T_i = n_j \sigma_{ij} = t n_j C_{ijkl} \varepsilon^0_{kl}. \tag{2.24}$$

The work done by the traction over the top surface of the cube is

$$W_{z^+} = \int_{-\Delta_x}^{\Delta_x} \int_{-\Delta_y}^{\Delta_y} \int_0^1 T_i \frac{dr_i}{dt}\, dt\, dy\, dx \tag{2.25}$$

$$= 2\,\Delta_x\,\Delta_y\, C_{i3kl} \varepsilon^0_{kl} (2u_i + R_{i3}\Delta_z + \varepsilon^0_{i3}\Delta_z), \tag{2.26}$$

and for the bottom

$$W_{z^-} = 2\Delta_x\Delta_y\, C_{i3kl} \varepsilon^0_{kl} (-2u_i + R_{i3}\Delta_z + \varepsilon^0_{i3}\Delta_z). \tag{2.27}$$

Similar results are found for the sides. The work done on all surfaces is therefore

$$W(\varepsilon^0_{ij}) = W_{+x} + W_{-x} + W_{+y} + W_{-y} + W_{+z} + W_{-z} \tag{2.28}$$

$$= 4 C_{ijkl} \varepsilon^0_{kl} (R_{ij} + \varepsilon^0_{ij}) \Delta_x \Delta_y \Delta_z \tag{2.29}$$

$$= 4 C_{ijkl} \varepsilon^0_{kl} \varepsilon^0_{ij} \Delta_x \Delta_y \Delta_z. \tag{2.30}$$

The final equality holds as C_{ijkl} is symmetric in i and j and R_{ij} is antisymmetric, implying $C_{ijkl} R_{ij} = 0$. The work done is equal to the total strain energy stored in the deformation of the hexahedron as it is in the elastic regime and the energy used to deform the hexahedron may be recovered by the hexahedron returning to its original shape. The average stored energy due to the strain ε_{ij} is therefore

$$U(\varepsilon_{ij}) = \frac{W(\varepsilon_{ij})}{8\Delta_x\Delta_y\Delta_z} = \frac{1}{2} C_{ijkl} \varepsilon_{kl} \varepsilon_{ij}, \tag{2.31}$$

and is called the strain energy or strain energy density.

From (2.31) we can show that the stiffness tensor C_{ijkl} has an additional symmetry. We have

$$\frac{\partial}{\partial \varepsilon_{ij}} \frac{\partial}{\partial \varepsilon_{kl}} U = C_{ijkl}, \tag{2.32}$$

but the order of differentiation does not matter, so we find that

$$C_{ijkl} = C_{lkij}. \tag{2.33}$$

Taking into account the three symmetries, the stiffness tensor has only 21 degrees of freedom. If the material is isotropic, there are only two degrees of freedom. Commonly the Young's modulus E and Poisson's ratio ν are used to specify the full linear elastic properties of an isotropic material.

Sometimes it's useful to express the linear elastic equations using *Voigt's notation* where the stress and strain become the vectors

$$\varepsilon_\alpha = \begin{bmatrix} \varepsilon_{11} \\ \varepsilon_{22} \\ \varepsilon_{33} \\ 2\varepsilon_{23} \\ 2\varepsilon_{13} \\ 2\varepsilon_{12} \end{bmatrix} \quad \text{and} \quad \sigma_\alpha = \begin{bmatrix} \sigma_{11} \\ \sigma_{22} \\ \sigma_{33} \\ \sigma_{23} \\ \sigma_{13} \\ \sigma_{12} \end{bmatrix}. \tag{2.34}$$

(2.19) then becomes

$$\sigma_\alpha = C_{\alpha\beta}\varepsilon_\beta, \tag{2.35}$$

and the fourth order tensor C_{ijkl} can be written as the symmetric matrix $C_{\alpha\beta}$. In this thesis, when using Voigt's notation subscripts will be Greek indices, as in (2.35).

2.1.4 Variational solution

We can find the displacement for a given load by minimising the energy of a system. If we have material in a domain Ω with a stiffness tensor C_{ijkl} and a traction on the surface $\partial\Omega$ of $\boldsymbol{t}$, then the total energy stored in the system is

$$W = \int_\Omega U \, d\boldsymbol{x} - \int_{\partial\Omega} t_i u_i \, d\boldsymbol{x} \tag{2.36}$$

$$= \frac{1}{2}\int_\Omega \varepsilon_{ij} C_{ijkl} \varepsilon_{kl} \, d\boldsymbol{x} - \int_{\partial\Omega} t_i u_i \, d\boldsymbol{x} \tag{2.37}$$

$$= \frac{1}{2}\int_\Omega \frac{\partial u_i}{\partial x_j} C_{ijkl} \frac{\partial u_k}{\partial x_l} \, d\boldsymbol{x} - \int_{\partial\Omega} t_i u_i \, d\boldsymbol{x}. \tag{2.38}$$

To minimise W we take a variation on $\boldsymbol{u}$ so that $\boldsymbol{u} = \boldsymbol{u}^0 + \delta\boldsymbol{v}$ where δ is a small parameter and $\boldsymbol{u}^0$ is an optimal solution. As $\boldsymbol{u}^0$ is optimal and δ is small

$$\frac{\partial W}{\partial \delta} = \int_\Omega \frac{\partial u_i}{\partial x_j} C_{ijkl} \frac{\partial v_k}{\partial x_l}\, d\boldsymbol{x} - \int_{\partial\Omega} t_i v_i\, d\boldsymbol{x} \tag{2.39}$$

$$= O(\delta). \tag{2.40}$$

Taking $\delta \to 0$ we see that at the extrema of W

$$\int_\Omega \frac{\partial u_i}{\partial x_j} C_{ijkl} \frac{\partial v_k}{\partial x_l}\, d\boldsymbol{x} = \int_{\partial\Omega} t_i v_i\, d\boldsymbol{x} \tag{2.41}$$

for all functions $\boldsymbol{v}$.

2.1.5 Numerical solution

In order to practically solve (2.41) for strange domains (such as the shape of a squid) and complicated, spatially varying stiffness tensors C_{ijkl}, a numerical solution must be sought. Finite element analysis (FEA) is used for this task. We may represent $\boldsymbol{u}$ as a linear combination of basis functions, say η_p,

$$u_i(\boldsymbol{x}) = \sum_p u_{ip} \eta_p(\boldsymbol{x}) \tag{2.42}$$

where u_{ip} are not functions of position. The total energy is then

$$W = \sum_{p,q} \frac{1}{2} u_{ip} u_{kq} \int_\Omega C_{ijkl} \frac{\partial \eta_p}{\partial x_j} \frac{\partial \eta_q}{\partial x_l}\, d\boldsymbol{x} - \sum_p u_{ip} \int_{\partial\Omega} t_i \eta_p\, d\boldsymbol{x}. \tag{2.43}$$

Which can be minimised with respect to each of the u_{ip} constants

$$\frac{\partial W}{\partial u_{ip}} = \sum_q u_{kq} \int_\Omega C_{ijkl} \frac{\partial \eta_p}{\partial x_j} \frac{\partial \eta_q}{\partial x_l}\, d\boldsymbol{x} - \int_{\partial\Omega} t_i \eta_p\, d\boldsymbol{x} = 0. \tag{2.44}$$

We can also derive (2.44) from (2.41) by noting that if (2.41) is true for $\boldsymbol{v}$, then it must also hold for $\alpha\boldsymbol{v}$, and so it suffices to consider only $v_i \in \{\eta_p\}$.

To solve (2.44) numerically, rather than choosing a true basis for all functions $\mathbb{R}^n \to \mathbb{R}$, we approximate with a finite basis. In such a case we can explicitly calculate a matrix K, indexed

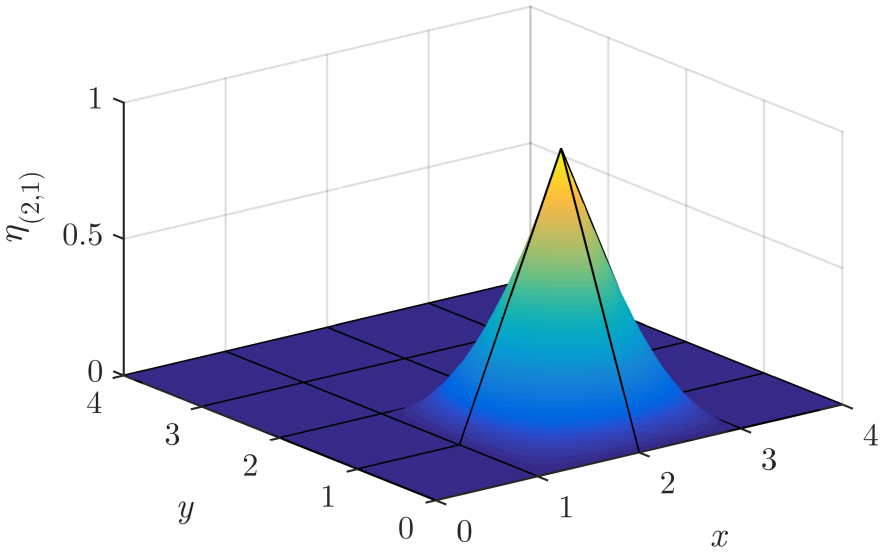

FIGURE 2.6: The bilinear shape function associated with the point at $x = 2$, $y = 1$ where mesh elements have side lengths of 1. Note that the shape function has support restricted to the elements immediately around $x = 2$, $y = 1$.

by two pairs of indices (denoting a pair of indices as (ip)),

$$K_{(ip)(kq)} = \int_\Omega C_{ijkl} \frac{\partial \eta_p}{\partial x_j} \frac{\partial \eta_q}{\partial x_l} \, d\boldsymbol{x}. \tag{2.45}$$

This matrix is called the *stiffness matrix* as it embodies the effect of the stiffness tensor. Note that K is symmetric and positive definite as the product $u_{(ip)} K_{(ip)(jq)} u_{(jq)}$ calculates the strain energy, which cannot be negative. We can define the *load vector* to embody the effect of the load on the problem as

$$s_{(ip)} = \int_{\partial\Omega} t_i \eta_p \, d\boldsymbol{x}. \tag{2.46}$$

We can thus find a numerical solution to the linear elastic problem by solving the matrix equation

$$K_{(ip)(kq)} u_{(kq)} = s_{(ip)}. \tag{2.47}$$

In this thesis we choose the bilinear and trilinear Lagrange basis functions on a regular mesh for two and three dimensions respectively. Each of these functions is associated with nodes on the mesh. At the associated node the function is 1 and at all other nodes the function is 0. This allows easy interpretation of results as the displacement at any particular node can be

"read off" the solution vector. An example of a bilinear basis function can be seen in Fig. 2.6. If the mesh elements have side lengths of 1, then the trilinear basis function associated with the point $(1, 1, 1)$ is then

$$\eta(\boldsymbol{x}) = \begin{cases} xyz, & x \in [0,1], y \in [0,1], z \in [0,1] \\ (2-x)yz, & x \in [1,2], y \in [0,1], z \in [0,1] \\ x(2-y)z, & x \in [0,1], y \in [1,2], z \in [0,1] \\ (2-x)(2-y)z, & x \in [1,2], y \in [1,2], z \in [0,1] \\ xy(2-z), & x \in [0,1], y \in [0,1], z \in [1,2] \\ (2-x)y(2-z), & x \in [1,2], y \in [0,1], z \in [1,2] \\ x(2-y)(2-z), & x \in [0,1], y \in [1,2], z \in [1,2] \\ (2-x)(2-y)(2-z), & x \in [1,2], y \in [1,2], z \in [1,2] \\ 0, & \text{otherwise.} \end{cases} \tag{2.48}$$

These basis functions have the benefit that they have finite and quite restricted support making the matrix K very sparse.

In order to solve (2.47) efficiently, the conjugate gradient method is used with either a multigrid preconditioner or a geometric agglomerated multigrid preconditioner (GAMG). The GAMG preconditioner agglomerates elements without the need for an explicit coarsening scheme and so can be used on a wider range of meshes. These preconditioners are generated by solving the problem on a coarse mesh first helping reduce large wavelength errors before the 'true' solver reduces the low wavelength errors on the finer mesh. These methods are implemented in the PETSc framework (Balay et al., 1997, 2016).

2.2 Homogenisation of periodic microstructures

The above continuum theory is predicated on the elastic material being a continuum, that is it relies on the ability to divide up the material infinitely and each piece still retain the same governing laws. Of course no material is truly like this, on some small scale every material will cease to act as a continuum and the behaviour of individual constituents will become important. The value of elastic theory lies in it modelling the bulk, or average, behaviour without regard to the small details. We can apply the same principle to periodic microstructures, structures with regular variation on a very fine length scale. Such microstructures can also be modelled as a material if we are concerned about the bulk behaviour at a length scale large enough in

comparison to the microstructural variations. Taking a description of a microstructure and producing a bulk model is called *homogenisation*.

Here we concern ourselves only with periodic microstructures, or pseudo periodic where the microstructures deviate from truly periodic only slowly over many periods. Such a microstructure can be described with a *representative volume element* (RVE) which is repeated in all directions.

Consider a single hexahedral RVE ω inside a large group, far from the edge. Let the average strain inside this RVE be

$$\langle \varepsilon_{ij} \rangle = \frac{1}{|\omega|} \int_\omega \varepsilon_{ij} \, d\boldsymbol{x}. \tag{2.49}$$

Similarly, let the average stress be

$$\langle \sigma_{ij} \rangle = \frac{1}{|\omega|} \int_\omega \sigma_{ij} \, d\boldsymbol{x}. \tag{2.50}$$

As this microstructure is inside a large collection of similar microstructures, we may discard the deviations from average strain over large length scales and assume the displacement is

$$u_i = \varepsilon^0_{ij} x_j + u'_i \tag{2.51}$$

where $\boldsymbol{u}'$ is periodic and ε^0_{ij} is the overall bulk strain of the macroscopic material. Now,

$$\langle \varepsilon_{ij} \rangle = \frac{1}{2|\omega|} \int_\omega \frac{\partial}{\partial x_j}(\varepsilon^0_{ik} x_k + u'_i) + \frac{\partial}{\partial x_i}(\varepsilon^0_{ik} x_k + u'_i) \, d\boldsymbol{x} \tag{2.52}$$

$$= \varepsilon^0_{ij} + \frac{1}{2|\omega|} \int_{\partial\omega} u'_i n_j + u'_j n'_i \, d\boldsymbol{x} \tag{2.53}$$

where we have made use of Gauss' divergence theorem. The surface integral in (2.53) will be zero as $\boldsymbol{u}'$ is periodic causing opposing faces to cancel. Thus we find that

$$\langle \varepsilon_{ij} \rangle = \varepsilon^0_{ij}. \tag{2.54}$$

That is, we may impose an average strain $\langle \varepsilon_{ij} \rangle$, by requiring that the displacement satisfies (2.51). Such a displacement may be found by numerically solving (2.41) for $\boldsymbol{u}'$ under the assumption of (2.51).

Let $\varepsilon_{ij}^{kl}(\boldsymbol{x})$ be the strain field induced by the imposed average strain

$$\varepsilon_{ij}^{0} = \frac{1}{2}(\delta_{ik}\delta_{jl} + \delta_{il}\delta_{jk}). \tag{2.55}$$

We may then find

$$\langle \sigma_{ij}^{kl} \rangle = \frac{1}{|\omega|} \int_{\omega} C_{ijmn}(\boldsymbol{x}) \varepsilon_{mn}^{kl} \, d\omega, \tag{2.56}$$

with C_{ijkl} varying depending on the material at $\boldsymbol{x}$, likely solid or void. Thus we are able to determine C_{ijkl}^{*}, the *effective material tensor*, which satisfies

$$\langle \sigma_{ij} \rangle = C_{ijkl}^{*} \langle \varepsilon_{kl} \rangle \tag{2.57}$$

through

$$\begin{aligned} \langle \sigma_{ij}^{kl} \rangle &= C_{ijmn}^{*} \langle \varepsilon_{mn}^{kl} \rangle & (2.58)\\ &= \frac{1}{2} C_{ijmn}^{*} (\delta_{mk}\delta_{nl} + \delta_{ml}\delta_{nk}) & (2.59)\\ &= C_{ijkl}^{*}. & (2.60) \end{aligned}$$

This requires solving the equations of elasticity 6 times, once for each of the unique components of ε.

This concept of taking a periodic microstructure and determining effective material properties is important to this thesis. It allows us to find effective material properties of microstructures thus decoupling the microstructural deformation from the macrostructural and making the computation of multiscale designs feasible.

2.3 The SIMP Method

A common structural optimisation problem is to minimise the compliance (maximise stiffness) of a design under load, subject to a volume constraint. If the design must fit inside some domain Ω (Fig. 2.7a), then we define a control function $\rho(\boldsymbol{x}) : \Omega \to \{0, 1\}$, with $\rho = 1$ signalling where material is present and $\rho = 0$ signalling where no material is present (Fig. 2.7b). The stiffness

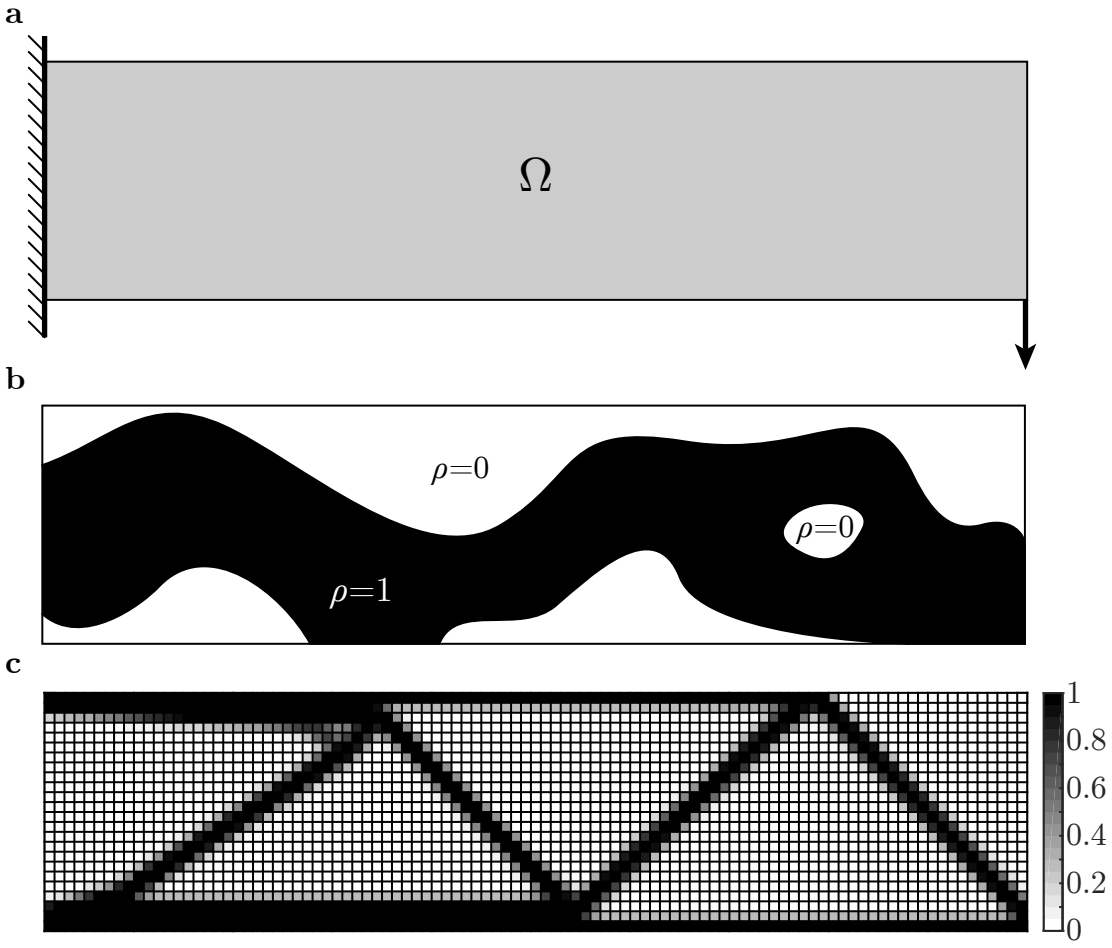

FIGURE 2.7: Optimising the stiffness of a cantilever beam using SIMP. (**a**) The optimisation domain Ω with boundary conditions. (**b**) A possible solid/void solution showing values of $\rho = 1$ for solid and $\rho = 0$ for void. (**c**) The optimised SIMP design densities. Note that the design is primarily fully solid or fully void but intermediate densities remain.

tensor can then be described as

$$C_{ijkl}(\rho) = \begin{cases} C^0_{ijkl}, & \rho = 1 \\ 0, & \rho = 0 \end{cases} \tag{2.61}$$

with C^0_{ijkl} being the stiffness tensor of the base material.

The optimisation problem then has the following numerical form,

$$\begin{aligned} &\min_{\rho} \int_{\partial\Omega} \boldsymbol{u}.\boldsymbol{s}\, d\boldsymbol{x} \\ &\text{s.t.} \begin{cases} K\big(C_{ijkl}(\rho)\big)\boldsymbol{u} = \boldsymbol{s} \\ \displaystyle\int_{\Omega} \rho\, dx \leq V^0 \end{cases} \end{aligned} \tag{2.62}$$

where K and $\boldsymbol{s}$ are defined above in (2.45) and (2.46). The constraints in (2.62) are that the displacements, $\boldsymbol{u}$, must satisfy the linear elastic equations derived above, and that the amount of material used is limited to $V^0 < |\Omega|$.

2.3.1 Method description

The optimisation problem (2.62) is difficult to solve due to the large solution space the integer function ρ provides when discretised and the expense of calculating the displacements $\boldsymbol{u}$. The idea of the *solid isotropic material with penalisation* (SIMP) method is to relax ρ to be a density function $\rho : \Omega \to [0, 1]$ and to replace (2.61) with the fictitious material law,

$$C_{ijkl}(\rho) = \rho^P C^0_{ijkl}, \tag{2.63}$$

where P is a parameter. We describe (2.63) as fictitious as there may not be a material with a stiffness that behaves as described; no physical interpretation is required however, as the few regions of intermediate densities in the final design would be removed before manufacture.

A 'large enough' exponent P combined with the volume constraint in (2.62) will make the use of intermediate densities in the optimisation inefficient. As an example, consider Fig. 2.8: rather than using two supports with $\rho = 0.5$, the structure would be stiffer if one similar sized support of $\rho = 1$ was used. This penalisation of intermediate density material is expected to drive the optimisation towards a structure that does not make use of intermediate density material, thus solving the original problem. Fig. 2.7c shows such an example. The relaxed formulation of the optimisation problem is easier to solve than the discrete as the solution space becomes

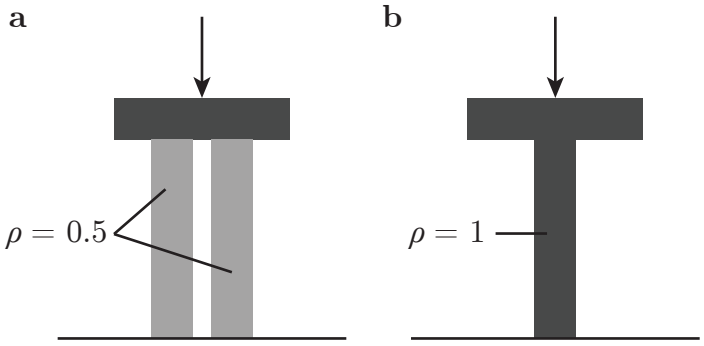

FIGURE 2.8: Using a SIMP law, the left structure (**a**), with two intermediate density struts, has a lower stiffness than the right (**b**), which uses one fully dense strut despite both having the same material cost

continuous. Steps can be taken by an optimisation algorithm that are smooth, creating regions of fractional "density". In addition, derivatives of the density can be calculated to provide information to the optimisation as to which direction should be taken.

Checker boarding, where a checker-board like pattern is produced, is a problem that occurs in structural optimisation. It is caused by the numerical solution modelling the stiffness higher than it should be in such a case (Bendsøe and Sigmund, 2003). Another problem is mesh dependence, in general the continuous structural optimisation problem (2.62) may not have a minimum. This is demonstrated by mesh refinement producing finer and finer details in optimised designs with a greater number of holes. Clearly an infimum exists as infinitely stiff structures are not physical; a good solution close to this infimum is still desirable even if the optimal cannot be achieved.

Both the checker boarding and mesh dependence problems are combated in this thesis by use of a sensitivity filter. The filter is (Sigmund, 1997; Bendsøe and Sigmund, 2003)

$$\widehat{\frac{\partial f}{\partial \rho_e}} = \frac{1}{\rho_e \sum_{i \in N_e} r_{\min} - \operatorname{dist}(e,i)} \sum_{i \in N_e} (r_{\min} - \operatorname{dist}(e,i)) \rho_i \frac{\partial f}{\partial \rho_i}, \tag{2.64}$$

where $\operatorname{dist}(i,j)$ is the distance from the centre of element i to the centre of element j and

$$N_e = \{i \,|\, \operatorname{dist}(i,e) < r_{\min}\}. \tag{2.65}$$

The filter is heuristic but performs well; $r_{\min}$ provides a length scale below which features cannot be produced as sensitivities are blurred. Essentially, the length scale of the smallest feature size is artificially enlarged to be above the scale of the finite elements. In addition, the minimum feature size persists over mesh refinement, 'fixing' the issue of mesh dependence.

2.3.2 Derivatives

How to find the derivatives of the objective function may not be immediately obvious, here they are found through the adjoint method. If the design variables are $\boldsymbol{b}$, then from (2.47) we can obtain

$$\frac{\partial \boldsymbol{u}}{\partial b_i} = -K^{-1}\frac{\partial K}{\partial b_i}\boldsymbol{u}. \tag{2.66}$$

So then by the chain rule

$$\frac{\partial f}{\partial b_i} = \left(\frac{\partial f}{\partial b_i}\right)_{\boldsymbol{u}} + \left(\frac{\partial f}{\partial \boldsymbol{u}}\right)^T \frac{\partial \boldsymbol{u}}{\partial b_i} \tag{2.67}$$

$$= \left(\frac{\partial f}{\partial b_i}\right)_{\boldsymbol{u}} - \left(\frac{\partial f}{\partial \boldsymbol{u}}\right)^T K^{-1}\frac{\partial K}{\partial b_i}\boldsymbol{u}, \tag{2.68}$$

where $\left(\frac{\partial f}{\partial b_i}\right)_{\boldsymbol{u}}$ is the partial derivative of f with respect to b_i holding $\boldsymbol{u}$ constant. Let the adjoint displacement be

$$\tilde{\boldsymbol{u}}^T = \left(\frac{\partial f}{\partial \boldsymbol{u}}\right)^T K^{-1} \tag{2.69}$$

which can be found by solving

$$K\tilde{\boldsymbol{u}} = \frac{\partial f}{\partial \boldsymbol{u}}. \tag{2.70}$$

Thus

$$\frac{\partial f}{\partial b_i} = \left(\frac{\partial f}{\partial b_i}\right)_{\boldsymbol{u}} - \tilde{\boldsymbol{u}}^T\frac{\partial K}{\partial b_i}\boldsymbol{u}. \tag{2.71}$$

Derivatives of a function f implicitly dependent on the solution (2.47) can be found with at most one extra matrix solve. In the case of compliance, the objective $f = \boldsymbol{u}^T\boldsymbol{t}$ is self adjoint. That is, (2.70) is the same as (2.47), $\tilde{\boldsymbol{u}} = \boldsymbol{u}$, and no extra solve is required.

2.4 The Level Set Method

Level set methods can be applied to a number of problems, here we describe how they have been applied to structural optimisation problems. In this thesis, the level set method is used to

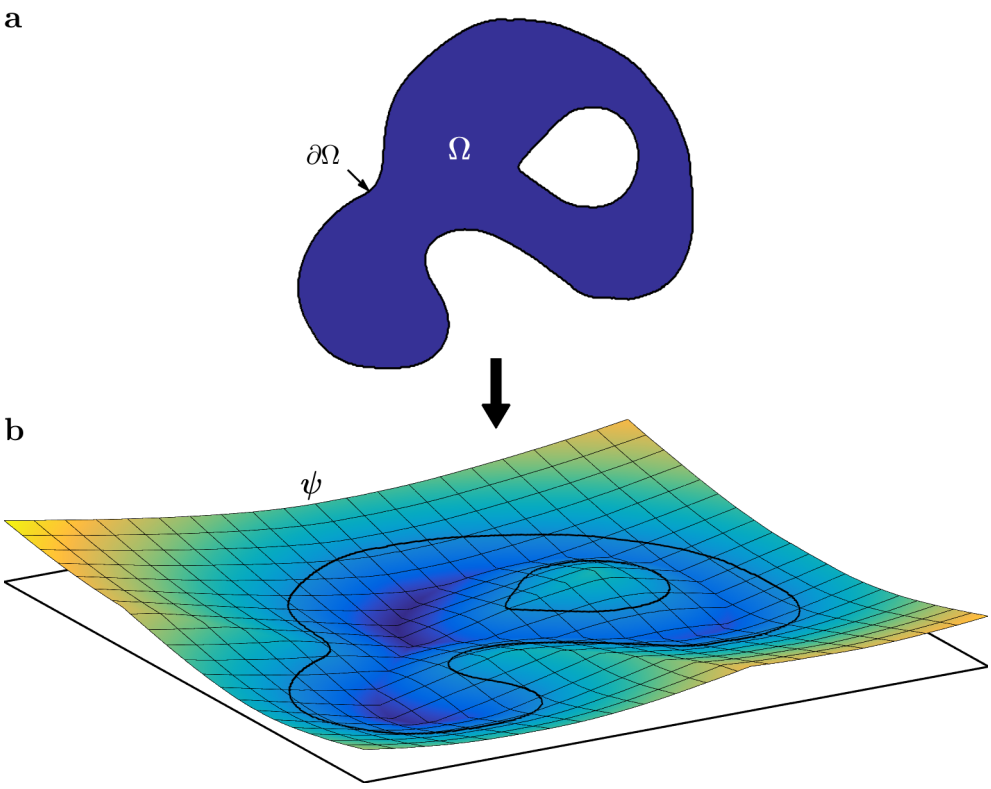

FIGURE 2.9: Example of a level set function. (**a**) The structural domain Ω with boundary $\partial\Omega$ to be represented. (**b**) An example of a level set function ψ that represents the domain Ω. The zero level set of ψ is $\partial\Omega$ while the solid portion, Ω, is where $\psi \leq 0$.

optimise microstructures which will then be interpolated and used as a basis for the macroscopic optimisation.

The main concept of level set methods is to represent a structural domain as the level set of a scalar function ψ. That is, we let the solid area of the structure be

$$\Omega = \{\boldsymbol{x} \,|\, \psi(\boldsymbol{x}) \leq 0\} \tag{2.72}$$

with the structure's boundary being

$$\partial\Omega = \{\boldsymbol{x} \,|\, \psi(\boldsymbol{x}) = 0\}. \tag{2.73}$$

A visual example of this can be seen in Fig. 2.9.

If we evolve ψ over time so that $\psi = \psi(\boldsymbol{x}, t)$, then the boundary (defined as $\psi(\boldsymbol{x}, t) = 0$) will move. Consider the derivative of ψ at a point tracking the moving boundary,

$$\frac{d\psi}{dt} = \frac{\partial \psi}{\partial t} + \nabla\psi \cdot \frac{d\boldsymbol{x}}{dt} = 0, \tag{2.74}$$

where $\frac{d\boldsymbol{x}}{dt}$ is the movement of the boundary point itself. As the boundary is defined to have $\psi = 0$ we have that for a point on the moving boundary $\frac{d\psi}{dt} = 0$. Set the normal velocity to be

$$\frac{d\boldsymbol{x}}{dt} \cdot \boldsymbol{n} = \frac{d\boldsymbol{x}}{dt} \cdot \nabla\psi \frac{1}{|\nabla\psi|} \tag{2.75}$$

$$= V, \tag{2.76}$$

then substitute into (2.74) for $\nabla\psi \cdot \frac{d\boldsymbol{x}}{dt}$ to obtain

$$\frac{\partial \psi}{\partial t} = -V|\nabla\psi|. \tag{2.77}$$

The equation (2.77) is called the *Hamilton-Jacobi evolution equation*. While (2.77) is true on the boundary $\partial\Omega$, it may be applied throughout the domain as an evolution equation for the level set function ψ. If V is positive, then $\frac{\partial\psi}{\partial t}$ will be negative causing ψ to decrease and the boundary to extend outwards; this is shown in one dimension in Fig. 2.10. Choosing V appropriately will allow us to perform an optimisation, this is the basis of the level set description in structural optimisation (Wang et al., 2003; Allaire et al., 2004).

The level set description has a number of benefits. The method describes a moving boundary without relaxing the problem and permitting infeasible intermediate density designs, keeping a valid design at all times. The level set method requires no repeated meshing of the solid as the boundary can be described on the same mesh as the solid, unlike other boundary tracking techniques such as using splines. Perhaps the strongest benefit of the level set method over other boundary tracking techniques is that topology changes are readily allowed and are not special cases. While hole nucleation can be an issue in two dimensions, three dimensions has no such issue due to the extra freedom permitted by the third spatial dimension (Allaire et al., 2005). For a more full description of level set methods and associated numerical concerns the reader is referred to Sethian (1999) and Osher and Fedkiw (2006).

In order to choose V, consider a functional $\mathcal{F} = \mathcal{F}(\Omega)$, and a perturbation of Ω to

$$\tilde{\Omega} = \{\boldsymbol{x} + \boldsymbol{\theta} \,|\, \boldsymbol{x} \in \Omega\}. \tag{2.78}$$

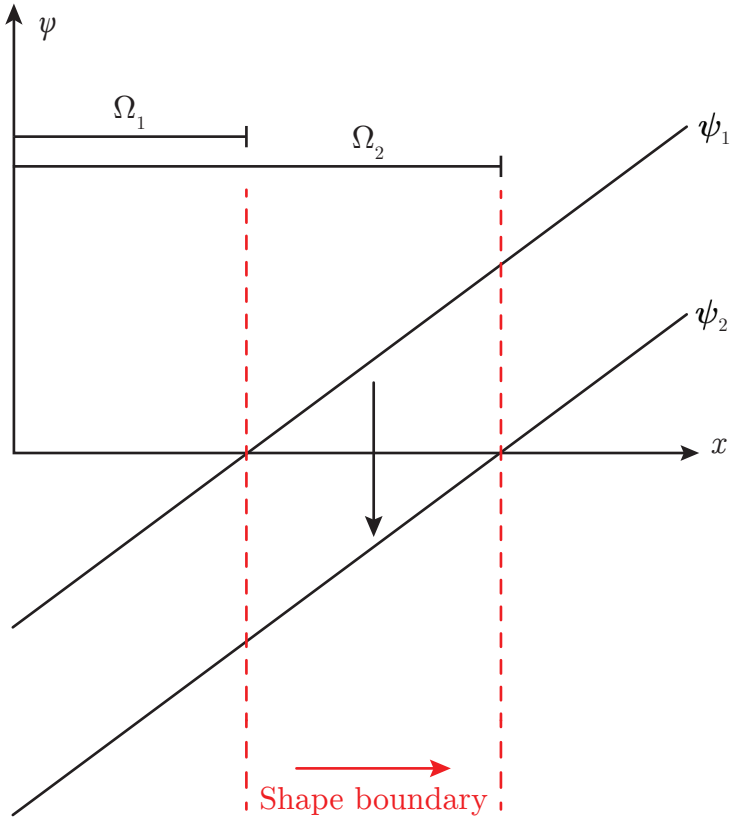

FIGURE 2.10: A moving boundary represented as a level set in one dimension. As the level set function changes from ψ_1 to ψ_2 the boundary moves right and the interval domain changes from Ω_1 to Ω_2.

The *material derivative*, $\mathcal{F}'$, is defined with

$$\mathcal{F}(\tilde{\Omega}) = \mathcal{F}(\Omega) + \mathcal{F}'(\Omega)(\boldsymbol{\theta}) + o(|\boldsymbol{\theta}|). \tag{2.79}$$

In general, the material derivative can be expressed in the intuitive form (Allaire et al., 2004)

$$\mathcal{F}'(\Omega)(\boldsymbol{\theta}) = \int_{\partial\Omega} v\boldsymbol{\theta}.\boldsymbol{n}\, dS \tag{2.80}$$

where v is the *shape sensitivity* of $\mathcal{F}$.

Assuming we can calculate the shape sensitivity and thus the effect of any perturbation to Ω, we must now choose a perturbation that results in the desired effect on the objective $\mathcal{F}$. The perturbation $\boldsymbol{\theta} = -v\boldsymbol{n}$ is called the steepest descent and results in

$$\mathcal{F}'(\Omega)(\boldsymbol{\theta}) = -\int_{\partial\Omega} v^2\, dS \leq 0. \tag{2.81}$$

Thus, choosing for (2.77)

$$V = -v \tag{2.82}$$

results in $\mathcal{F}$ monotonically decreasing over time as Ω evolves.

How to calculate v is beyond this thesis, for structural optimisation problems see Torquato and Donev (2004); Allaire et al. (2005); Challis et al. (2008b). In particular, see Challis (2009) for how to calculate shape sensitivities of effective elastic tensor components. Once v is found for a functional, rules for combinations follow naturally such as the chain and product rules.

This thesis uses the level set method to optimise microstructures, making use of the implementation from Challis et al. (2008a, 2014a). The implementation is also extended in Chapter 5 in order to generate anisotropic structures with specific Young's modulus profiles.

Chapter 3

Single Parameter Microstructure Interpolation

In this chapter we develop the basic ideas of the MIMO (microstructure interpolation for macroscopic optimisation) method and test them against some compliance minimisation problems. The microstructures are elastically isotropic and parameterised by density (microstructure volume fraction). Using optimised isotropic microstructures parameterised with a single dimension simplifies the first look at the method in a number of ways. As the microstructures are elastically isotropic, they can be compared to the Hashin-Shtrikman bounds (Hashin and Shtrikman, 1963) to ensure optimality. Elastic isotropy also removes the concern of microstructure orientation. Finally, having a single dimensional parameterisation ensures that the space of allowed microstructures is an interval, greatly aiding the macroscopic structural optimisation. These restrictions are lifted in Chapter 5.

3.1 Introduction

Recent advances in additive manufacturing now allow the physical construction of designs with features on the scale of 10μm (Zheng et al., 2014). This new manufacturing capability can be fully exploited using structural optimisation to find the best high resolution design for a particular application. While the resolution of structural design problems that can be solved computationally is increasing (Challis et al., 2014a; Aage et al., 2014), a large compute cluster is not always a feasible investment. Further, some objectives are computationally more expensive to optimise than others due to a lack of sensitivity information. In these cases and with current computational technology it is therefore still useful to seek efficient methods to solve structural optimisation problems at very high effective resolution.

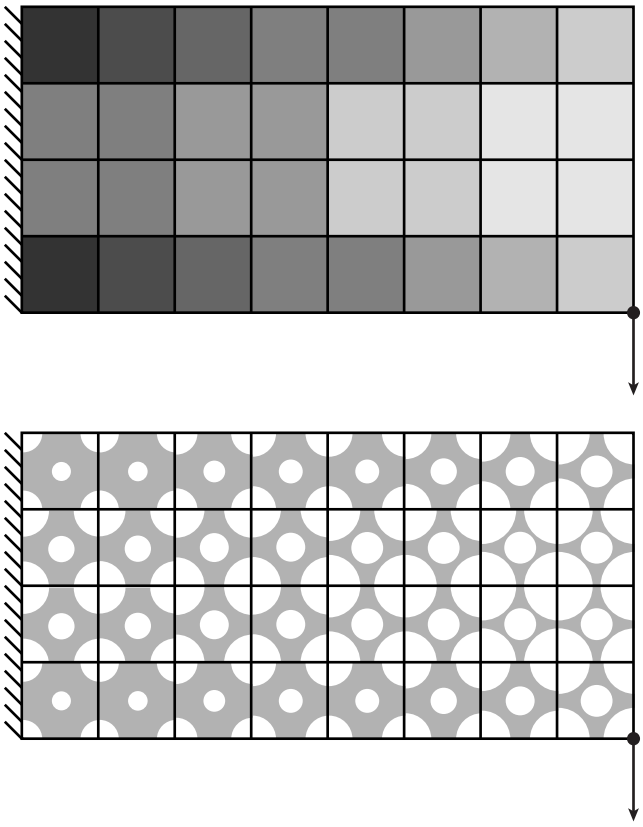

FIGURE 3.1: Each element in the macroscopic design makes use of a microstructure from a smoothly varying set. This figure is illustrative only: the macroscopic structure and microstructures shown are not optimised. (**top**) The macroscopic density. (**bottom**) The microstructures used in each element of the macroscopic structure. Note that this figure only illustrates the microstructure used in each element and in practice the microstructure would be far smaller than the elements used in the macroscopic domain.

As detailed in Chapter 1, some authors have incorporated microstructures into multiscale structural optimisation to provide a broader search space of solutions with finer detail than could be achieved through direct optimisation (e.g. Rodrigues et al., 2002; Coelho et al., 2008). These methods optimise "top-down": the microstructure in each element is optimised to best support the macroscopic loads. Homogenisation is used to decouple the macroscopic design problem from the microstructural design problem, allowing solutions to be found efficiently. Homogenisation assumes the microstructures vary smoothly so that the linearly elastic response of the periodic material may be determined by test strains over one cell; however in practice this smoothness is not always enforced. In addition to theoretical implications, the lack of smoothness complicates construction of such designs: how the microstructures in neighbouring elements interface is not clear.

We overcome this difficulty through "bottom-up" optimisation with the MIMO method: we

first find a smooth space of optimised microstructures that can be used as building blocks for the macroscopic optimisation problem (Fig. 3.1). The space of microstructures is found by interpolating between directly optimised *key microstructures*. Our method trades generality for better physical interpretation: while the space of allowed microstructures is diminished compared to other multiscale optimisation methods, the microstructures vary smoothly throughout the design. Our approach has the further benefit of being a computationally efficient way to design structures spanning two scales as no homogenisation calculations are needed during the macroscopic optimisation.

The chapter is organised as follows. Firstly the microstructure family is generated with the level set method (Section 3.2.1). The shape interpolation scheme is then described, from which the smooth space of microstructures is produced (Section 3.2.2). This smooth space of microstructures is evaluated, ensuring that the interpolated microstructures are indeed optimal and smooth (Section 3.2.3); smooth in the sense the geometry changes continuously but also in the sense that the material properties change with sufficient smoothness (e.g. continuously, and monotonically). This smooth space of microstructures is then used in a material distribution method optimising macroscopic designs for compliance under a variety of loads (Section 3.3).

3.2 Development of Interpolated Microstructures

Here we develop a smoothly varying set of microstructures over a range of densities with which a macroscopic design problem can be solved. We design isotropic microstructures for maximum bulk modulus at regularly spaced volume fractions. These explicitly optimised microstructures are used as key microstructures, in-between which microstructures are interpolated. Interpolating between the key structures allows us to develop a smoothly varying set of microstructures with which to solve our macroscopic design problem. The microstructure optimisation and interpolation are detailed below.

3.2.1 Optimisation of key microstructures

We use the Graphics Processing Unit (GPU) implementation of the level set method described by Challis et al. (2014a) to design periodic, isotropic microstructures with maximised bulk modulus. The bulk modulus is commonly used as a stiffness measure for microstructural optimisation (Sigmund, 2000; Guest and Prévost, 2006; Challis et al., 2008a) and allows comparison of optimised designs to the Hashin-Shtrikman bounds (Hashin and Shtrikman, 1963). Other effective material properties could be considered such as shear modulus or Young's modulus

(e.g. Sigmund, 2000). This implementation uses the level set method for topology optimisation (Wang et al., 2003; Allaire et al., 2004). Other topology optimisation methods can be used to achieve similar results (Sigmund, 2000; Yang et al., 2011). The microstructure optimisation problem is outlined here, and for details of the algorithm the reader is referred to the work of Challis et al. (2014a).

We consider periodic microstructures characterised by a representative base cell consisting of 120^3 voxels. The two materials within the base cell are a solid material with Young's modulus $E_0 = 1$ and Poisson's ratio $\nu = 0.3$, and a void material with a Young's modulus of zero. We solve the optimisation problem

$$\begin{aligned} &\max_{\boldsymbol{\chi}} K(\boldsymbol{\chi}), \\ &\text{subject to } \begin{cases} |\rho(\boldsymbol{\chi}) - \rho_{\text{req}}| \leq 0.005, \\ A(\boldsymbol{\chi}) \leq 0.01, \\ \boldsymbol{h}(\boldsymbol{\chi}) = \mathbf{0}. \end{cases} \end{aligned} \tag{3.1}$$

Here $\boldsymbol{\chi}$ is the vector of design variables specifying each element as either solid or void; $K(\boldsymbol{\chi})$ is the bulk modulus of the periodic material generated from the base cell; $\rho(\boldsymbol{\chi})$ is the volume fraction of solid material within the base cell; ρ_{req} is the required solid fraction; $A(\boldsymbol{\chi})$ measures the anisotropy of the material; and $\boldsymbol{h}(\boldsymbol{\chi}) = \mathbf{0}$ corresponds to the linear elasticity homogenization equations.

The anisotropy measure $A(\boldsymbol{\chi})$ is calculated as (Challis et al., 2008a, 2014a)

$$A = \sqrt{\frac{(C^*_{ijkl} - C^{\text{iso}}_{ijkl})(C^*_{ijkl} - C^{\text{iso}}_{ijkl})}{C^{\text{iso}}_{mnpq} C^{\text{iso}}_{mnpq}}}, \tag{3.2}$$

where C^*_{ijkl} is the effective elasticity tensor for the periodic material generated by the base cell, and C^{iso}_{ijkl} is the closest truly isotropic tensor to the computed C^*_{ijkl} as defined by the measure A above.

The optimisation problem (3.1) is solved for required solid fractions of $\rho_{\text{req}} \in \{0.1, 0.3, 0.5, 0.7, 0.9\}$. Each problem is solved with a range of optimisation parameters and the best result is chosen (Challis et al., 2014a). The resulting base cells are used as key microstructures for the microstructure interpolation. To ensure that these key structures have similar topology and geometry the solution for $\rho = 0.5$ is generated first. Optimisations for other volume fractions are then started from the optimisation solution at the neighbouring solid fraction.

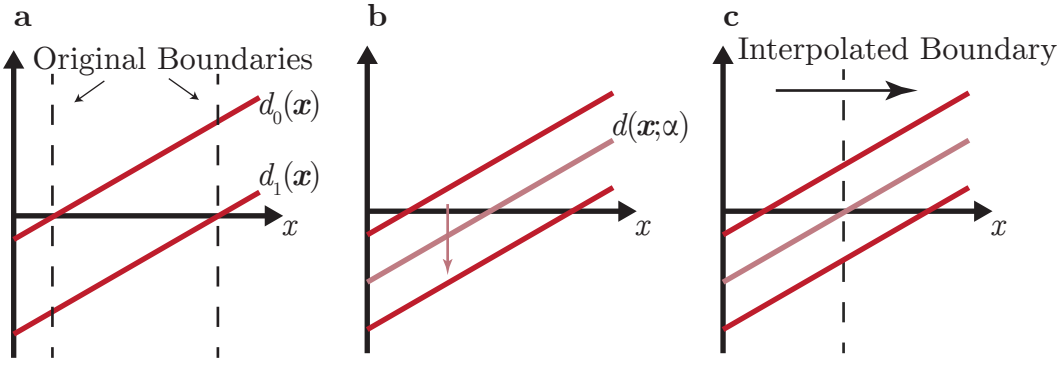

FIGURE 3.2: (**a**) The functions d_0 and d_1 define the initial shapes. (**b**) The function d smoothly transitions between d_0 and d_1. (**c**) d defines the interpolated boundary.

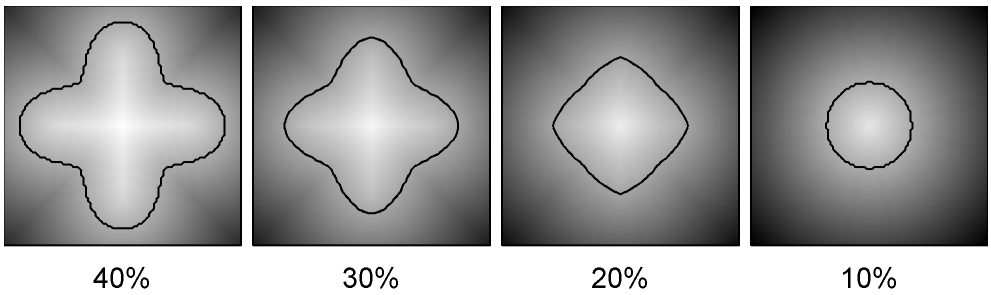

FIGURE 3.3: Example of interpolating between two 2D shapes. Original shapes on the very left and very right, interpolated shapes between. Distance maps are shown in greyscale. The volume of each shape is indicated with the percentages

3.2.2 Microstructure interpolation

Shape metamorphosis takes two key shapes and smoothly transitions between them. There are many methods to accomplish this which focus on pleasing aesthetics of the "morph" (e.g., He et al., 1994; Breen and Whitaker, 2001). Our problem is different to the typical problems that these methods are applied to. Firstly, the structures have quite similar features and secondly, we are concerned with smoothly changing properties of the interpolated microstructures rather than simply aesthetics.

The shape interpolation (metamorphosis) used here makes use of the signed distance function as would be used in a level set method. The method used here is similar to Raya and Udupa (1990). While more complicated methods could be used (e.g., He et al., 1994; Breen and Whitaker, 2001) the simple one is satisfactory as we show in Section 3.2.3.

Firstly we define $d_0(\boldsymbol{x})$ and $d_1(\boldsymbol{x})$ as the signed shortest distance of the point $\boldsymbol{x}$ to the surface of the two key shapes where a positive value indicates the point is interior. We can then define

$$d(\boldsymbol{x};\alpha) = (1-\alpha)d_0(\boldsymbol{x}) + \alpha d_1(\boldsymbol{x}) \tag{3.3}$$

with $\alpha \in [0,1]$. Let

$$\Phi(\alpha,\beta) = \{\boldsymbol{x} \,|\, d(\boldsymbol{x};\alpha) > \beta\}. \tag{3.4}$$

Φ is a set of points defining a solid shape dependent on the level-set value β. We define the actual interpolated shape as $\Omega(\alpha) = \Phi(\alpha,\beta_0)$ where β_0 satisfies

$$\big|\Phi(\alpha,\beta_0)\big| = (1-\alpha)\big|\Phi(0,0)\big| + \alpha\big|\Phi(1,0)\big| \tag{3.5}$$

and

$$\big|\Phi\big| = \iiint_{\Phi} dV. \tag{3.6}$$

That is, we force the volume of the shape to vary linearly throughout the interpolation by the choice of level-set value β_0. Fig. 3.2 illustrates this for a one-dimensional example (in a single dimension $\beta = 0$ always) and Fig. 3.3 for a two-dimensional example. An example of two key microstructures with solid volume fractions of 0.5 and 0.7 and the interpolated microstructure with solid fraction of 0.6 is shown in Fig. 3.4. This method is simple to implement: the volume of the shape transitions linearly and no external input is required unlike other metamorphosis methods. We next evaluate whether the method generates interpolated microstructures with appropriate physical properties.

3.2.3 Microstructure evaluation

Here we evaluate the material properties of the key structures and interpolated microstructures: we examine the bulk (K) and shear (G) moduli of C^{iso}_{ijkl}, which is the closest truly isotropic tensor to the computed material properties as defined by the measure A above.[1] Fig. 3.5 shows material properties of the key structures and the interpolated microstructures. The properties vary smoothly close to the Hashin-Shtrikman theoretical upper bounds (Hashin and Shtrikman, 1963) which are known to be tight (Norris, 1985). As there is a void phase, the lower bounds are zero. The upper bounds for a two phase design with one phase void are (Hashin and Shtrikman,

[1] We do this because G is not defined for anisotropic materials. However, the materials here are very close to isotropic so it is informative to examine the properties of the closest isotropic material.

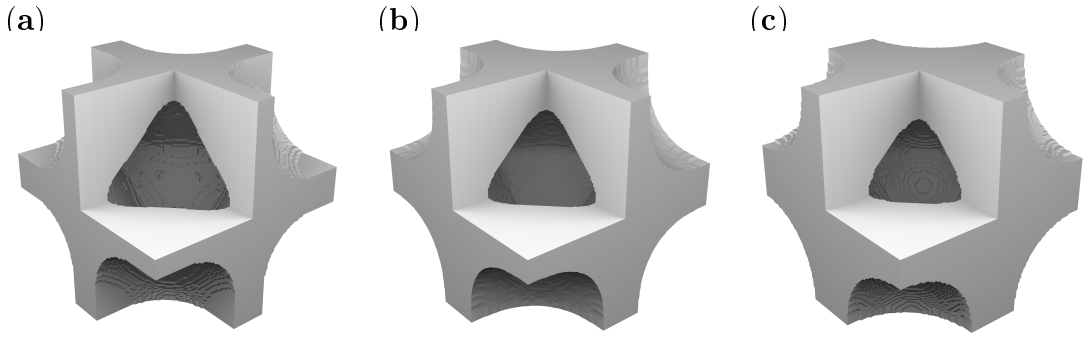

FIGURE 3.4: (**a**) Directly optimised microstructure with 50% volume fraction. (**b**) Microstructure with 60% volume fraction interpolated using the 50% and 70% volume fraction microstructures. (**c**) Directly optimised microstructure with 70% volume fraction. The front octant has been removed in each to show the inner structure.

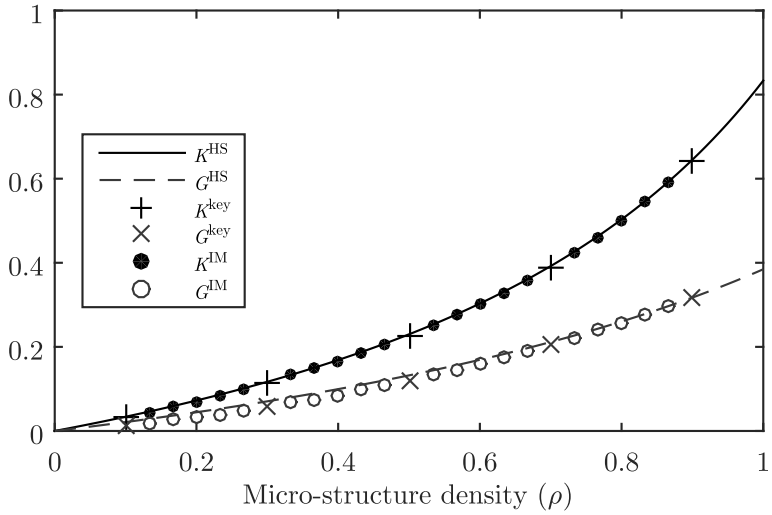

FIGURE 3.5: Hashin-Shtrikman bounds on bulk modulus K^{HS} and shear modulus G^{HS} compared to elastic properties of the key microstructures (K^{key}, G^{key}) and interpolated microstructures (K^{IM}, G^{IM})

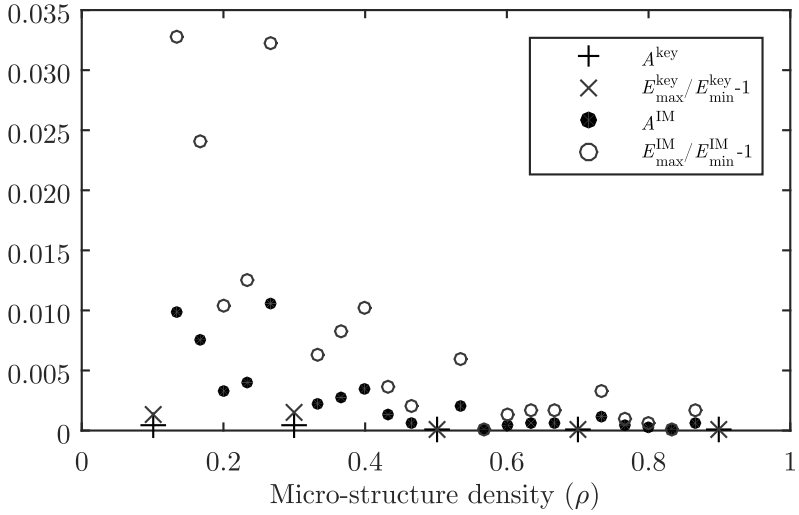

FIGURE 3.6: Anisotropy measures of the key microstructures (key) and interpolated microstructures (IM)

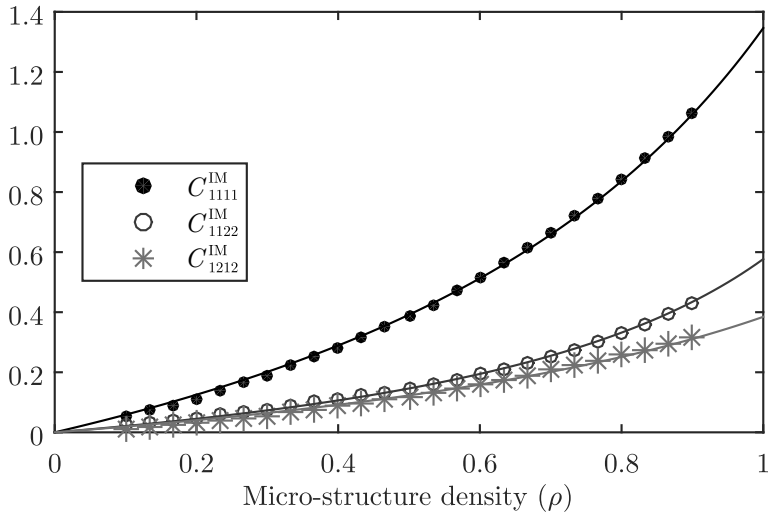

FIGURE 3.7: Model fit to the three unique elastic constants as per (3.9)

1963):

$$K^{\text{HS}}(\rho) = K_0 - \frac{1-\rho}{\frac{1}{K_0} - \frac{3\rho}{3K_0+4G_0}}, \tag{3.7}$$

$$G^{\text{HS}}(\rho) = G_0 - \frac{1-\rho}{\frac{1}{G_0} - \frac{6\rho(K_0+2G_0)}{5G_0(3K_0+4G_0)}}, \tag{3.8}$$

where K_0 and G_0 are the base material bulk and shear moduli and ρ is the volume fraction of solid material. The interpolated microstructure bulk modulus is close to the Hashin-Shtrikman upper bound, indicating that the interpolated microstructures perform just as well as those that

are directly optimised. We note that the shear modulus, which is not optimised for, suffers at low volume fractions.

While the key structures are optimised with an isotropy constraint, in practice an elastically isotropic microstructure is impossible to represent using discrete voxels. Two measures of anisotropy are examined. The first being the ratio of the Young's modulus in its maximal direction $E_{\max}$ to the Young's modulus in its minimal direction $E_{\min}$. The second measure is as specified above in (3.2) and used in the optimisation of the key microstructures (Challis et al., 2008a). Fig. 3.6 shows that the interpolated microstructures are less isotropic than the directly optimised (and actively constrained) microstructures, however the difference between $E_{\max}$ and $E_{\min}$ is never greater than 3.5% and is typically below 1.5%.

The properties of the interpolated microstructures are fit using least squares to the function

$$C^{\text{fit}}_{ijkl}(\rho) = C^0_{ijkl} - C^0_{ijkl}\frac{1-\rho}{1+a_{ijkl}\rho}. \tag{3.9}$$

This functional form matches that of the Hashin-Shtrikman bounds. Further, the fit function matches the properties of a void at $\rho = 0$ with $C^{\text{fit}}_{ijkl}(0) = 0$ and matches the base material properties at $\rho = 1$ with $C^{\text{fit}}_{ijkl}(1) = C^0_{ijkl}$. As the microstructures are cubically symmetric there are only 3 unique elastic constants in the effective stiffness tensor that are fitted. The fitted functions match the properties of the interpolated microstructures very well (Fig. 3.7) and provide a smooth relation between density and the properties of the interpolated microstructures. The simple fit functions extrapolate the properties of the interpolated microstructures below $\rho = 0.1$ and above $\rho = 0.9$. This facilitates their use for designing macroscopic structures.

We now have a continuum of microstructures of varying densities which are close to optimal (the HS bound) and which are close to isotropic. The microstructures are smooth in the sense that varying the density ρ a small amount varies the geometry a small amount, guaranteeing that structures with similar densities will connect to each other. The microstructures are also smooth in the sense that their homogenised elastic properties are smooth and fit well to a simply expressed function. These microstructures and the fitted properties can now be used to construct macroscopic designs where the density can vary at each point in the design.

3.3 Macroscopic Design Examples

3.3.1 Method

Macroscopic structures are now designed that specify the density of an interpolated microstructure at each point in the design. These MIMO designs are compared with single scale SIMP optimised designs to gauge the effectiveness and appropriateness of the method.

The compliance is minimised for 2D and 3D cantilever and bridge-like domains for a variety of loading conditions: a single point load; a single distributed load; the mean of a number of individually applied point loads; and a "worst case" loading. Compliance is commonly optimised (e.g. Bendsøe and Sigmund, 2003) and, unlike strength, is straightforward to quantify for multi-scale designs and hence is the focus for this study.

For both the MIMO and SIMP optimisations the material distribution method (Bendsøe and Kikuchi, 1988; Bendsøe, 1989) is used to optimise the designs. Discretising on a regular cubical grid with the displacement piece-wise linear and the density piece-wise constant gives the compliance minimisation problem

$$\min_{\rho(\boldsymbol{x})} \ \boldsymbol{u}^T\boldsymbol{t}$$
$$\text{subject to } \begin{cases} \boldsymbol{u} = \underset{\tilde{\boldsymbol{u}}}{\operatorname{argmin}} \left[\frac{1}{2}\tilde{\boldsymbol{u}}^T\boldsymbol{K}(\boldsymbol{\rho})\tilde{\boldsymbol{u}} + \tilde{\boldsymbol{u}}^T\boldsymbol{t}\right], \\ \frac{1}{M}\sum_{e=1}^{M}\rho_e \leq V_0, \end{cases} \tag{3.10}$$

where $\boldsymbol{u}$ is the displacement vector, $\boldsymbol{K}(\rho) = \boldsymbol{K}(C_{ijkl}(\rho_e))$ is the stiffness matrix, $\boldsymbol{t}$ is the load vector, V_0 is a material constraint, $\rho_e \in [0,1]$ is the material density in element e and M is the total number of elements.

The mean compliance problem is defined similarly to (3.10) as

$$\min_{\rho(\boldsymbol{x})} \ \frac{1}{N}\sum_{n=1}^{N}\boldsymbol{u}_n^T\boldsymbol{t}_n$$
$$\text{subject to } \begin{cases} \boldsymbol{u}_n = \underset{\tilde{\boldsymbol{u}}}{\operatorname{argmin}} \left[\frac{1}{2}\tilde{\boldsymbol{u}}^T\boldsymbol{K}(\boldsymbol{\rho})\tilde{\boldsymbol{u}} + \tilde{\boldsymbol{u}}^T\boldsymbol{t}_n\right], \\ \frac{1}{M}\sum_{e=1}^{M}\rho_e \leq V_0. \end{cases} \tag{3.11}$$

In this case the objective function is the mean compliance of N independently applied loads.

The worst case loading optimisation problem is defined as

$$\min_{\rho(\boldsymbol{x})} \max_{\boldsymbol{\alpha}} \boldsymbol{u}^T \boldsymbol{t}$$
$$\text{subject to} \begin{cases} \boldsymbol{u} = \underset{\tilde{\boldsymbol{u}}}{\operatorname{argmin}} \left[\frac{1}{2} \tilde{\boldsymbol{u}}^T \boldsymbol{K}(\boldsymbol{\rho}) \tilde{\boldsymbol{u}} + \tilde{\boldsymbol{u}}^T \boldsymbol{t} \right], \\ \frac{1}{M} \sum_{e=1}^{M} \rho_e \leq V_0, \\ \boldsymbol{t} = \sum_{n=1}^{N} \alpha_n \boldsymbol{t}_n, \\ \sum_{n}^{N} \alpha_n^2 \leq 1. \end{cases} \tag{3.12}$$

Here N loads are linearly combined with scale factors determined by $\boldsymbol{\alpha}$ where $\boldsymbol{\alpha}$ maximises the compliance for a given $\boldsymbol{\rho}$ – that is, $\boldsymbol{\alpha}$ chooses the worst case loading.

The stiffness matrix $\boldsymbol{K}$ is dependent on $\boldsymbol{\rho}$ through the elasticity tensor $C_{ijkl}(\rho)$. For the SIMP optimisations the standard fictitious material law (Rozvany et al., 1992)

$$C_{ijkl} = C^0_{ijkl} \rho^P, \tag{3.13}$$

is used (as also described in (1.1) and (2.63)). This penalises intermediate densities discouraging their use. C^0_{ijkl} matches the base material used for the microstructures with $E = 1$ and $\nu = 0.3$. For the interpolated structures, (3.9) was used as the material law with the a_{ijkl} fit as shown in Fig. 3.7.

The optimisation is performed using the implementation of the Globally Convergent Method of Moving Asymptotes (GCMMA) by Svanberg (1987, 2002). This is a more recent version of the MMA algorithm often used for structural optimisation (Svanberg, 1987). The GCMMA is guaranteed to converge to the set of points satisfying the Karush-Kuhn-Tucker (KKT) conditions while the MMA is not. The KKT conditions are a necessary but not sufficient condition for optimality.

The SIMP designs are "sharpened" post-optimisation to remove the soft, intermediate valued elements of the design and attain a true 0-1 design. The sharpened density $\rho_{\mathrm{s}}(\boldsymbol{x})$ is related to the optimised, "raw" density $\rho_0(\boldsymbol{x})$ by

$$\rho_{\mathrm{s}}(\boldsymbol{x}) = \begin{cases} 1, & \rho_0(\boldsymbol{x}) \geq \gamma, \\ \rho_{\min}, & \text{otherwise}, \end{cases} \tag{3.14}$$

where γ is chosen to satisfy the volume constraint. In sharpening, it is possible that in applying (3.14) the load is no longer supported or structural members become detached. In such cases select elements are forced to be solid prior to sharpening. Sharpening a SIMP optimised result to a 0-1 design removes the penalised intermediate values and in the examples considered results in a better performing structure.

For this work, a fixed 160 iterations was used to avoid the difficult problem of defining a robust convergence condition: a range of convergence conditions were tested but each condition terminated some optimisations too early or much too late. All of the optimisation histories demonstrated convergence in the objective within these 160 iterations. The initial design was $\rho(\boldsymbol{x}) = 1$ with a target volume fraction of $V_0 = 0.2$. A continuation method was used for the SIMP optimisation: initially, the exponent $P = 1$ in (3.13), with P rising linearly to $P_{\max}$ over the first 120 iterations. $P_{\max}$ varied depending on the problem, with $P_{\max} \in [3.5, 5]$. All objective results quoted use $P_{\max} = 5$ to provide a fair comparison.

3.3.2 Results

We tested the method in cantilever and bridge-like macroscopic design problems in both two and three dimensions. Four different objectives were used, a single point load with (3.10), a single distributed load with (3.10), the average of multiple different load cases with (3.11), and the worst case of multiple combined loads with (3.12). Schematics of the different load cases are shown in Fig. 3.8 for 2D and Fig. 3.9 for 3D.

The optimised SIMP and MIMO designs are shown in Fig. 3.10, Fig. 3.11 and Fig. 3.12. The objectives of the optimised designs are shown in Table 3.1 and a graphical representation can be seen in Fig. 3.13. The use of intermediate density microstructures within the MIMO optimised designs is shown in Fig. 3.14.

3.4 Discussion

3.4.1 Evaluation of MIMO designs

The proposed MIMO method in 2D produces optimised designs that typically utilise intermediate density microstructures extensively, as shown in Fig. 3.14. However, the bridge with a simple point load (problem a) makes little use of intermediate density elements. This shows that the small penalisation represented by (3.9) is enough to discourage intermediate density

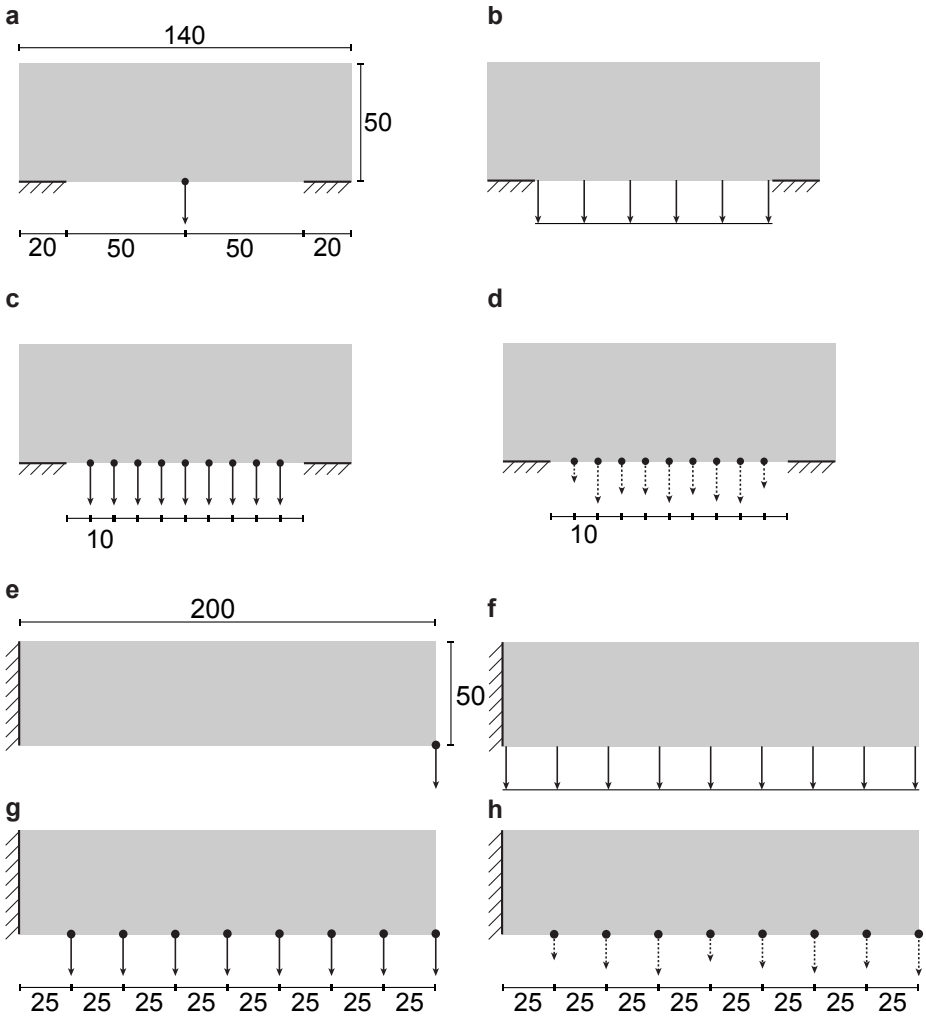

FIGURE 3.8: Schematics of the 2D macroscopic optimisation problems, dimensions in number of unit square elements. (**a**) Bridge with a single point load. (**b**) Bridge with a distributed load. (**c**) Bridge, mean of 9 independent load cases. (**d**) Bridge with the worst case out of a linear combination of 9 loads. (**e**) Cantilever with a single point load. (**f**) Cantilever with a distributed load. (**g**) Cantilever, mean of 8 independent load cases. (**h**) Cantilever with the worst case out of a linear combination of 8 loads.

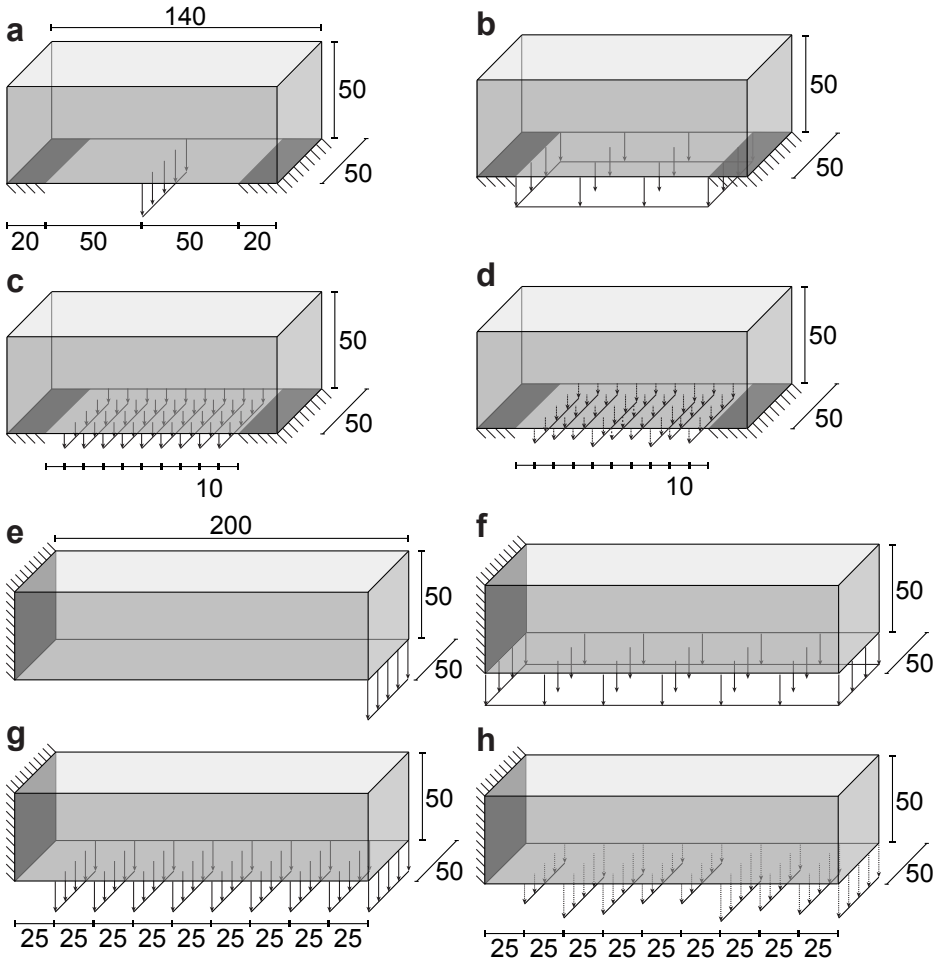

FIGURE 3.9: Schematics of the 3D macroscopic optimisation problems, dimensions in number of unit cubic elements. (**a**) Bridge with a single load. (**b**) Bridge with a distributed load. (**c**) Bridge, mean of 9 independent load cases. (**d**) Bridge with the worst case out of a linear combination of 9 loads. (**e**) Cantilever with a single load. (**f**) Cantilever with a distributed load. (**g**) Cantilever, mean of 9 independent load cases. (**h**) Cantilever with the worst case out of a linear combination of 9 loads.

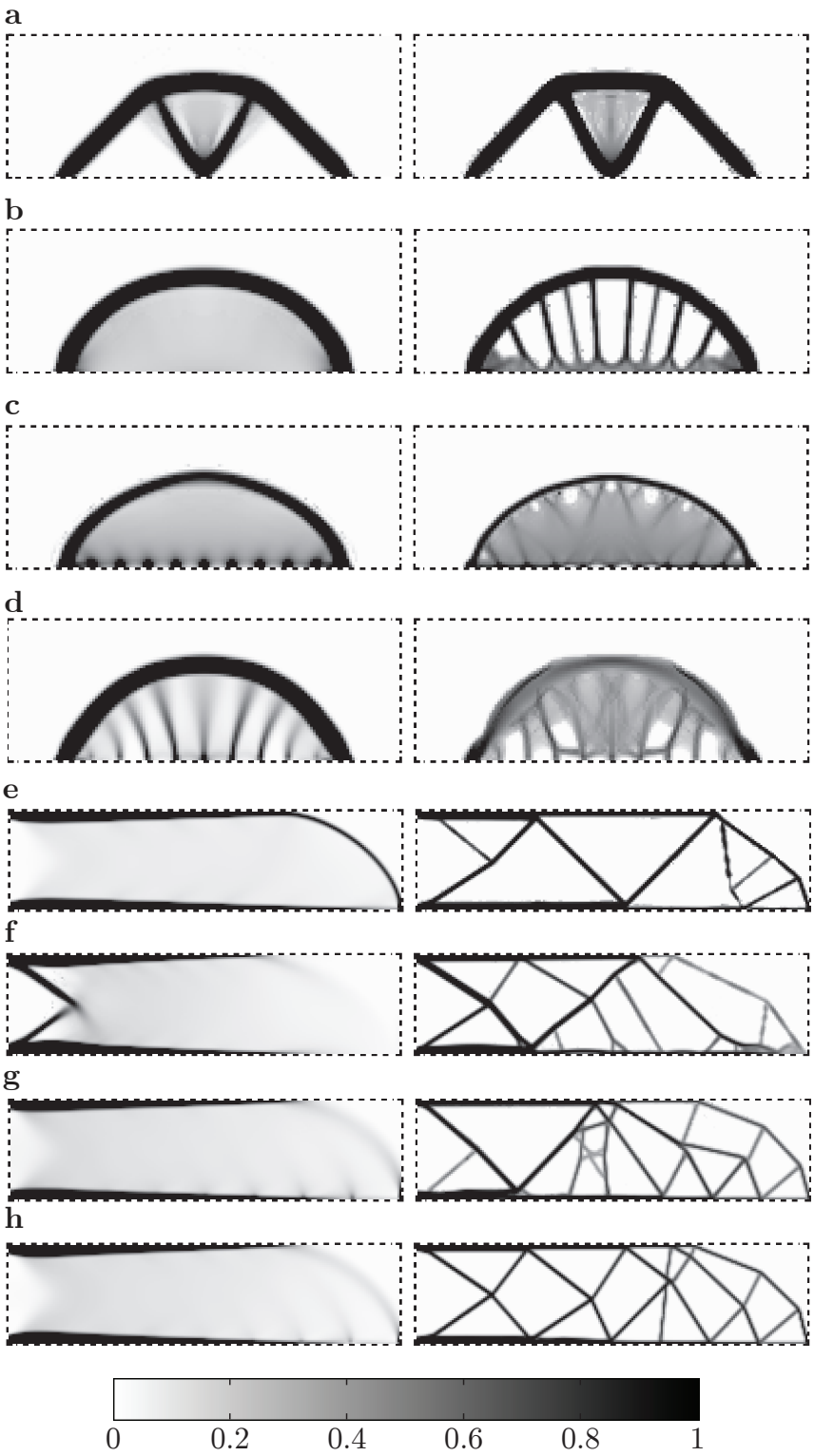

FIGURE 3.10: Optimised designs for the 2D problems, on the left is the MIMO solution and on the right is the SIMP solution. The letters correspond to those in Fig. 3.8: (**a**) Bridge, point load. (**b**) Bridge, distributed load. (**c**) Bridge, mean load. (**d**) Bridge, worst case. (**e**) Cantilever, point load. (**f**) Cantilever, distributed load. (**g**) Cantilever, mean load. (**h**) Cantilever, worst case.

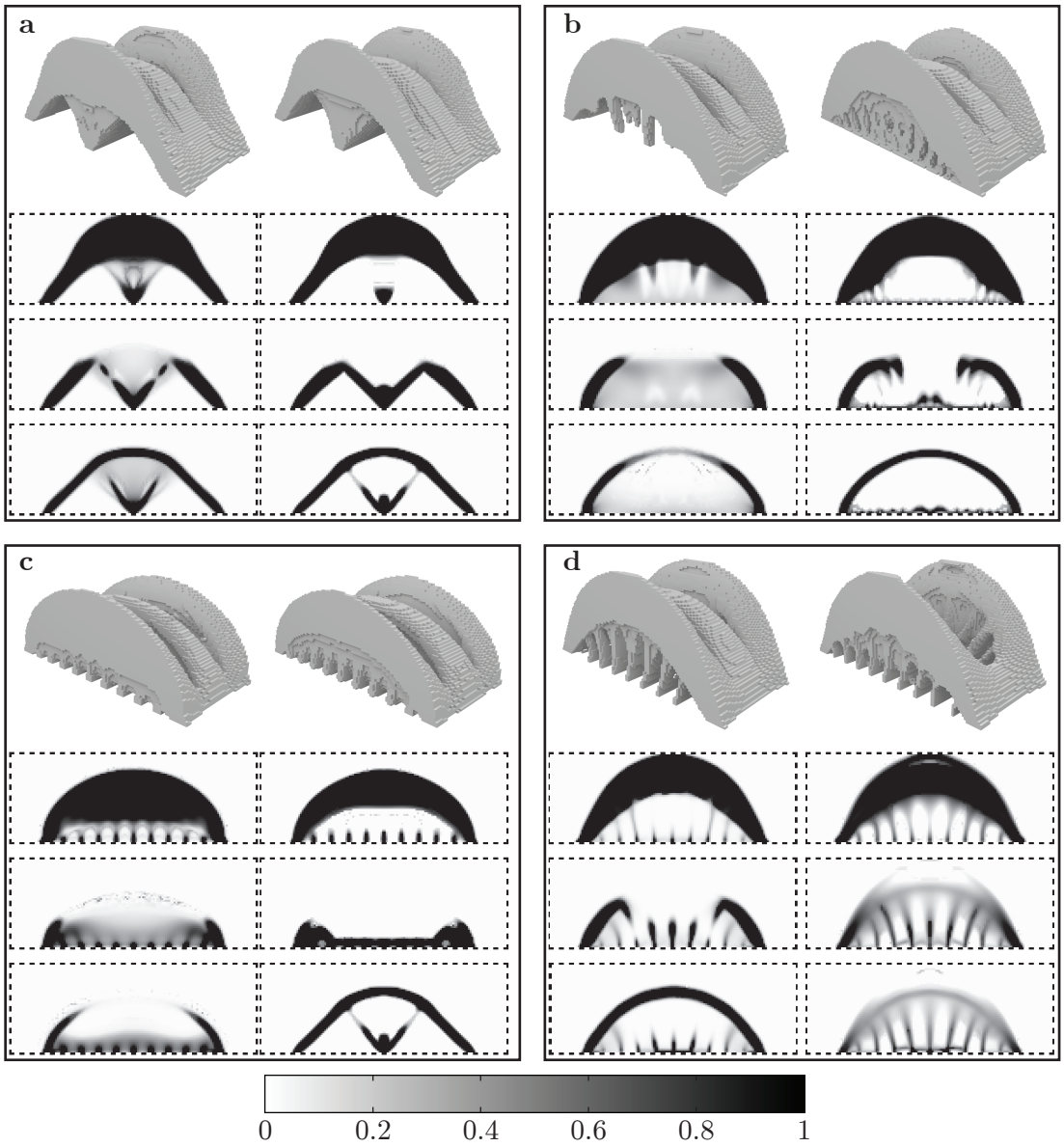

FIGURE 3.11: Optimised designs for the 3D bridge problems. In each part the MIMO design is on the left while the SIMP solution is on the right, the top image is a render of the 50% density level set while the lower images are vertical slices of the density at y =1, 10 and 20. The letters correspond to Fig. 3.9: (**a**) Point load. (**b**) Distributed load. (**c**) Mean load. (**d**) Worst case.

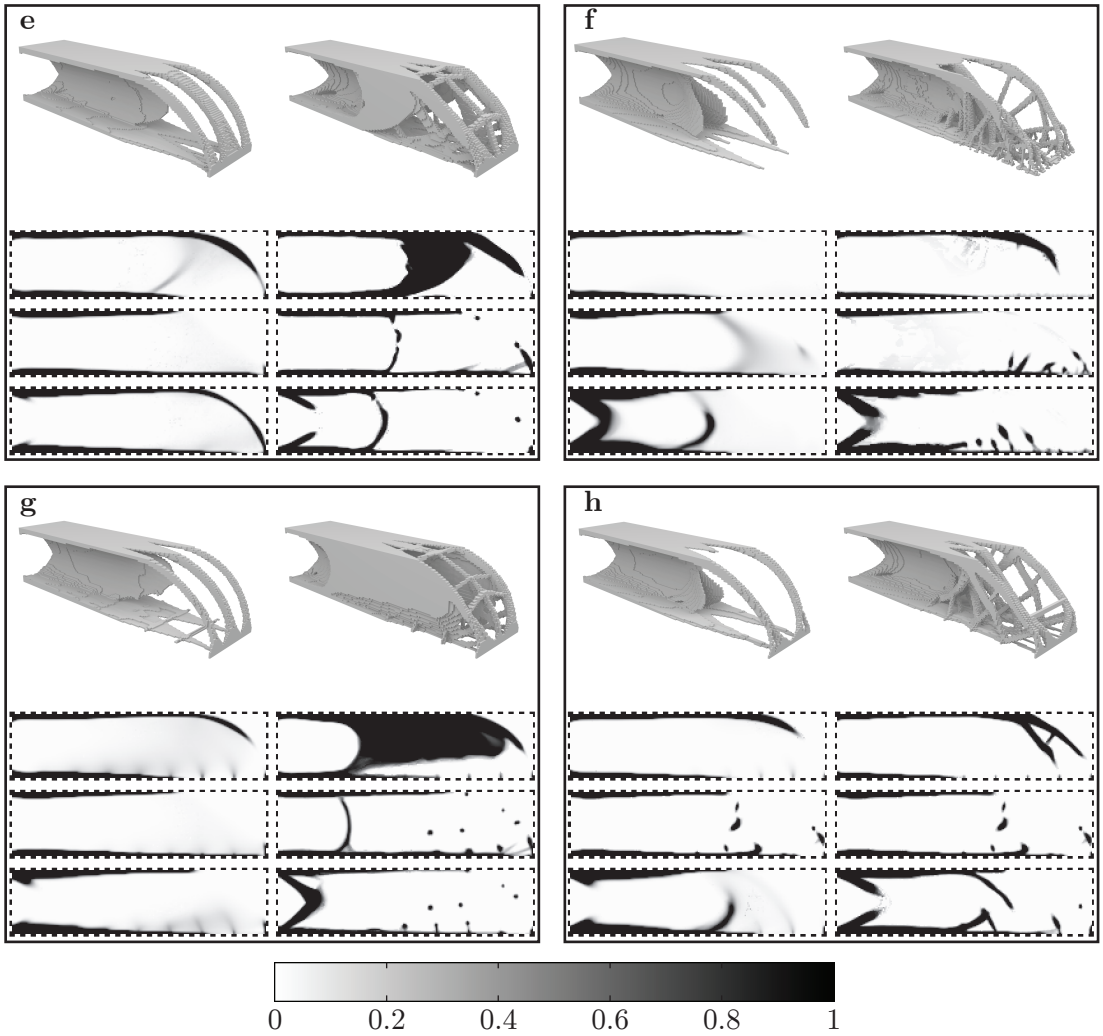

FIGURE 3.12: Optimised designs for the 3D cantilever problems. In each part the MIMO design is on the left while the SIMP solution is on the right, the top image is a render of the 50% density level set while the lower images are vertical slices of the density at y =1, 10 and 20. The letters correspond to Fig. 3.9: (**e**) Point load. (**f**) Distributed load. (**g**) Mean load. (**h**) Worst case.

TABLE 3.1: Compliance objective values for the optimised SIMP design, sharpened 0-1 design and MIMO design for each test problem

2D

Problem	SIMP	Sharpened	MIMO
a	1.59×10^1	1.43×10^1	1.34×10^1
b	7.39×10^4	5.71×10^4	5.38×10^4
c	7.68×10^1	3.13×10^1	1.63×10^1
d	4.03×10^2	2.31×10^2	6.41×10^1
e	9.77×10^2	8.42×10^2	7.98×10^2
f	7.26×10^6	6.62×10^6	4.71×10^6
g	6.07×10^2	5.00×10^2	2.96×10^2
h	3.10×10^3	2.17×10^3	1.97×10^3

3D

Problem	SIMP	Sharpened	MIMO
a	7.09×10^2	6.56×10^2	7.00×10^2
b	3.21×10^6	2.64×10^6	2.77×10^6
c	7.39×10^2	6.50×10^2	6.92×10^2
d	1.07×10^4	4.03×10^3	3.22×10^3
e	4.24×10^4	3.85×10^4	3.82×10^4
f	2.63×10^8	2.28×10^8	2.17×10^8
g	1.82×10^4	1.46×10^4	1.37×10^4
h	9.87×10^4	9.02×10^4	8.98×10^4

microstructures in this case; i.e. they are not beneficial for the optimisation objective. In 3D, we do not see such extensive use of intermediate densities in the MIMO designs (Fig. 3.14). Our explanation for this is that the extra freedom offered by the third spatial dimension reduces the utility of varying the material density throughout the design.

Fig. 3.14 also shows that nearly all of the optimised MIMO designs have at least 10% of their elements with densities above 0.9. This reflects the fact that the designs tend to have a solid outer load-bearing shell. The benefit of this solid outer shell is evident in numerous applications. For example, see the second moment of inertia which features in the Euler-Bernoulli bending beam equation. This is why an I-beam is appropriate for a number of engineering applications: a significant portion of the material is placed far from the neutral axis at the top and bottom while the smaller amount of material left resists shearing. The MIMO designs, particularly in the two-dimensional cases e-h, resist this shearing more efficiently with microstructures than their SIMP counterparts can with only truss-like structures (Fig. 3.10). While the two-dimensional e-h designs used intermediate density microstructures to resist shearing the three-dimensional e-h designs imitate the I-beam design by linking the two extremes with a solid, thin, vertical member which is allowed by the third spatial dimension.

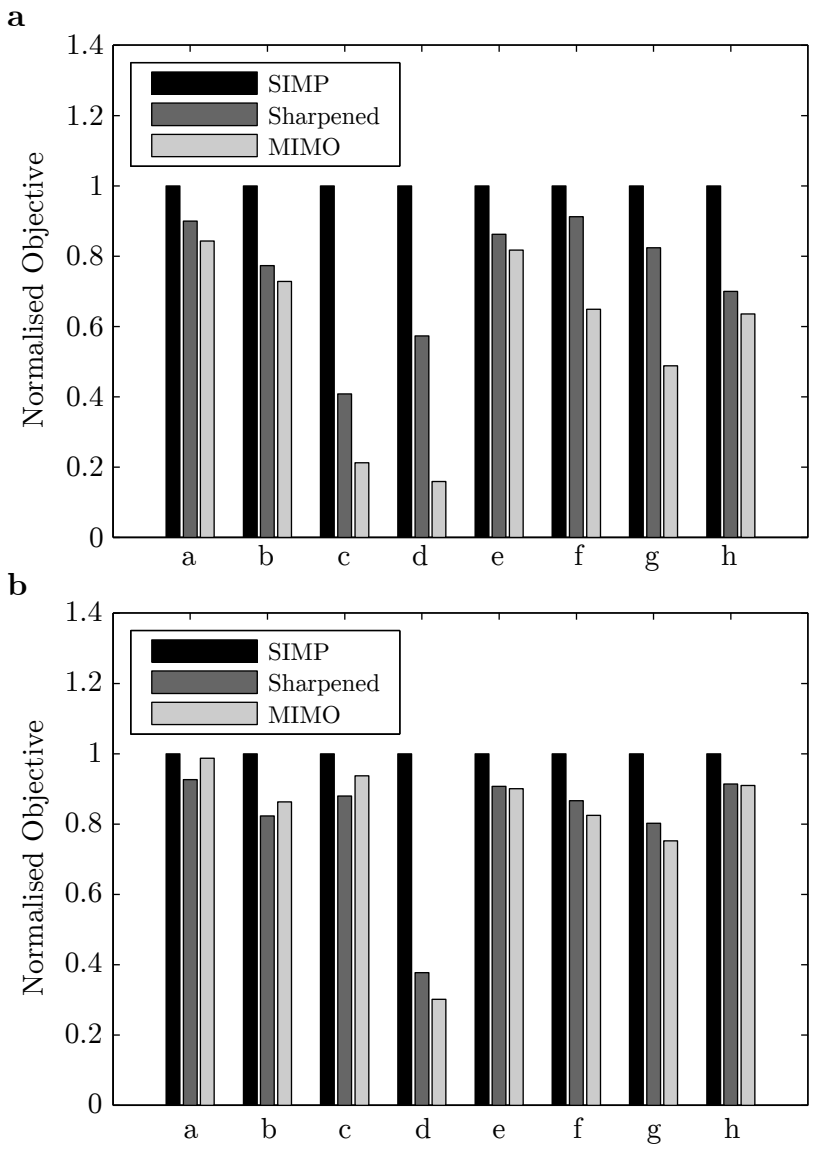

FIGURE 3.13: Optimised compliance objective values for each test problem normalised by the objective of the SIMP optimised design. (**a**) 2D. (**b**) 3D.

The proposed MIMO method finds optimised macroscopic designs that have better objective values than designs optimised via the SIMP method. This is to be expected: Any elements with intermediate densities that appear in the SIMP solutions have heavily penalised elastic properties compared to such elements within the MIMO designs. It is more appropriate to compare the MIMO objective values to those of the 0-1 designs that have been obtained by sharpening the SIMP optimised solutions. In 2D, the MIMO designs have better objective values than the 0-1 designs for all of the examples considered here (see Fig. 3.13a). In these cases the MIMO final objective values outperform those of the 0-1 designs by as much as 70%, which occurs for the bridge with the worst case loading. We note that for the bridge examples

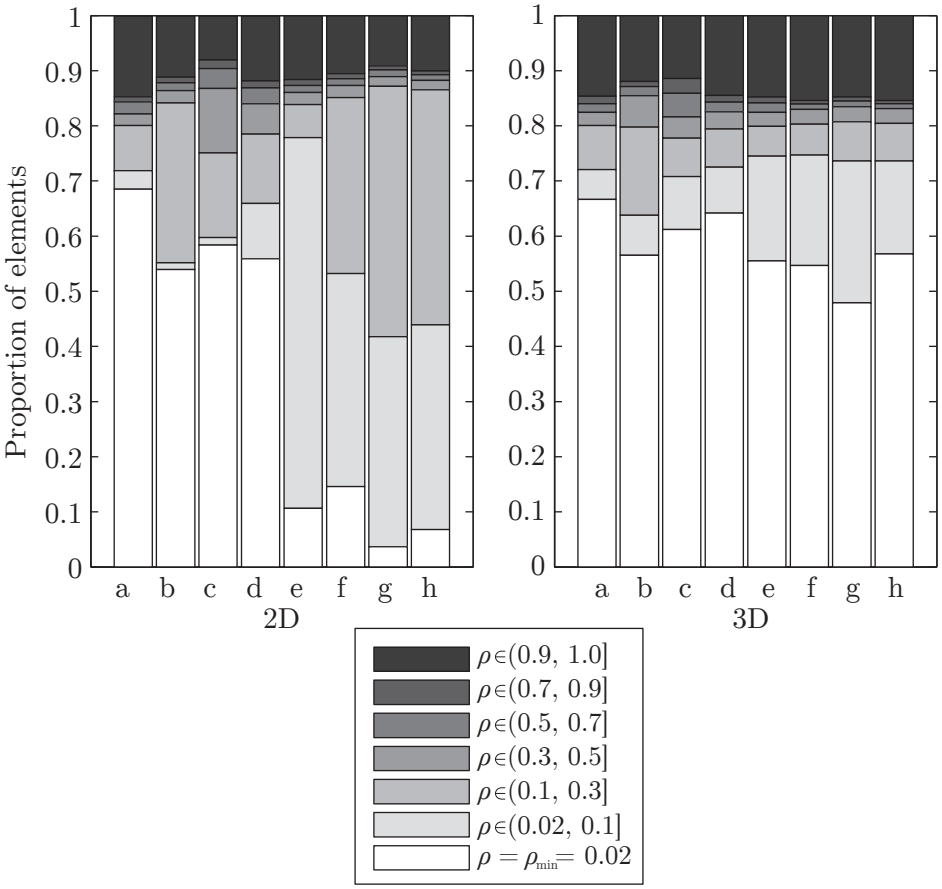

FIGURE 3.14: Proportions of elements grouped by density within the optimised MIMO designs

with the mean and worst case loadings (c and d) the GCMMA algorithm struggled to find a solid-void SIMP solution.

The more effective load distribution possible with the MIMO designs appears most beneficial in 2D for complex load cases such as the distributed, mean and worst-case optimisation problems, as particularly evidenced by the cantilever examples (f, g and h). These multiple-scale 2D MIMO designs could be produced using laser or water cutting, for example, if 2D microstructures were used instead of the 3D microstructures used in this work. Unfortunately, the nature of non-linear optimisation inhibits the ability to make strong statements about benefits of the method for a general optimisation problem. Future work could include a full study on the method confined to two dimensions contrasting MIMO to known truss solutions, such as those suggested by Rozvany et al. (2006).

Unlike the 2D examples, for many of the 3D examples the MIMO solutions do not give a improvement in the objective value compared to what is achieved with the 0-1 sharpened SIMP design (see Fig. 3.13b). This is surprising: the interpolated microstructure design space is a

super-set of the solid-void problem and thus is guaranteed to have an optimum no worse than the solid-void problem, as can be seen comparing the MIMO objectives to the original SIMP results prior to sharpening. Further analytical results are difficult to obtain so we cannot be certain that the results found here generalise to any specific class of problem. However, from the results presented here it is quite clear that excellent designs for the compliance minimisation problem can be achieved in 3D without utilising the intermediate densities available with the MIMO method. This highlights the importance of comparing the results of new methods to those achieved by more standard techniques. Here, the comparison suggests that the additional complexity of multiscale optimisation methods may not be warranted for 3D compliance minimisation problems if the microstructures are constrained to be isotropic.

3.4.2 Advantages of the MIMO approach

Our proposed method has significant advantages in terms of computational complexity compared to multiscale optimisation methods that have previously been proposed. Specifically, the MIMO method is no more computationally expensive[2] than other material distribution methods once the smoothly varying set of microstructures has been determined: the microstructural optimisation and interpolation do not need to be repeated for different macroscopic designs provided the same microstructural properties are desired. Further, the separation between the microstructural and macroscopic optimisations means that the designer can directly control the choice of microstructures. For example, optimisation methods have multiple parameters and a parameter sweep can be performed and the preferred microstructure could then be selected. This approach has been used here but would be infeasible for an integrated multiscale approach (e.g. Rodrigues et al., 2002). The separation between the choice of microstructures and the macroscopic optimisation also facilitates the use of the MIMO method for new applications where additional microstructural objectives and constraints are needed. For example, open microstructures with connected a pore space could be forced by including a conductive void phase and conductivity in the microstructural design objective function (e.g. Challis et al., 2008a); this method of ensuring a connected pore space is used to good effect in Chapter 4.

A further significant advantage of the MIMO method is that it ensures smoothness and connectedness of the microstructures within the macroscopic design. As discussed in Section 1.2.3, this was a particular motivation for the current work. We note that the lack of enforced smoothness and connectedness in previous multiscale design approaches (Rodrigues et al., 2002; Coelho et al., 2008) can be alleviated using techniques such as those detailed for FGMs by Zhou and

[2]Time comparisons would be unfair due to external influences, these include other traffic on the compute cluster and the non-deterministic connectivity of the resource allocation.

Li (2008a). Zhou and Li (2008a) enforce connectivity of a changing microstructure with three techniques: specifying material at connection points as an optimisation constraint; adding 'pseudo-loads' to desired connection points; and by adding a non-linear diffusion term to the global optimisation. Each of these methods could be adapted into the multiscale optimisation method. However, the first two would remove generality by specifying the loading points and the last would be difficult to implement and computationally expensive in three dimensions, perhaps prohibitively so.

3.4.3 MIMO applications and extensions

Although the MIMO method has not provided significant improvements in the compliance objectives for the 3D optimisation examples considered here, there are a number of application areas where the MIMO approach would be beneficial. Kuiper and Huiskes (1997) optimised the Young's modulus throughout 2D bone prosthetics to reduce bone resorption. More recently Arabnejad Khanoki and Pasini (2012) optimised bone resorption using a multi-scale approach, also in 2D. The MIMO approach would be a natural choice for extending this work to 3D providing two key benefits. Firstly, the smoothness of the interpolated microstructures would make it possible to construct a physical prototype. Secondly, by utilising optimised open cell microstructures, MIMO designs can provide an interconnected pore space for bone ingrowth. This is explored in the following chapter (Chapter 4).

Another application is functionally graded materials (FGMs), where a material smoothly changes its properties along a particular spatial direction (Niino and Maeda, 1990). Functionally graded materials with varying Young's modulus have been designed using inverse homogenisation (Birman and Byrd, 2007), and techniques have been developed to ensure connectivity of the design (Zhou and Li, 2008a). We note that designing a functionally graded material using MIMO would be simple once the space of smoothly varying interpolated microstructures has been found: inverting (3.9) gives a microstructure for any required Young's modulus, and a prescribed continuous curve for the Young's modulus would result in a smoothly changing microstructure. An example of this application can be found in Chapter 5.

The MIMO method proposed here could be extended to remove the isotropy constraint on the microstructures. The isotropy constraint simplifies the macroscopic design problem: only the density of the microstructure needs to be determined within each element of the macroscopic structure. It also allows us to compare the elastic properties of the interpolated microstructures to the Hashin-Shtrikman upper bounds (Hashin and Shtrikman, 1963), demonstrating that the interpolated microstructures are close to optimal. In nature, microstructures appear in many organisms such as trees (Gibson, 2012), butterfly wings (Michielsen and Stavenga, 2008) and

seashells (Shepherd et al., 1995) which are all in a sense optimised and efficient. We note that these microstructures are not isotropic and in later chapters we seek a smooth space of optimised microstructures that are not isotropic. In such a case there will be significant directional dependence of the material properties leading to additional design variables. The new freedom provided by the anisotropy of the microstructures may give new insights and improved objective values.

3.5 Conclusion

In this chapter we have proposed the MIMO method of interpolating microstructures for use in macroscopic design using the material distribution method. The microstructure interpolation was found to provide a smoothly varying space of microstructures which were close to optimal. The approach overcomes a shortcoming of earlier multiscale methods: connections between nearby microstructures are guaranteed, meaning that designs are physically interpretable.

Macroscopic designs optimised for minimum compliance using the MIMO microstructures were compared to those optimised using a SIMP material law and subsequently sharpened to give 0-1 designs. The MIMO designs demonstrated improved compliance for the 2D problems with complex load cases but not for the 3D problems. While the additional complexity of the MIMO method may not be warranted for minimising compliance, the method may be useful in other cases where a particular class of microstructures is desirable, such as in designing bone prosthetics. These results also highlight a need to test newly developed algorithms against existing methods.

In the following chapters we apply the MIMO method to the design of bone prosthetics (Chapter 4), and we extend the method to anisotropic microstructures with a multidimensional parameterisation (Chapter 5).

Chapter 4

Application to Bone Prosthesis Design

In Chapter 3 we developed a method to smoothly interpolate microstructures for use in the material distribution method, named microstructure interpolation for macroscopic optimisation (MIMO). We found that the method provided a benefit for two-dimensional compliance problems while three-dimensional compliance problems resulted in optimised designs of mainly solid or void microstructures with little benefit above traditional, exclusively solid-void designs.

In this chapter we consider the design of femoral implants using multiscale structural optimisation with the MIMO method. Femoral implant objective functions do not typically include stiffness and require more subtle designs. Kuiper and Huiskes (1997) optimised femoral implants under the assumption that the Young's modulus of the material can be varied throughout the design. Arabnejad Khanoki and Pasini (2012) used two-dimensional square lattice microstructures to produce such a varying meta-material. Here we approach the problem with the MIMO method allowing three-dimensional designs and more general microstructures.

4.1 Introduction

When designing femoral implants it is important to reduce the chance of implant failure, which is primarily caused by loosening of the prosthetic from the bone (aseptic loosening) (Malchau et al., 2002). Aseptic loosening leads to revision surgeries which are costly and cause patient discomfort. Mathematically, the chance of implant failure is typically quantified as a function of the stress on the interface between the prosthetic and the existing bone (Kuiper and Huiskes, 1997; Arabnejad Khanoki and Pasini, 2012; Chanda et al., 2015b), however fatigue has been considered (Arabnejad Khanoki and Pasini, 2013). A second major consideration in implant design is how much existing bone material will be removed by the body in response to changed loading conditions, termed bone resorption (Engh et al., 1992). Bone resorption needs to be controlled and minimised.

Early work that applied structural optimisation to implant design began with that by Kuiper and Huiskes (1997). In an effort to address aseptic loosening they optimised the design of a two-dimensional hip prosthesis with an objective based on the shear stress between the implant and the bone under a simple bending moment. The amount of bone resorption was constrained and quantified using the change in strain energy upon insertion of the implant. A spatially varying Young's modulus for the prosthesis was optimised, however they did not identify what materials or microstructures might be used to obtain such varying effective material properties. It was clear from their work that the shear stress objective is opposed to the bone resorption constraint. That is, for constant Young's modulus designs, stiffer designs had well distributed stress but a large amount of bone resorption while a soft, low stiffness prosthesis led to more concentrated stress and low bone resorption.

More recent research has expanded on the ideas explored by Kuiper and Huiskes (1997). Fraldi et al. (2010) used the solid isotropic material with penalisation (SIMP) method (Bendsøe and Sigmund, 2003) to optimise a femoral implant making use of computed tomography (CT) data for the geometry. The SIMP method maximised the stiffness of the combined femur and implant under four loads in order to distribute stress in the existing bone. The CT data provided a realistic optimisation domain, and the multiple loads were more representative of the true loads expected for such an implant. Arabnejad Khanoki and Pasini (2012) used a genetic algorithm to obtain a Pareto-optimal front for an objective combining the resorption (as quantified by Kuiper and Huiskes, 1997) and an interface failure function based on the multi-axial Hoffman brittle failure criteria (Hoffman, 1967). They optimised a porous 2D implant design with a microstructure comprised of a varying hollow square lattice. A plastic proof-of-concept was produced with additive manufacturing. Chanda et al. (2015b) used a multi-objective genetic algorithm to optimise the shape of a femoral implant, also making use of CT data to provide the problem geometry. The optimised design variables were the shape of four elliptical cross sections allowing a fully solid, easily manufacturable design. The objective functions quantified proximal bone resorption through the change in strain energy similar to Kuiper and Huiskes (1997), while failure was quantified using the Hoffman failure criteria (Hoffman, 1967).

Here we optimise porous femoral implants using a number of different microstructure sets, allowing us to consider how changing the microstructure affects the shear stress objective and the implant designs. We use our previously developed MIMO approach (Chapter 3) where interpolation between optimised microstructures is utilised to generate a smoothly varying set of microstructures. The design variables in the subsequent optimisation of macroscopic properties are the density of the microstructure within each element of the macroscopic design. The smoothly changing geometry of the microstructures in the MIMO approach means that the resulting porous designs are physically realisable: microstructures from the same set will

TABLE 4.1: Descriptions of the four sets of microstructures considered

Label	Isotropic	Optimised	Description
A	yes	yes	optimised for bulk modulus and a connected pore space
B	no	no	axis-aligned cubic cross structure
C	no	yes	optimised for bulk modulus and a connected pore space
D	no	yes	same as C but rotated about the y-axis by 45°

share a common geometry and therefore will connect across elements.

The work presented here extends Arabnejad Khanoki and Pasini's (2012) use of spatially varying microstructures for the femoral implant problem into 3D. Our approach is also more general, allowing the microstructures to be numerically created via optimisation (or otherwise), without the need for an explicit description. We use 3D generalisations of the loading, shear stress objective and bone resorption constraint from the earlier work of Kuiper and Huiskes (1997). A coarse-scaled prototype design is fabricated using the additive manufacturing technology *selective laser melting* (SLM). When new improvements in the resolution achievable with additive manufacturing technologies (Zheng et al., 2014) become more readily available, our designs will be manufacturable with microstructures at the fine scale needed for porous femoral implants.

The remainder of the chapter is as follows. The microstructure sets, femoral implant optimisation problem and optimisation methods are explained in Section 4.2. Results are presented and discussed in Section 4.3. Concluding remarks are given in Section 4.4.

4.2 Methods

4.2.1 Microstructures

Four microstructure sets are considered (Fig. 4.1, Table 4.1) for use in the macroscopic optimisation. Each set spans a range of volume fractions (or densities), ρ, and have properties and geometry that vary continuously and smoothly. This allows the optimiser to choose a microstructure from the set via the choice of the design variable ρ.

The first set, labelled A, are elastically isotropic microstructures optimised for the bulk modulus of the solid phase and conductivity of the void phase. They are optimised using the method described by Challis et al. (2008a). By optimising the effective conductivity of the void phase

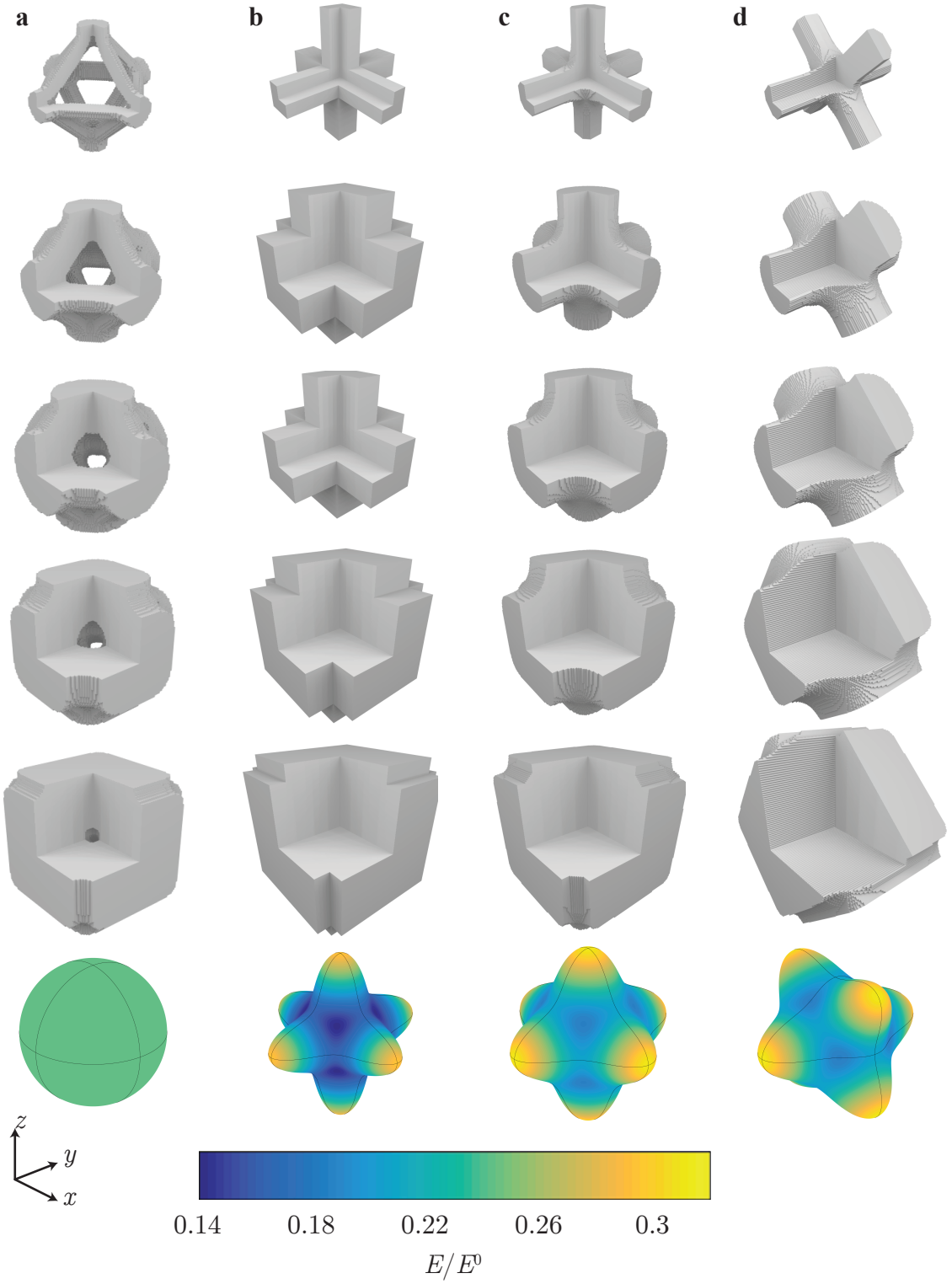

FIGURE 4.1: Visualisation of the microstructure sets used. Base cells shown at volume fractions of 10%, 30%, 50%, 70% and 90% from top to bottom. The front octant has been removed to show internal structure. The bottom most picture visualises directional dependence of the Young's modulus (E) for the 50% volume fraction microstructure as a fraction of the base material Young's modulus (E^0). (**a**) Microstructure set A. (**b**) Microstructure set B. (**c**) Microstructure set C. (**d**) Microstructure set D.

with appropriate weighting we ensure that the pore space is connected. The second set, B, are cubic cross structures, oriented such that the arms align with the cardinal axes. For the third set, C, we consider microstructures optimised for the bulk modulus of the solid phase and conductivity of the void phase as for A, but without the elastic isotropy constraint. This microstructure at 50% volume fraction has been shown to match the Schwarz P minimal surface (Torquato and Donev, 2004) and can be considered as a 'smoothed' cross microstructure with no sharp corners. The final set, D, are microstructures derived from set C but rotated by 45° about the y-axis. Microstructures in set D are less stiff in the x and z axial directions, and instead have high stiffness along the diagonals in the x-z plane (Fig. 4.1d). Further, set D microstructures are stiff along the y-axis similar to sets B and C. Set D is obtained by rotating the microstructures (including the periodic boundary conditions) without the need to re-optimise the microstructure geometry as there is no requirement that the axes of the microstructure base cells align with the macroscopic elements or axes.

Manufacture via SLM requires subsequent removal of unmelted metal powder. As such, all microstructures have a fully connected pore space to allow for this. Two isotropic base materials are considered for the implants, both have a Poisson's ratio $\nu = 0.3$ and the Young's modulus for each is $E_1 = 60$ GPa and $E_2 = 100$ GPa. These choices approximate the properties of two biocompatible titanium alloys that are currently available for processing via SLM: The low-modulus alloy Ti-24Nb-4Zr-8Sn, and the more commonly used Ti-6Al-4V (Head et al., 1995; Zhang et al., 2011; Challis et al., 2014b).

For the optimised microstructure sets (A, C and D) we can only optimise a finite number of microstructures. To provide a smooth set of microstructures without simultaneous multi-scale optimisation, we interpolate between a discrete number of optimised structures using the method described in Chapter 3. For microstructure sets A, C, and D, 5 key microstructures are directly optimised at volume fractions $\rho \in \{0.1, 0.3, 0.5, 0.7, 0.9\}$. Calculated and interpolated material properties for the microstructure sets can be seen in Fig. 4.2.

The effective material properties of the interpolated microstructures change smoothly as the volume fraction changes. This allows the effective material properties to be interpolated for the macroscopic structure optimisation, saving the cost of homogenisation calculations for every density used. Cubic splines are used for this interpolation.

For the set B, while no optimisation is required to obtain the geometry, we have not found an explicit, closed form description of the material properties for this set. Thus, material properties for set B are calculated for a number of microstructures at varying densities and are interpolated for the intervening densities. In addition to being more efficient than running

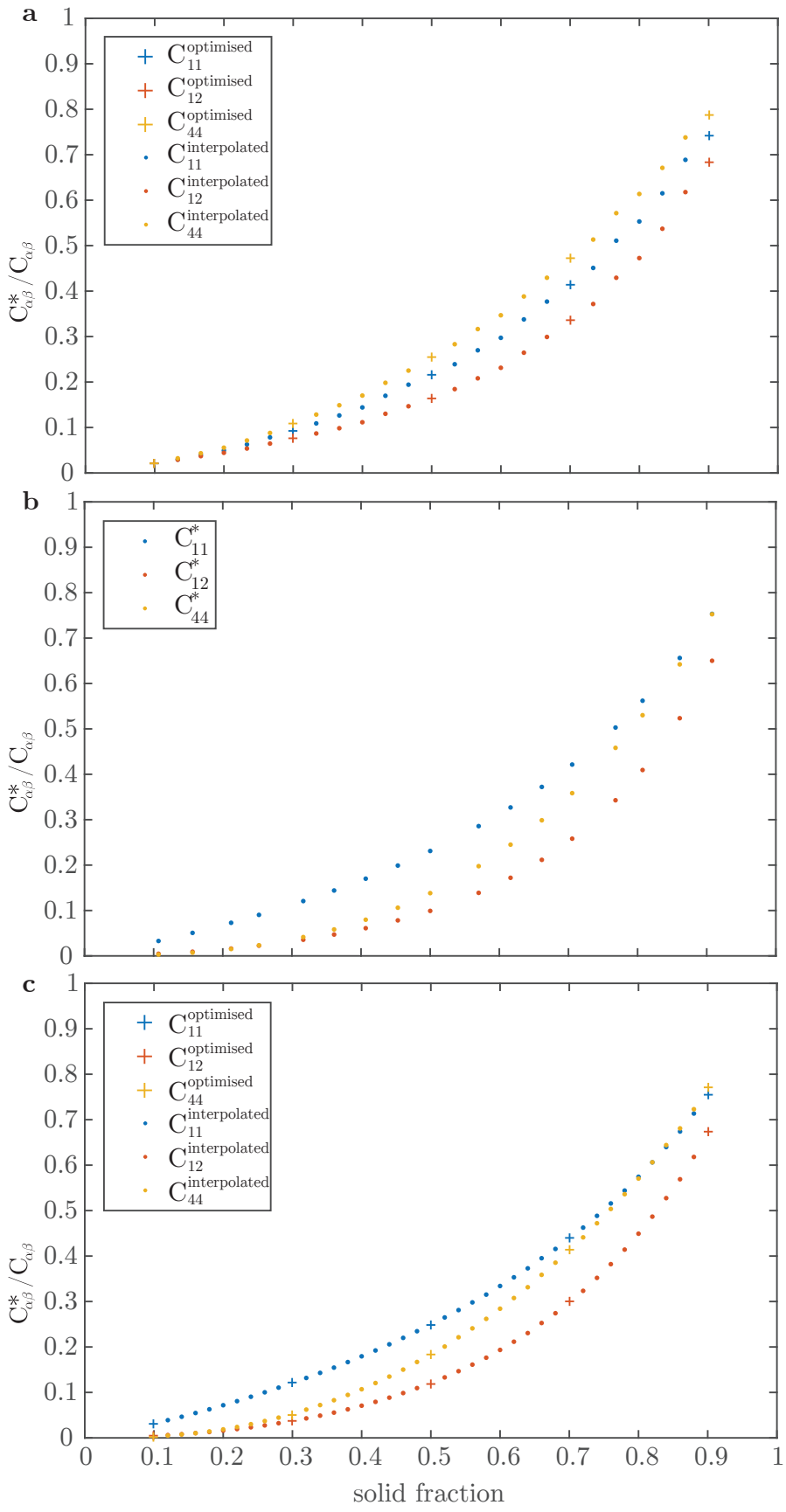

FIGURE 4.2: Microstructure properties over varying volume fractions. (**a**) Set A. (**b**) Set B. (**c**) Set C.

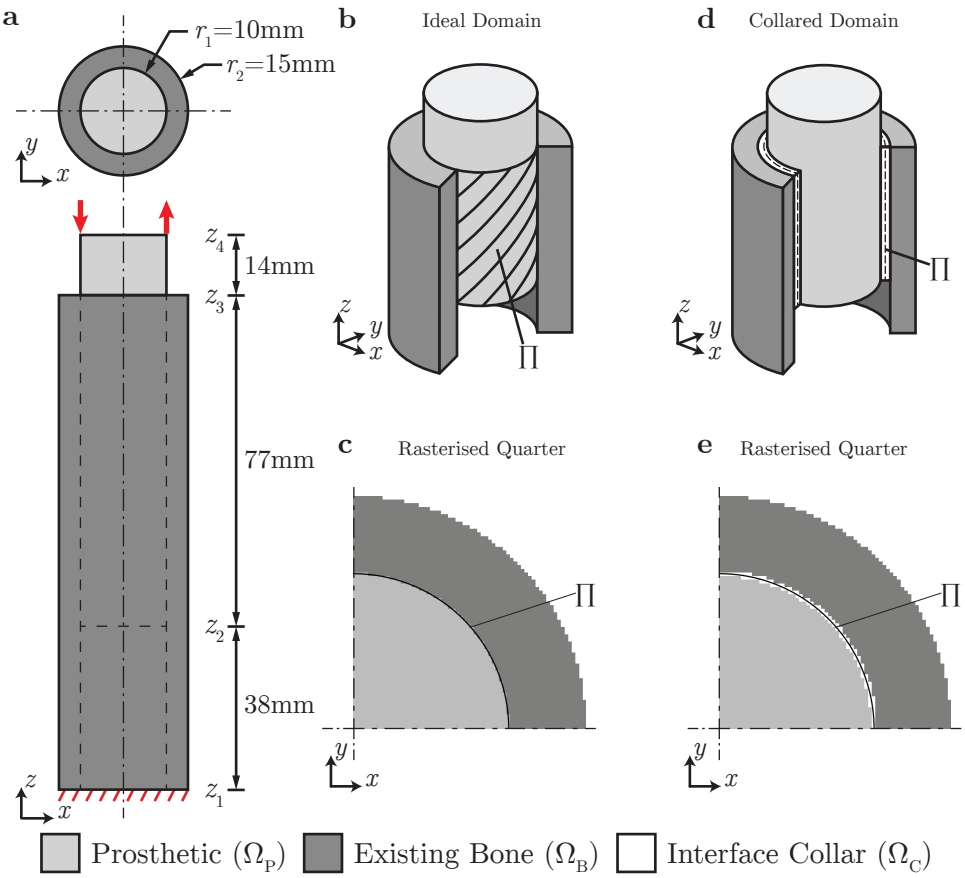

FIGURE 4.3: Schematics of the domain used for the femoral implant problem. (**a**) Orthographic schematic of the idealised design domain, with proximal torsion and fixed distal boundary conditions shown. (**b**) Isometric sketch of ideal domain. (**c**) 2D slice of rasterised ideal domain (top right quarter only). (**d**) Isometric sketch of domain with collar added. (**e**) 2D slice of rasterised domain with collar (top right quarter only).

many homogenisation calculations, interpolation of material properties also provides sensitivity (derivative) information for the macroscopic structure optimisation.

4.2.2 Problem Domain

We examine a simplified domain for the femoral implant problem, which is a 3D version of that used by Kuiper and Huiskes (1997). While more complicated and realistic domains have been considered (e.g. Chanda et al., 2015b) the idealised domain used here allows us to do an extensive theoretical study and draw useful conclusions regarding the application of the MIMO method and the microstructures used. The idealised 3D domain is shown in Fig. 4.3a and 4.3b. It consists of two coaxial cylinders. The outer hollow cylinder contains the existing bone (Ω_B) and extends from the distal end (z_1) where a fixed boundary condition holds the bone in

place. The inner cylinder is the prosthetic (Ω_P) extending from the proximal end (z_4) where a torque boundary condition provides the elastic load. Where the cylinders cross over is the bone-prosthetic interface ($[z_2, z_3]$) with the interface surface Π defined as the surface between Ω_B and Ω_P. The bone material is modelled as isotropic with a Young's modulus of 20 GPa and Poisson's ratio of 0.3.

We note that the mesh used for describing the prosthetic is an implicit constraint and can impact the optimisation in subtle ways (Bendsøe and Sigmund, 2003). To reduce non-homogeneous influences to the optimisation by the mesh a regular hexahedral mesh is used to describe the prosthetic design and solve the linear elastic problem. The mesh containing the whole domain has $128 \times 128 \times 512$ hexahedral elements. The volumes Ω_B (the existing bone) and Ω_P (the prosthetic) need to be rasterised so as to fit this. Fig. 4.3c shows a top view of the ideal domain rasterised into voxels — note that the surface Π is partially inside Ω_B and partially inside Ω_P.

The surface Π being contained in elements of both material types is problematic: the calculated stress on Π is quite irregular, causing rasterisation artefacts in the evaluation the optimisation objective. To mitigate this issue, we modify the problem domain slightly to that of Fig. 4.3d, by adding a collar (Ω_C) to the interface between the prosthetic and the bone. This allows the surface Π to exist entirely in the same material and smooths out the integrand on Π relevant for calculation of the objective function. The material properties inside Ω_C are set to be the same as the existing bone.

The total number of finite elements describing the bone prosthetic (Ω_P), and thus the total number of design variables in the optimisation, was 2,001,384. Ω_P was 361 elements high and 84 elements wide. The microstructure unit cell length-scale does not affect the calculated homogenised material properties so long as the unit cell length-scale is small in comparison to the macroscopic length-scale. As such, the number of microstructure unit cells used to manifest the design is unspecified in the optimisation problem.

4.2.3 Shear stress objective

The objective function to be minimised is (Kuiper and Huiskes, 1997)

$$F = \int_\Pi (\tau_i \tau_i)^m \, dS = \int_\Pi \tau^{2m} \, dS \tag{4.1}$$

where $\boldsymbol{\tau}$ is the shear stress vector with norm τ and Π is the cylinder with radius r_1 ranging over $z \in [z_2, z_3]$ between the existing bone and prosthetic (shown in Fig. 4.3). Conceptually, the objective should reduce shear stress concentrations on the bone-prosthetic interface by

penalising high values via the exponent $2m$. The objective integral is similar to a p-norm without the final renormalisation exponent. As $p \to \infty$ the p norm becomes the max norm. As m is raised it is therefore expected that the optimisation will distribute the shear stress more evenly throughout the interface.

There will be stress singularities at corners such as at the top of the interface surface Π (Williams, 1952). For F to be well-defined m must be small enough such that the singular integrand is still integrable. If m is too large then we may still calculate a value numerically, however the value of the integral may not converge but instead be mesh dependent. For the same reasons we do not consider the maximum value of the shear stress as it will be infinite. Here we consider $m = 1$ and $m = 2$.

4.2.4 Resorption constraint

Bone resorption (where underloaded bone is absorbed by the body) is also quantified in a similar manner to Kuiper and Huiskes (1997) as

$$m_{\mathrm{r}} = \frac{1}{|\Omega_{\mathrm{B}}|} \int_{\Omega_{\mathrm{B}}} H((1-s)U_{\mathrm{ref}} - U)\rho \, d\boldsymbol{x} \tag{4.2}$$

where H is the Heaviside step function, U is the strain energy, U_{ref} is a reference energy and s a dead zone parameter. Similar to Kuiper and Huiskes (1997) $s = 0.5$ is used. U_{ref} is calculated as the value of strain energy when the bone is continued to the top of the domain and the prosthetic is removed. Describing this constraint in words, if the strain energy of the bone in the presence of the implant decreases too far below U_{ref} it is considered resorped.

For the Heaviside step function we use the approximation

$$H(x) \approx \tilde{H}(x) = \frac{1}{2} + \frac{1}{2}\tanh(ax), \tag{4.3}$$

where $a = 10$ is a parameter for the “sharpness". This smoothed $\tilde{H}$ provides sensitivity information for the constraint to the optimiser. Using $\tilde{H}$ the constraint function becomes

$$m_{\mathrm{r}} = \frac{1}{2|\Omega_{\mathrm{B}}|} \int_{\Omega_{\mathrm{B}}} \left(\tanh\left[a \left((1-s) - \frac{U}{U_{\mathrm{ref}}} \right) \right] + 1 \right) d\boldsymbol{x}. \tag{4.4}$$

Note we divide the argument of the Heaviside function by the reference stress to make it dimensionless, ensuring consistent smoothing over various values of U_{ref}.

In addition to the above approximation we would like to avoid discretisation artefacts. We further modify the above to

$$m_{\mathrm{r}} = \frac{1}{|\Omega_{\mathrm{B}}^{\mathrm{R}}|} \sum_{e \in \Omega_{\mathrm{B}}^{\mathrm{R}}} \frac{1}{2} \tanh \left[a \left((1-s) - \frac{\int_e U \, d\boldsymbol{x}}{\int_e U_{\mathrm{ref}} \, d\boldsymbol{x}} \right) \right] + \frac{1}{2}, \tag{4.5}$$

where $\Omega_{\mathrm{B}}^{\mathrm{R}}$ is the set of all elements associated with the bone in the rasterised domain. That is, we consider the average strain energy within elements when calculating the amount of bone resorped.

4.2.5 Numerical and optimisation details

The optimisation problem, formally, is

$$\begin{aligned} &\min_{\rho(\boldsymbol{x})} F(\rho(\boldsymbol{x}), \boldsymbol{u}) \\ &\text{subject to } \begin{cases} \boldsymbol{u} = \underset{\boldsymbol{u}'}{\operatorname{argmin}} \dfrac{1}{2} \displaystyle\int_\Omega \varepsilon_{ij}(\boldsymbol{u}') C_{ijkl}(\rho) \varepsilon_{kl}(\boldsymbol{u}') \, dV \\ \qquad\qquad\qquad - \displaystyle\int_{\partial\Omega} u_i' t_i \, dS \\ m_{\mathrm{r}}(\boldsymbol{u}) \leq 0.05, \end{cases} \end{aligned} \tag{4.6}$$

where C_{ijkl} is the effective stiffness tensor for the relevant microstructure or the stiffness tensor for bone, as appropriate; ε is the strain tensor; and $\boldsymbol{t}$ is the boundary traction. As discussed in Chapter 2, the linear elastic problem is solved on a regular hexahedral grid with displacements piece-wise linear in each axial direction.

Prosthesis designs consist of a description of what microstructure to use throughout Ω_{P} specified by the microstructure volume fraction $\rho(\boldsymbol{x})$. The bone prosthesis is optimised in two ways for each microstructure set. The first is a homogeneous, constant volume fraction design — that is, the microstructure volume fraction is the same everywhere throughout the design ($\rho(\boldsymbol{x}) = \rho_{\mathrm{opt}}$). The second is inhomogeneous, allowing the microstructure volume fraction to vary spatially, constant within each finite element. This is as per the homogenisation method of structural optimisation (Bendsøe and Kikuchi, 1988). The densities are restricted to be in the interval $[0.1, 0.9]$. With $\rho < 0.1$, microstructures feature many small members that are difficult to represent faithfully while a microstructure with $\rho > 0.9$ would have small pore channels, also leading to manufacturing issues.

For the homogeneous designs the bisection method is used on the constraint function. Kuiper and Huiskes (1997) showed that the constraint and the objective are competing functions in the

TABLE 4.2: Objective and constraint results for $m = 1$. The inhomogeneous designs have objectives reduced by a factor of at least 2.4 compared to the corresponding homogeneous designs.

		$E^0 = 60$ GPa Material			$E^0 = 100$ GPa Material		
Microstructures	Design	$\langle\rho\rangle$	$\int_\Pi \tau^2 dS$	m_r	$\langle\rho\rangle$	$\int_\Pi \tau^2 dS$	m_r
A, iso, bulk opt.	homog.	0.54	2.41×10^7	5.00%	0.40	2.42×10^7	4.98%
	inhom.	0.44	9.95×10^6	4.99%	0.40	9.96×10^6	4.99%
B, cross	homog.	0.34	2.74×10^7	5.00%	0.14	3.74×10^7	5.00%
	inhom.	0.41	7.34×10^6	5.01%	0.34	7.14×10^6	5.07%
C, bulk opt.	homog.	0.36	2.57×10^7	5.00%	0.17	3.10×10^7	5.00%
	inhom.	0.41	8.46×10^6	5.02%	0.34	8.40×10^6	5.00%
D, rotated C	homog.	0.57	2.46×10^7	5.02%	0.46	2.50×10^7	4.97%
	inhom.	0.44	9.84×10^6	4.99%	0.41	1.04×10^7	4.99%

TABLE 4.3: Objective and constraint results for $m = 2$. The inhomogeneous designs have objective values at least an order of magnitude better than the homogeneous ones.

		$E^0 = 60$ GPa Material			$E^0 = 100$ GPa Material		
Microstructures	Design	$\langle\rho\rangle$	$\int_\Pi \tau^4 dS$	m_r	$\langle\rho\rangle$	$\int_\Pi \tau^4 dS$	m_r
A, iso, bulk opt.	homog.	0.54	8.00×10^{18}	5.00%	0.40	8.04×10^{18}	4.98%
	inhom.	0.43	1.57×10^{17}	5.01%	0.38	1.60×10^{17}	5.00%
B, cross	homog.	0.34	1.56×10^{19}	5.00%	0.14	5.83×10^{19}	5.00%
	inhom.	0.39	1.80×10^{15}	5.02%	0.34	3.90×10^{15}	5.03%
C, bulk opt.	homog.	0.36	1.17×10^{19}	5.00%	0.17	2.66×10^{19}	5.00%
	inhom.	0.38	6.22×10^{15}	5.01%	0.32	8.47×10^{15}	5.01%
D, rotated C	homog.	0.57	8.92×10^{18}	5.02%	0.46	9.34×10^{18}	4.97%
	inhom.	0.46	3.97×10^{16}	5.02%	0.38	5.03×10^{16}	5.01%

sense that a softer prosthetic will lead to a larger concentration of stress with low resorption while a stiff prosthetic will have a lower concentration of stress and higher resorption due to stress shielding. Therefore the volume fraction ρ where the constraint is active is the optimal volume fraction for the homogeneous case. The optimiser used for the inhomogeneous designs is the Globally Convergent Method of Moving Asymptotes (GCMMA) (Svanberg, 1987, 2002). As there are no simultaneous elastic homogenisation calculations to perform — elastic properties of the microstructure sets have already been determined — the macroscopic optimisation is very computationally efficient.

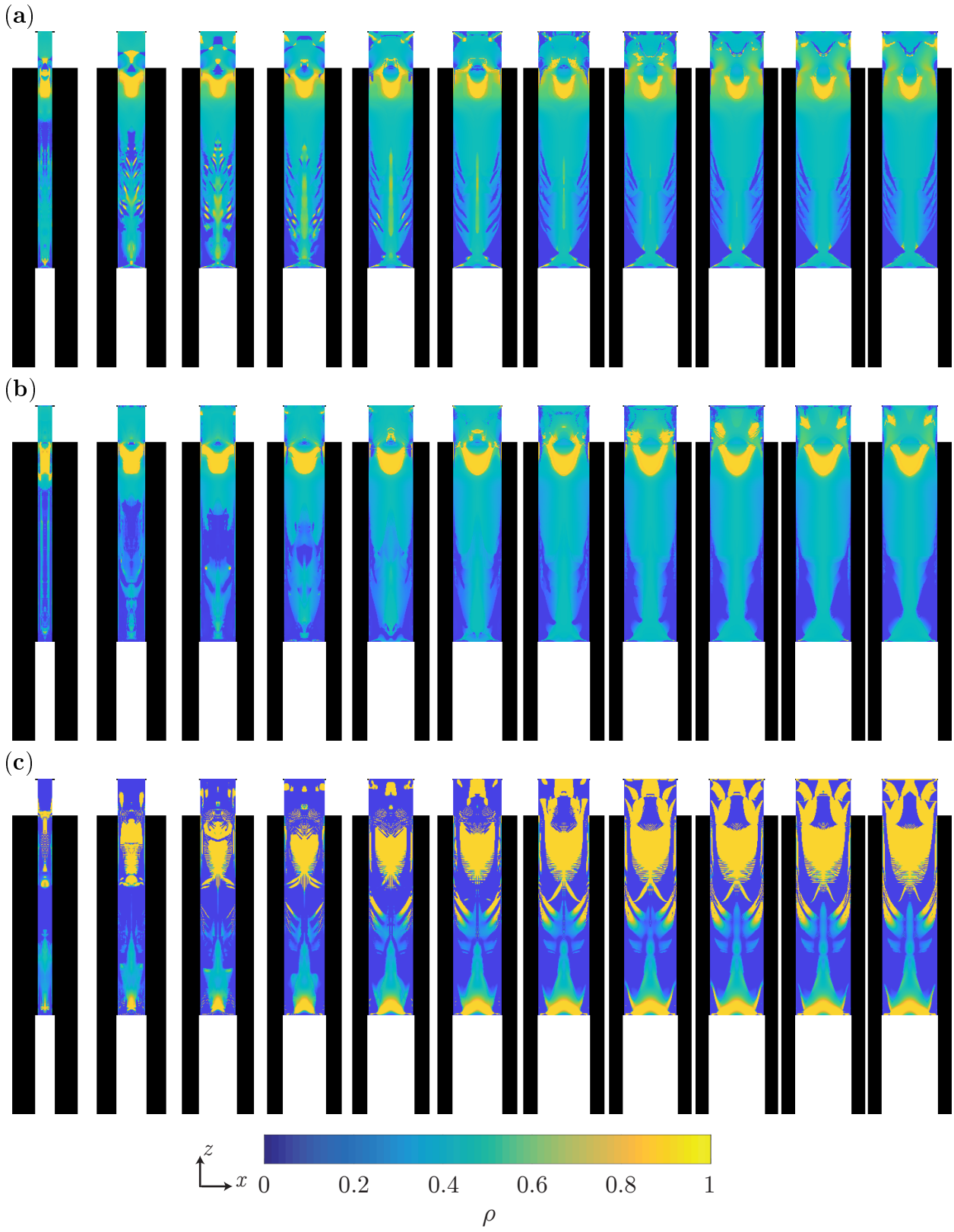

FIGURE 4.4: Prosthetic designs displaying volume fraction, ρ. Slices taken from the back of the prosthesis to the front with the torque forcing clockwise in the page (i.e. torque axis is out of page). All designs shown have a base material with Young's modulus 60 GPa. Black is bone, white is void. (**a**) $m = 1$, microstructure set A. (**b**) $m = 1$, microstructure set C. (**c**) $m = 2$, microstructure set C. Note the filament-like structures with microstructure set A and with microstructure set C when $m = 2$.

4.3 Results and Discussion

Objective function results can be seen in Table 4.2 and Table 4.3, while some optimised volume fraction distributions are shown in Fig. 4.4. Convergence histories are also shown in Fig. 4.5. First we note that the inhomogeneous (ρ varying) designs perform better than the homogeneous designs (ρ constant), especially with $m = 2$. The smallest improvement factor between the homogeneous and inhomogeneous designs is 2.4. Further, for the same value of m all inhomogeneous designs are better than all homogeneous. This clearly demonstrates that spatially varying the material properties is beneficial and, for the microstructures considered, provides more improvement in the shear stress objective than choosing the best single microstructure to be used throughout the domain.

Note that the units are changed as m changes and so comparisons cannot easily be drawn between the objective values for different m values. When $m = 1$ the designs tended to be smoother, with volume fraction changes happening over longer length scales than when $m = 2$. In addition, the optimisations required more iterations for convergence for $m = 2$ (Fig. 4.5). The average density $\langle\rho\rangle$ for the inhomogeneous designs varies from 0.32 to 0.46. This variation of the amount of material used is much less than for the homogeneous designs, for which the average density varies from 0.14 to 0.57.

With $m = 2$, the inhomogeneous designs make use of thin filaments of high volume fraction (e.g. Fig. 4.4c) suggesting that the microstructures should be able to vary their stiffness in differing directions independently. This is examined further in Chapter 5.

The inhomogeneous designs using microstructure set D have worse objective values than those using set C, showing that the orientation of the microstructures is an important factor. The narrow diagonal bands in the designs with microstructure set A suggest that the prosthetic should be compliant along the diagonal leading inward and up from the interface while stiff perpendicular to this (Fig. 4.4a). Microstructure set D is stiff in both these directions, perhaps leading to the poorer objective values and some similar banding which is visible in the optimised designs using this microstructure set. Interestingly, while sets B and C perform better with the inhomogeneous designs, sets A and D perform better with the homogeneous ones.

Typically the base material stiffness had a small effect on the objective values for the inhomogeneous designs (ρ spatially varying) except for the microstructure set B, $m = 2$ case. In this case the base material with a Young's modulus of 60 GPa far outperforms the 100 GPa base material by around 2 times. For the homogeneous designs (ρ constant), the base material with a Young's modulus of 60 GPa consistently outperforms the 100 GPa base material case, and some large differences can be seen. This preference for the 60 GPa base material is expected,

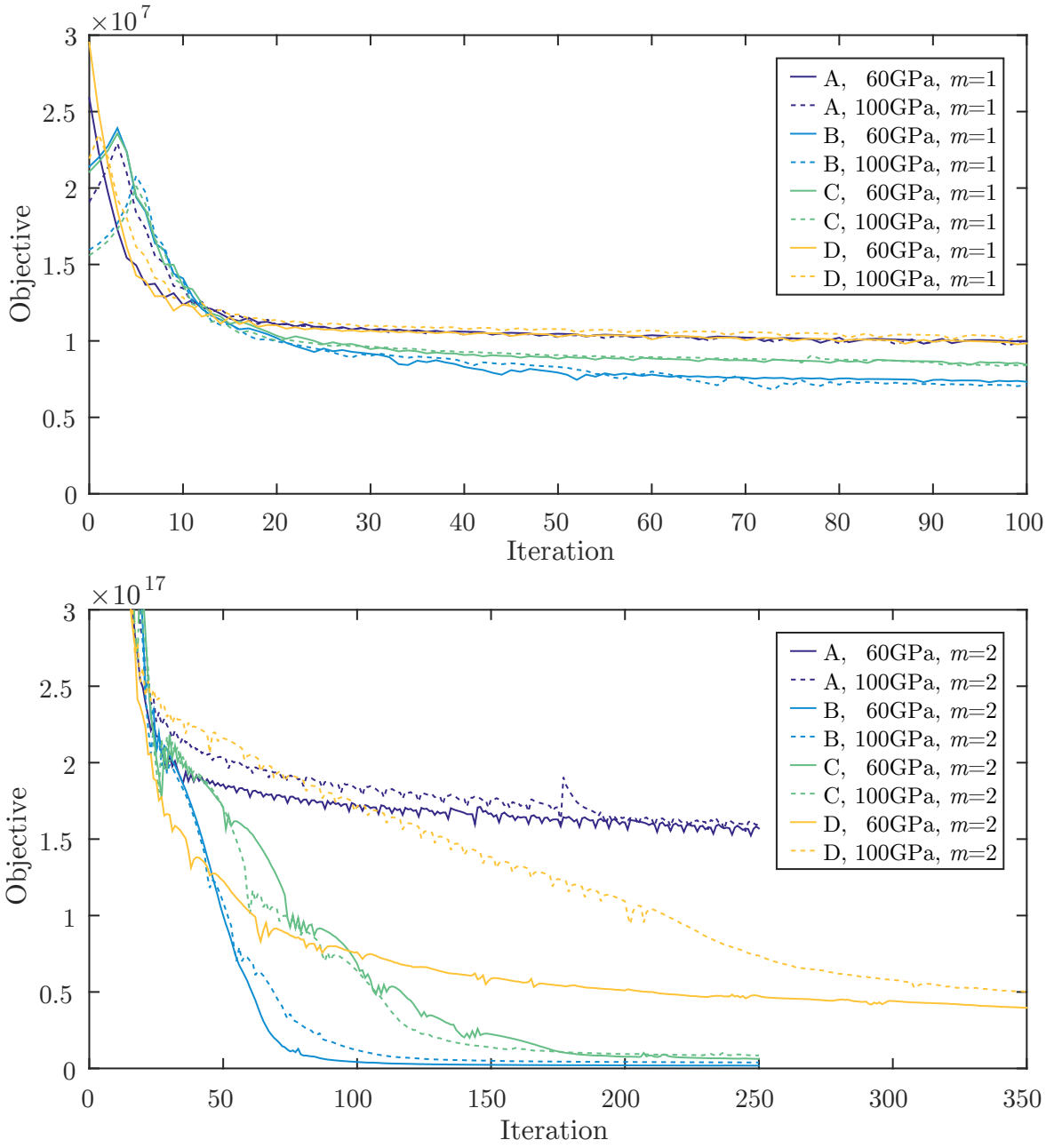

FIGURE 4.5: Optimisation history for macroscopic optimisations. The initial increase shown with $m = 1$ is due to first matching the resorption constraint.

as 60 GPa is closer to the stiffness of the bone (modelled as 20 GPa) than 100 GPa. Further, in all cases making the base material stiffer results in a lower average volume fraction ($\langle\rho\rangle$), as expected.

Shear stress is distributed unevenly across the interface with the majority concentrated near the proximal end (Fig. 4.6). At the proximal end where stress singularities are expected the inhomogeneous designs have low density just above the interface, in effect straightening the corner out (Fig. 4.4). The effect is noticeable in the shear stress (Fig. 4.6 and Fig. 4.7): the homogeneous design clearly has a shear stress that is trending towards infinity while the inhomogeneous designs may not have a stress singularity at all. Comparing the stress distributions between the $m = 1$ and $m = 2$ cases, one can see that for $m = 2$ the shear stress distribution is flattened out as expected (Fig. 4.7). Also shown is the stress distribution for a single $m = 3$ optimisation which is similar to the shear stress distribution with $m = 2$. This shows diminishing marginal benefit to raising m. Further optimisations were not performed for $m \geq 3$ as the optimisation cost increased with m, for $m = 3$, 750 iterations were required compared to around 250 for $m = 2$ and 100 for $m = 1$.

While the cross microstructure set (set B) performs the best, the hard angles make the designs difficult to manufacture. Therefore a design using microstructure set C was chosen and a model was produced using SLM (Fig. 4.8 and 4.9) (Challis et al., 2014b). With the SLM resolution currently available to the author, only base cells on the scale of 3mm could be produced. With improvements in SLM technology we expect this cell size to be reduced to provide microstructural pores on a scale suitable for bone in-growth (visualised in Fig. 4.8b) (Camron et al., 1976; Boyan et al., 1996). Even at this coarse scale the production of such a prototype demonstrates that such a multiscale design is manufacturable and will become a feasible solution to the bone prosthesis problem.

The microstructures used for a bone prosthesis should also take into account biological and practical business considerations beyond just the choice of length-scale suitable for bone ingrowth (Hollister and Murphy, 2011). While work is continuing in this direction, notably experiments examining bone ingrowth and strength of truss microstructures (Arabnejad Khanoki et al., 2016b), there is still work to be done towards finding the overall best microstructure.

4.4 Conclusion

We have designed porous femoral implants on a simplified 3D domain to minimise the shear stress over the bone-prosthetic interface while constraining the bone resorption. Implants have been designed with four different sets of microstructures. Interpolation between optimised

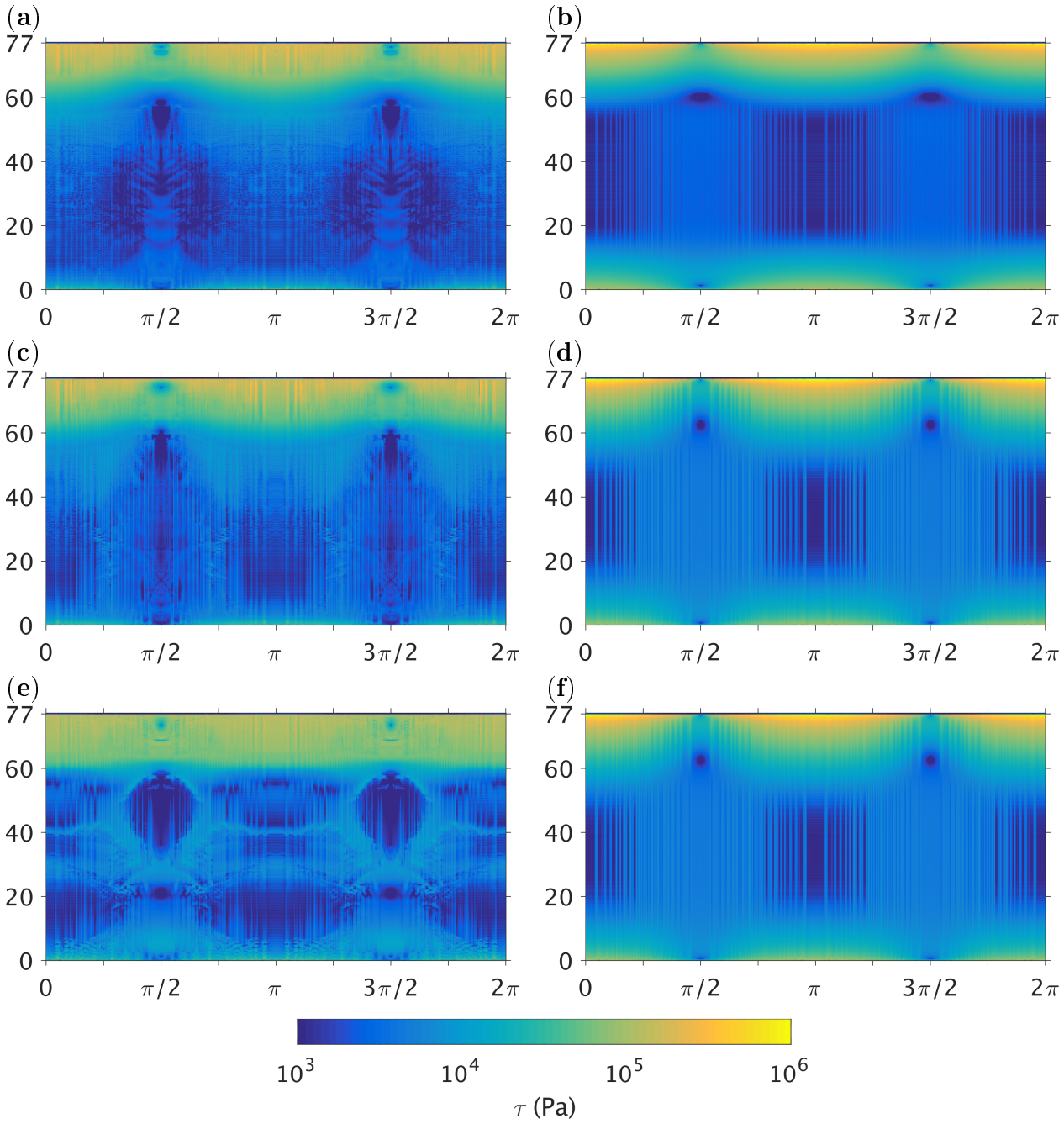

FIGURE 4.6: Stress distributions across the interface Π for: $m = 1$, microstructure set A (**a**) homogeneous and (**b**) inhomogeneous; $m = 1$, microstructure set C (**c**) homogeneous and (**d**) inhomogeneous; $m = 2$, microstructure set C (**e**) homogeneous and (**f**) inhomogeneous. An angle of 0 corresponds to the part of Π where $y = 0$, $x > 0$. Stress values have been truncated to the range $[10^3, 10^6]$ however some extreme values are outside this. Vertical striations are an artefact of the discretisation. Note the reduction in shear stress concentrated at the proximal end (top) for the homogeneous (b,d,f) compared to the inhomogeneous (a,c,e) and the further reduction from the $m = 1$ case (c) to the $m = 2$ case (e).

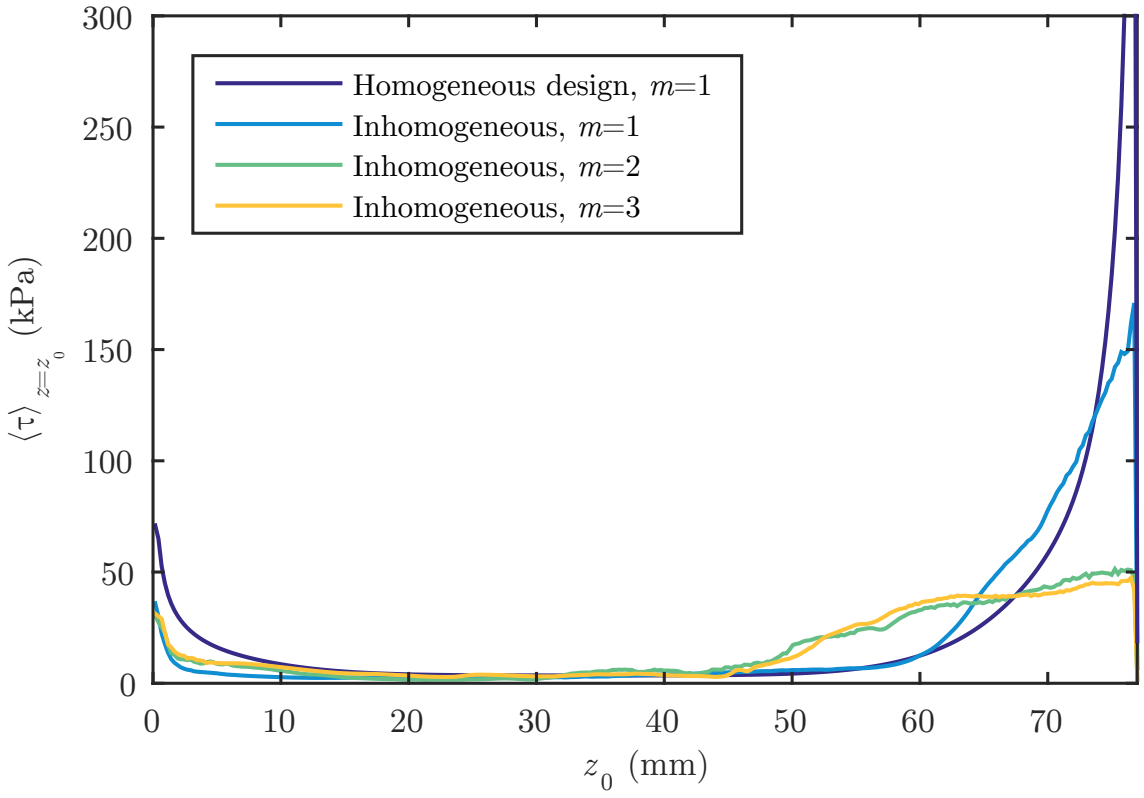

FIGURE 4.7: Shear stress averaged on circles around the interface surface Π. Microstructure set C with a 60 GPa base material. As m increases the maximum of the shear stress decreases and the distribution becomes flatter.

microstructures was used to generate microstructure sets that smoothly vary in geometry and elastic properties. Structural optimisation on the macroscopic scale was then used to design spatially homogeneous implants with the same microstructure throughout (ρ constant) as well as spatially inhomogeneous implants where the microstructure varies (ρ varying).

There are several benefits to the presented approach. The inhomogeneous designs outperform the homogeneous designs: significantly reduced objective values are obtained when spatial variation of the microstructures is allowed. Furthermore, the two-scale optimisation method is computationally efficient: after the establishment of the microstructure set no homogenisation calculations are required. There is also fine grain control over the microstructure set used: the topology of the microstructures used can supervised without automation required to chose candidates, yet the microstructures can be taken from sets without closed form descriptions such as the bulk modulus optimised microstructures seen here. Finally, the resulting designs are physically realisable, being composed of varying microstructures that are guaranteed to transition smoothly and with a connected pore space that will allow the removal of excess material after fabrication with selective laser melting (SLM). This was demonstrated via construction

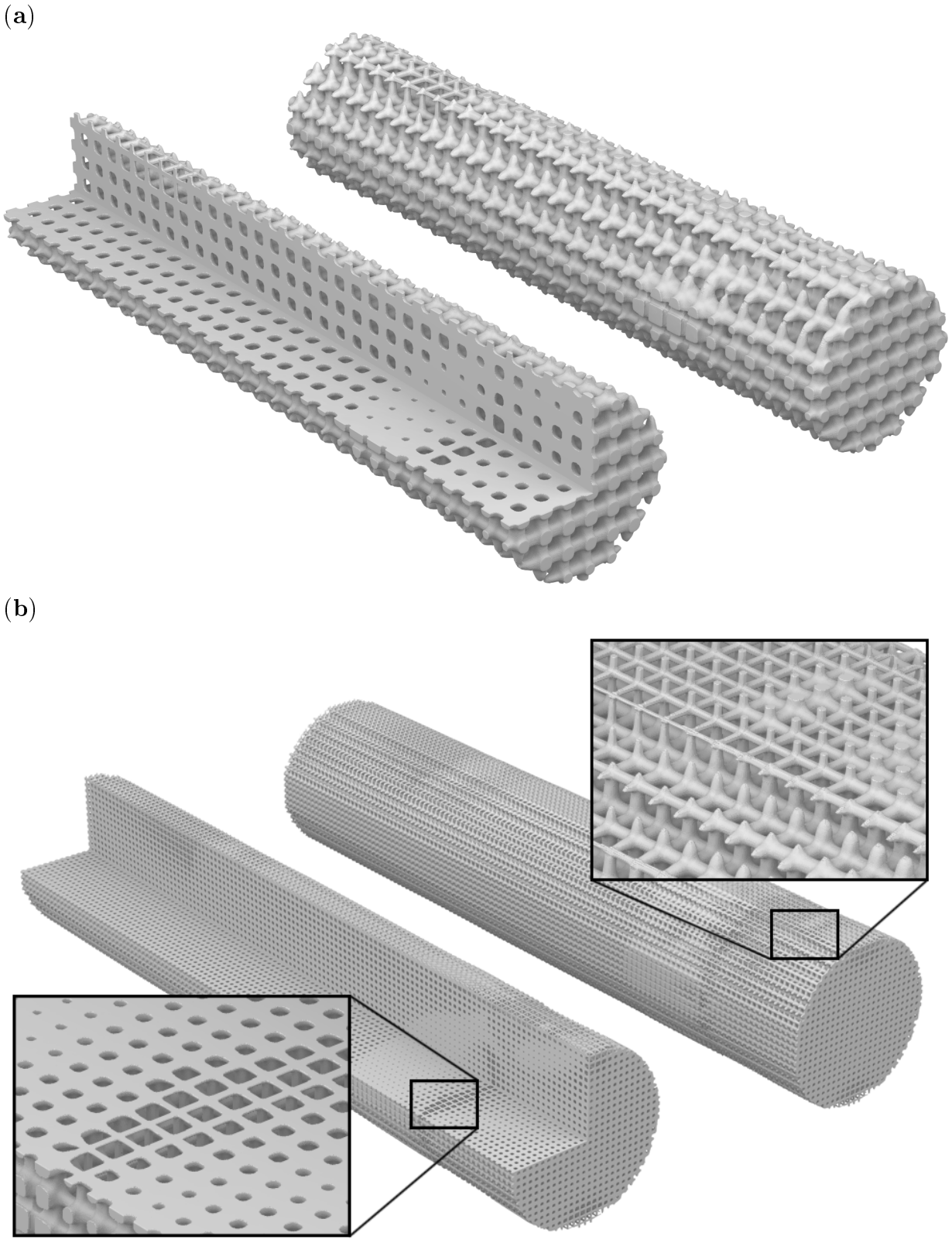

FIGURE 4.8: (**a**) Two renders of a potential design with microstructure cells 2.86mm across, the left has one quadrant removed to show internal structure, the right is unmodified. (**b**) Two renders of a design similar to (a) with microstructure cells that are 800μm across, giving pores at a scale relevant for bone ingrowth.

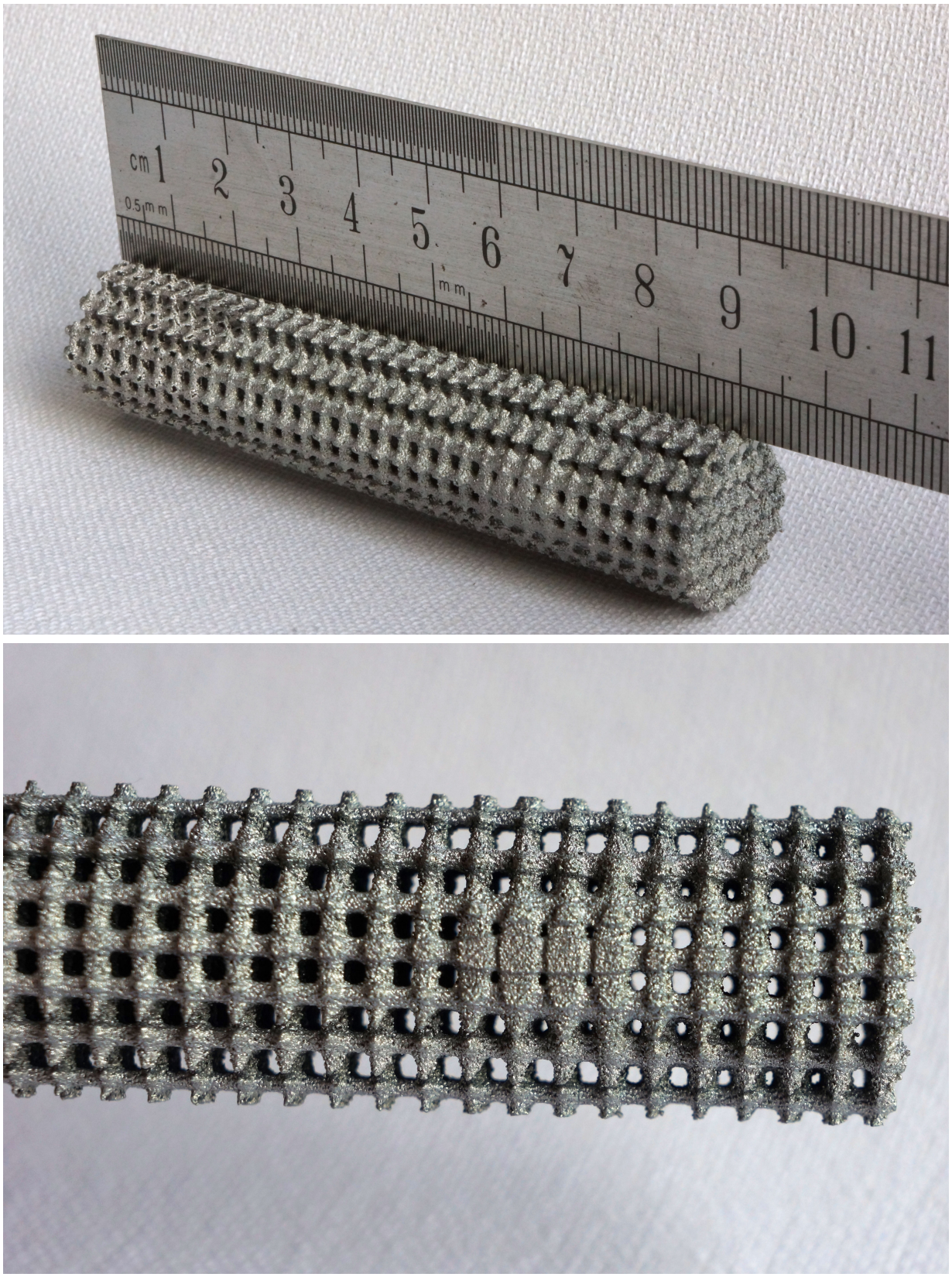

FIGURE 4.9: Photographs of the design in Fig. 4.8a, manufactured using selective laser melting (SLM). We thank Tim Sercombe (The University of Western Australia) for the manufacture of the prototype and Chris Foster for the photography.

of a physical prototype.

The choice of microstructure set was found to be important for the femoral implant problem. When the isotropic microstructures are used the existence of small macroscopic structures in the implant designs suggest that anisotropic microstructures should be used. Indeed, the anisotropic microstructures produced designs with better objective values than the designs with isotropic microstructures and the small scale features are no longer present. The choice of microstructure orientation was also shown to be an important factor. Ideally the orientation of the stiffest direction of the microstructure should be allowed to vary throughout the design, however this causes connectivity issues that are non-trivial to solve. In Chapter 5 we use a multiparametric microstructure set to allow this variation.

The domain and loading conditions considered here are considerably simplified, providing both a proof-of-concept and a way to consider which microstructures are appropriate for the femoral implant problem. In particular, the nuanced structure of the femur is missing, with only uniform, cortical bone present. True femurs also contain porous trabecular tissue which itself varies in density. In addition to the idealised domain, the objective function is missing a component dealing with the strength of the prosthesis. Strength is an important requirement and it should be ensured that a bone prosthetic be able to withstand the rigours of day-to-day use over a long time period (Arabnejad Khanoki and Pasini, 2013). More suitable loading conditions, geometry and non-linear analysis can be seen in the works of Arabnejad Khanoki and Pasini (2013); Chanda et al. (2015b); and Arabnejad Khanoki et al. (2016a) for example, which consider multiple load cases on a more complicated geometry generated from CT data. Combining the use of spatially varying three-dimensional microstructures with a more realistic loading situation and suitable objective functions could provide benefits for the design of femoral implants and other prostheses. Recommendations of more suitable loading conditions, objective functions, and geometries for this prosthesis problem are outside the scope of this thesis however, as is the use of CT data.

The following chapter (Chapter 5) explores the use of more general microstructures for the femoral implant problem; microstructures which are not only anisotropic, but also can have the stiffness in different directions vary independently.

Chapter 5

Multiparametric Microstructure Interpolation

In Chapter 3 we developed the microstructure interpolation for macroscopic optimisation (MIMO) method whereby optimised microstructures interpolated using a single parameter were used for macroscopic optimisation with the material distribution method. While the method did not show significant improvements for compliance problems in three dimensions as it did in two dimensions, in Chapter 4 we showed that it provides benefits for the three-dimensional femoral implant design problem. The choice of microstructure — including orientation — was seen to be significant. In this chapter, we generalise the MIMO method to utilise a microstructure set with a multi-dimensional parameterisation and apply the microstructures to the femoral implant design problem. Having recognised that the optimised structures have strong orientational preferences we would like to use a microstructure family that can exploit this.

5.1 Introduction

The microstructure set developed in this chapter varies in multiple effective properties independently, is optimised, single scale, and remains smoothly varying to facilitate connectivity between microstructures. To our knowledge no such single scale, multiparametric microstructure set has been optimised previously. Bendsøe and Kikuchi (1988) used a rectangular lattice, however the lattice was not optimised but described analytically. Similarly Jog et al. (1994) used analytical descriptions of microstructures built from ranked laminates. While Rodrigues et al. (2002) and Coelho et al. (2008) use microstructures that are fully general with no additional limit to their effective properties past what is physically possible, they are not guaranteed to vary in a continuous manner.

In this chapter we explore a space of microstructures parameterised by their effective Young's moduli along the three axial directions. Finding a family of microstructures that fulfils these requirements while maintaining features similar enough for interpolation is complex; a number of difficulties arise when the dimensionality of the parameterisation is greater than one. With the higher dimensionality the number of key-microstructures is much larger. If 10 different key microstructures are desired along every parameter dimension then the number of key microstructures is 1000. While 10 can be hand picked and examined individually, the generation of 1000 key microstructures must be automated in some way. In addition, the space of valid microstructures will cease to be an interval ($[\rho_{\min}, \rho_{\max}]$) and may be a general shape other than a hypercube. As such, the limits of one parameter depend on the value of the other parameters and may not be described analytically. We explore a penalisation function to incorporate such a constraint into the macroscopic optimisation.

The remainder of this chapter is organised as follows: the microstructure set is prescribed and generated in Section 5.2 before being applied to the bone femoral implant problem in Section 5.3. Results of the optimisation are discussed in Section 5.4 with the application to functionally graded materials in Section 5.5. Finally, Section 5.6 contains concluding remarks for the chapter.

5.2 Microstructures

Here a set of microstructures is generated, parameterised by the axial Young's moduli, E_x, E_y, and E_z. In Chapter 4 we saw evidence that materials with directional dependence may be desirable for use in optimisation. These microstructures should provide benefits over the single parameter microstructures due to the increased freedom in available effective material properties: if load is to be carried in only one direction then that direction can be stiffened independently of the others.

As before, a number of key microstructures will be generated and the full set will be interpolated from these. The family generated should be similar enough such that the homogenised properties are smoothly changing when the microstructural geometry is interpolated via shape interpolation.

5.2.1 Parameterisation

A fully general compliance tensor S_{ijkl} has 21 degrees of freedom. For simplicity we constrain the desired effective stiffness tensors to be orthotropic, meaning that the tensor is unchanged

through axial reflections. This restriction removes the ability for the material to shear in response to axial loads. A general orthotropic compliance tensor has 9 degrees of freedom, explicitly

$$S_{\alpha\beta} = \begin{bmatrix} a & b & c & 0 & 0 & 0 \\ b & d & e & 0 & 0 & 0 \\ c & e & f & 0 & 0 & 0 \\ 0 & 0 & 0 & g & 0 & 0 \\ 0 & 0 & 0 & 0 & h & 0 \\ 0 & 0 & 0 & 0 & 0 & i \end{bmatrix}. \tag{5.1}$$

Applying the axial Young's modulus constraints leaves 6 degrees of freedom:

$$S_{\alpha\beta} = \begin{bmatrix} \frac{1}{E_x} & b & c & 0 & 0 & 0 \\ b & \frac{1}{E_y} & e & 0 & 0 & 0 \\ c & e & \frac{1}{E_z} & 0 & 0 & 0 \\ 0 & 0 & 0 & g & 0 & 0 \\ 0 & 0 & 0 & 0 & h & 0 \\ 0 & 0 & 0 & 0 & 0 & i \end{bmatrix}. \tag{5.2}$$

Clearly then, the elastic tensor is underspecified.

The Young's modulus in the direction of

$$\boldsymbol{n}(\theta) = \begin{bmatrix} \cos\theta \\ \sin\theta \\ 0 \end{bmatrix} \tag{5.3}$$

in the x-y plane for an orthotropic material is

$$E_{\boldsymbol{n}} = \frac{1}{n_i n_j S_{ijkl} n_k n_l} \tag{5.4}$$

$$= \frac{1}{\frac{1}{E_x}\cos^4\theta + 2(S_{xxyy} + 2S_{xyxy})\sin^2\theta\cos^2\theta + \frac{1}{E_y}\sin^4\theta} \tag{5.5}$$

$$= \frac{1}{\frac{1}{E_x}\cos^4\theta + 2\gamma_{xy}\sin^2\theta\cos^2\theta + \frac{1}{E_y}\sin^4\theta}, \tag{5.6}$$

where

$$\gamma_{xy} = S_{xxyy} + 2S_{xyxy}. \tag{5.7}$$

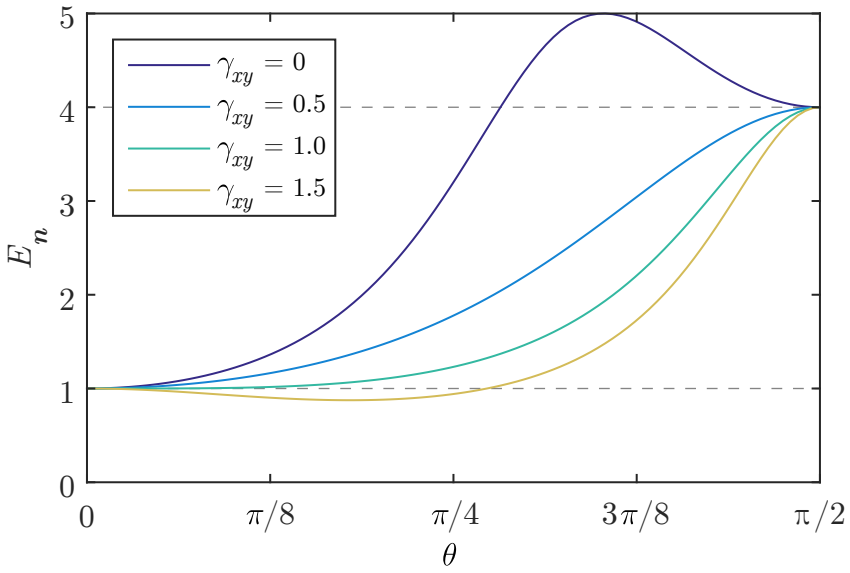

FIGURE 5.1: Directional dependence of Young's modulus in the x-y plane where $E_x = 1$ and $E_y = 4$. Some choices of γ_{xy} will lead to intermediate values lying outside the range $[E_x, E_y]$.

$E_{\boldsymbol{n}}$ is shown for $\theta \in [0, \frac{\pi}{2}]$ and various choices of γ_{xy} in Fig. 5.1. There are three possible strategies for choosing γ_{xy}: letting γ_{xy} be unconstrained, making γ_{xy} another parameter along with the three E_i, and choosing $\gamma_{xy} = \gamma_{xy}(E_x, E_y, E_z)$. If γ_{xy} is allowed to be free then $E_{\boldsymbol{n}}$ may be some extreme value falling outside of $[E_x, E_y]$. While γ_{xy} could become a parameter along with E_x, E_y, and E_z; we restrict ourselves to the original three parameters to keep the number of microstructures directly optimised computationally feasible.

We choose

$$\gamma_{xy} = \frac{S_{1111} + S_{2222}}{2} = \frac{1}{2E_x} + \frac{1}{2E_y} \tag{5.8}$$

which leads to

$$E_{\boldsymbol{n}} = \frac{1}{\frac{1}{E_x}\cos^2\theta + \frac{1}{E_y}\sin^2\theta}. \tag{5.9}$$

This choice ensures isotropy in the case of $E_x = E_y$ and ensures that $E_{\boldsymbol{n}}$ is monotonic between the axes. The corresponding choice is made for γ_{xz} and γ_{yz} to obtain the compliance tensor[1]

$$S_{\alpha\beta} = \begin{bmatrix} \frac{1}{E_x} & b & c & 0 & 0 & 0 \\ b & \frac{1}{E_y} & e & 0 & 0 & 0 \\ c & e & \frac{1}{E_z} & 0 & 0 & 0 \\ 0 & 0 & 0 & \frac{1}{E_y} + \frac{1}{E_z} - 2e & 0 & 0 \\ 0 & 0 & 0 & 0 & \frac{1}{E_x} + \frac{1}{E_z} - 2c & 0 \\ 0 & 0 & 0 & 0 & 0 & \frac{1}{E_x} + \frac{1}{E_y} - 2b \end{bmatrix}. \tag{5.10}$$

If we now let

$$\boldsymbol{n}(\theta) = \begin{bmatrix} \cos\theta\cos\phi \\ \sin\theta\cos\phi \\ \sin\phi \end{bmatrix}, \tag{5.11}$$

the Young's modulus in any direction becomes

$$E_{\boldsymbol{n}} = \frac{1}{\frac{1}{E_z}\sin^2\phi + \frac{1}{E_x}\cos^2\theta\cos^2\phi + \frac{1}{E_y}\sin^2\theta\cos^2\phi}. \tag{5.12}$$

The Young's modulus varies smoothly and monotonically between the axes. This is shown for an example in Fig. 5.2.

Three degrees of freedom remain in the specification of the desired effective stiffness tensors, the Poisson's ratios. We have that

$$b = -\frac{\nu_{yx}}{E_y} = -\frac{\nu_{xy}}{E_x}, \tag{5.13}$$

$$c = -\frac{\nu_{zx}}{E_z} = -\frac{\nu_{xz}}{E_x}, \tag{5.14}$$

$$e = -\frac{\nu_{zy}}{E_z} = -\frac{\nu_{yz}}{E_y}. \tag{5.15}$$

The same three possible choices are available for the Poisson's ratios as for γ_{ij}: leaving them unconstrained, using them as a parameter or specifying them as a function of the parameters. The Poisson's ratios are intimately linked to the geometry of a microstructure, and specifying them may lead to changes in the geometry making the interpolation difficult. Therefore in the interest of allowing the geometry to remain consistent between the microstructures we do not constrain the Poisson's ratios.

[1]Note that using Voigt's notation, the compliance tensor has $S_{44} = 4S_{yzyz}$. This is unlike the stiffness tensor where $C_{44} = C_{yzyz}$.

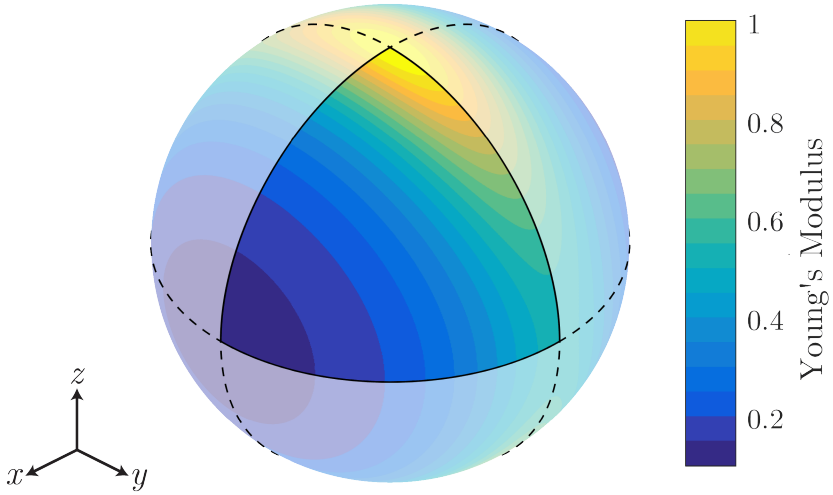

FIGURE 5.2: Three-dimensional Young's modulus directional dependence with $E_x = \frac{1}{8}$, $E_y = \frac{1}{2}$, and $E_z = 1$ with γ_{ij} set as in (5.8). Each point on the sphere is coloured based on the Young's modulus of the tensor in the direction from the centre of the sphere through that point. The colour-map applies only to the front octant that has been emphasised. Note that the Young's modulus on any transect of the octant is monotonic.

In Voigt's notation, the desired effective compliance tensor is

$$S_{\alpha\beta} = \begin{bmatrix} \frac{1}{E_x} & -\frac{\nu_{yx}}{E_y} & -\frac{\nu_{zx}}{E_z} & 0 & 0 & 0 \\ -\frac{\nu_{xy}}{E_x} & \frac{1}{E_y} & -\frac{\nu_{zy}}{E_z} & 0 & 0 & 0 \\ -\frac{\nu_{xz}}{E_x} & -\frac{\nu_{yz}}{E_y} & \frac{1}{E_z} & 0 & 0 & 0 \\ 0 & 0 & 0 & \frac{1}{E_y} + \frac{1}{E_z} + \frac{2\nu_{yz}}{E_y} & 0 & 0 \\ 0 & 0 & 0 & 0 & \frac{1}{E_x} + \frac{1}{E_z} + \frac{2\nu_{xz}}{E_x} & 0 \\ 0 & 0 & 0 & 0 & 0 & \frac{1}{E_x} + \frac{1}{E_y} + \frac{2\nu_{xy}}{E_x} \end{bmatrix}. \tag{5.16}$$

5.2.2 Generation of key microstructures

The key microstructures matching the above properties are found in a similar way to those in previous chapters with the level-set method. Representative cells were 64^3 elements in size. The Young's moduli are constrained along with the γ_{ij} as in (5.8) while the conductivity of the void phase is maximised. Maximising the void conductivity serves two purposes: it helps to ensure the connectivity of the pore space, important for manufacture; and it also reduces the solid volume fraction as a larger pore space will increase the overall void phase conductivity.

Shape sensitivities (recall Section 2.4) for the effective stiffness tensor components, $C^*_{\alpha\beta}$, can be found in Challis (2009) and shape sensitivities for the constraints can be found through the chain and product rules. As $C_{\alpha\beta}$ and $S_{\alpha\beta}$ are inverses, $C_{\alpha\gamma}S_{\gamma\beta} = \delta_{\alpha\beta} = \textit{constant}$. So if $v_{C^*_{\alpha\beta}}$ is

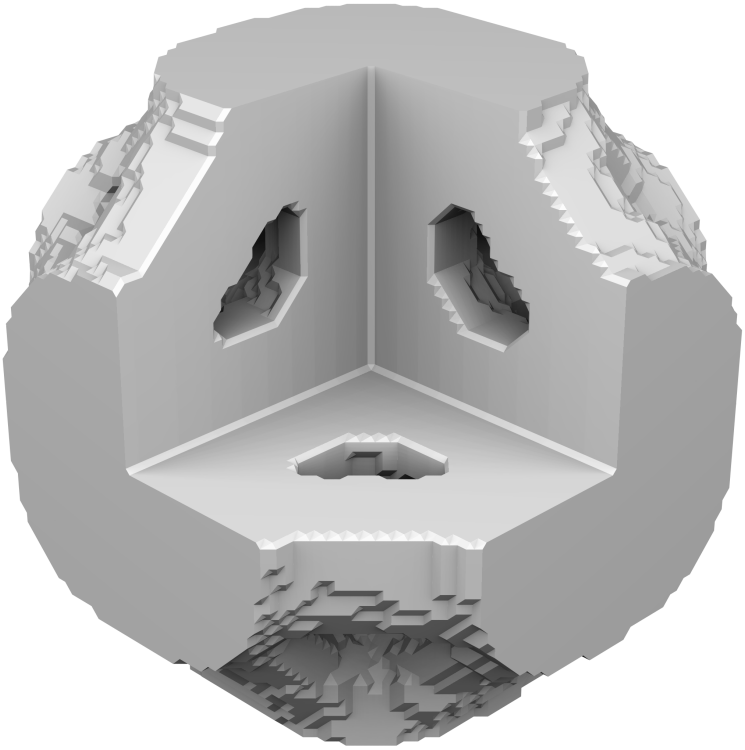

FIGURE 5.3: Initial microstructure for the key microstructure optimisations. The front octant has been removed to show internal structure. The microstructure has $E_x = E_y = E_z = 0.25E^0$ and a surface genus of 12 (without periodic continuations).

the shape sensitivity of $C^*_{\alpha\beta}$ then the shape sensitivity of $S^*_{\alpha\beta}$ is

$$v_{S^*_{\alpha\beta}} = -S^*_{\alpha\gamma} v_{C^*_{\gamma\delta}} S^*_{\delta\beta}. \tag{5.17}$$

Thus the shape sensitivity of $E_x = \frac{1}{S^*_{11}}$ can be found as

$$v_{E_x} = -\frac{v_{S^*_{11}}}{{S^*_{11}}^2}. \tag{5.18}$$

Shape sensitivities for γ_{ij} can be found in a similar way.

Let the set of desired Young's modulus ratios for the key microstructures be

$$\mathcal{E}^{\text{key}} = \{0.01, 0.03, 0.05, 0.07\} \cup \{0.1, 0.15, 0.20, \ldots, 0.9\}. \tag{5.19}$$

The parameter space for the key microstructures is then chosen to be the cube

$$\left(\frac{E_x}{E^0}, \frac{E_y}{E^0}, \frac{E_z}{E^0}\right) \in \mathcal{E}^{\text{key}} \times \mathcal{E}^{\text{key}} \times \mathcal{E}^{\text{key}} \tag{5.20}$$

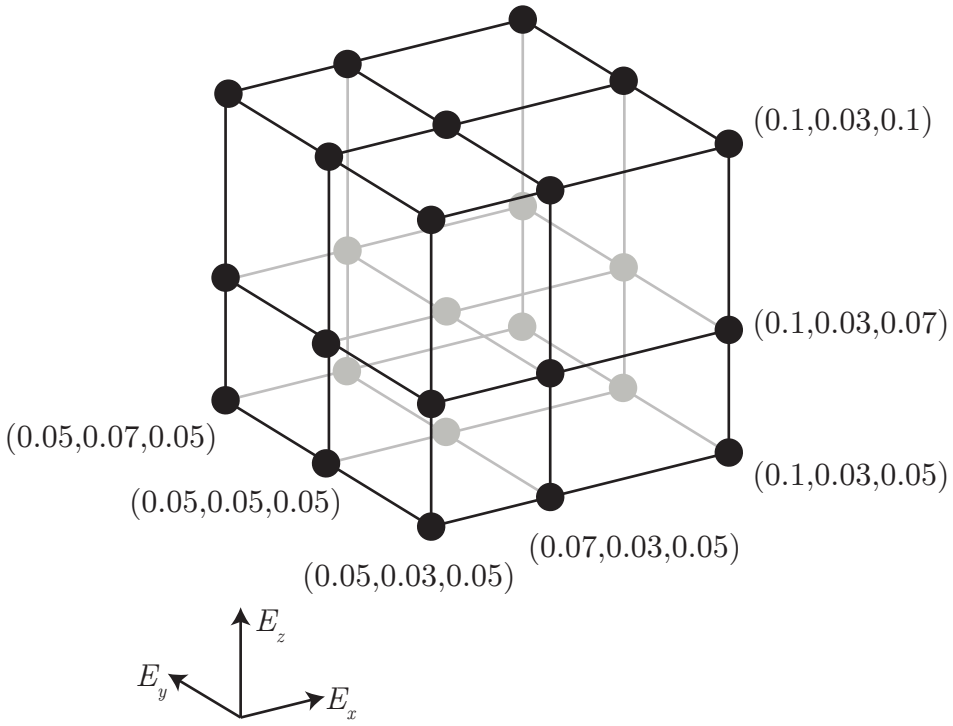

FIGURE 5.4: Key microstructures were considered neighbours if adjacent in the regular grid including all diagonals. *All* points in the figure are considered connected to the central one at $(0.07, 0.05, 0.07)$.

with the base material having Young's modulus E^0 and Poisson's ratio $\nu^0 = 0.3$. Firstly, a microstructure for $E_x = E_y = E_z = 0.25E^0$ is found (Fig. 5.3). All other key microstructures are optimised using a neighbouring key microstructure as the starting structure. The neighbourhood had 26 point connectivity as illustrated in Fig. 5.4. The neighbour chosen to seed a particular key microstructure is the neighbour closest to the initial structure in the parameter space. Thus all the key microstructures in the parameter space are generated in a tree like fashion with $E_x = E_y = E_z = 0.25E^0$ being the root. In this way the geometry of all the key microstructures should be similar facilitating the use of shape interpolation.

The microstructures are checked to ensure that microstructures are similar enough for sensible shape interpolation and to ensure that the microstructures match their parameterisation. A key microstructure is considered to have satisfied its constraints if the Frobenius norm of the error is below 0.005. That is, if E_x is the actual Young's modulus in the x direction and E_x^{t} is the target, similar for E_y, E_z, γ_{xy}, γ_{xz} and γ_{yz}, then a microstructure is considered to have

satisfied its constraints if

$$\left(\frac{E_x - E_x^{\mathrm{t}}}{E^0}\right)^2 + \left(\frac{E_y - E_y^{\mathrm{t}}}{E^0}\right)^2 + \left(\frac{E_z - E_z^{\mathrm{t}}}{E^0}\right)^2 + (\gamma_{xy} - \gamma_{xy}^{\mathrm{t}})^2 + (\gamma_{xz} - \gamma_{xz}^{\mathrm{t}})^2 + (\gamma_{yz} - \gamma_{yz}^{\mathrm{t}})^2 \leq 0.005. \tag{5.21}$$

For a key microstructure to be considered satisfactory it is required to satisfy (5.21) and to have the same surface genus as the original microstructure.

Each microstructural optimisation has a number of parameters associated with it. For example, one of the optimisation parameters controls the speed of the level set front. As a large number of optimisations need to be performed, a full optimisation parameter sweep is not undertaken as in the previous chapters. Rather, if a satisfactory key microstructure cannot be found with one set of optimisation parameters then a number of optimisation parameter sets are considered in turn. Note that satisfactory microstructures can not be found for every considered set of Young's moduli. In addition, if a key microstructure does not have enough neighbours to be able to contribute to shape interpolation, it is removed.

To reduce the number of microstructural optimisations required, optimisations are performed only for

$$E_x \leq E_y \leq E_z. \tag{5.22}$$

The full set of key microstructures are then obtained through reflections from the reduced set. This reduces the number of microstructural optimisations from $21^3 = 9261$ to $\left(\!\!\binom{21}{3}\!\!\right) = \binom{21+2}{3} = 1771$. The microstructure optimisations were performed on a cluster utilising a mix of Nvidia C2050, C2070, and S2050 GPUs with the time taken being on the order of a few weeks.

5.2.3 Microstructure interpolation

Once the set of key microstructures is generated, interpolation is used to obtain the full microstructure set. The multiparametric microstructure interpolation used is a generalisation of that seen in Chapter 3. The major difference is the use of trilinear interpolation instead of linear interpolation for the distance functions.

Here we describe the interpolated microstructure $\Gamma(E_1, E_2, E_3)$ corresponding to the parameter vector (E_1, E_2, E_3). Let E_i^0 be the largest number in $\mathcal{E}^{\mathrm{key}}$ such that $E_i^0 < E_i$. Further let E_i^1 be the smallest number in $\mathcal{E}^{\mathrm{key}}$ such that $E_i^1 \geq E_i$. In this way, (E_1^i, E_2^j, E_3^k) are the points in $\mathcal{E}^{\mathrm{key}} \times \mathcal{E}^{\mathrm{key}} \times \mathcal{E}^{\mathrm{key}}$ surrounding (E_1, E_2, E_3) as illustrated in Fig. 5.5. Let $d^{ijk}(\boldsymbol{x})$ be the signed

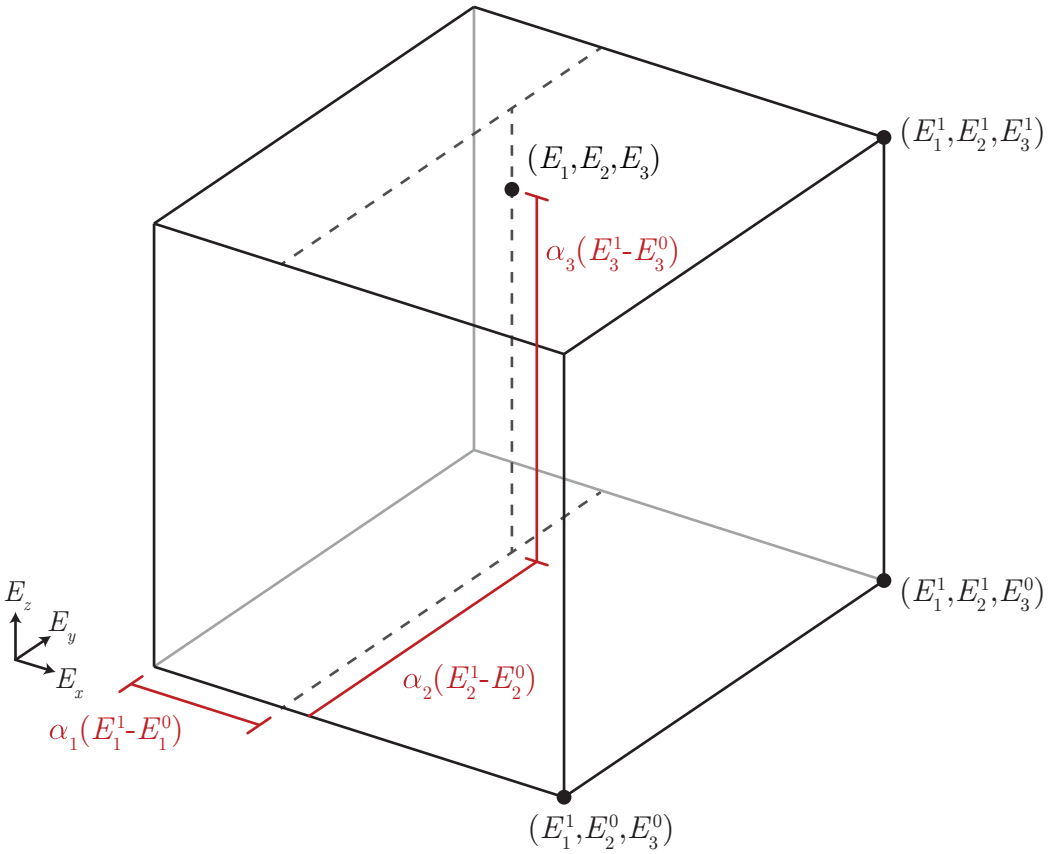

FIGURE 5.5: The neighbourhood around the parameter vector (E_1, E_2, E_3). The corners (E_1^i, E_2^j, E_3^k) correspond to key microstructures from which interior points are interpolated. The α_i vary linearly from 0 to 1 within the hexahedron.

distance to the surface of the key microstructure with parameters (E_1^i, E_2^j, E_3^k). As before, let positive distance signal the solid interior of the microstructure and negative distance signal void. Finally, let

$$\alpha_i = \frac{E_i - E_i^0}{E_i^1 - E_i^0} \tag{5.23}$$

so that α_i varies linearly from 0 to 1 moving across the interpolation hexahedron (Fig. 5.5).

The trilinearly interpolated distance function is then

$$d(\boldsymbol{x}) = \sum_{a_1\in\{0,1\}} \sum_{a_2\in\{0,1\}} \sum_{a_3\in\{0,1\}} \left(\prod_{i\in\{1,2,3\}} (1 - a_i + \alpha_i(2a_i - 1)) \right) d^{a_1a_2a_3}(\boldsymbol{x}). \tag{5.24}$$

Similar to Chapter 3, the final interpolated shape is

$$\Gamma = \{\boldsymbol{x} \,|\, d(\boldsymbol{x}) \geq \beta\}, \tag{5.25}$$

where β is chosen so that the volume fraction of the microstructure is trilinearly interpolated between the 8 key microstructures.

5.2.4 Results

Fig. 5.6 shows the space of satisfactory microstructures found along with their volume fractions. It also shows which microstructures were removed from the set for the macroscopic optimisation due to not having enough neighbours for interpolation. It was the most difficult to find satisfactory microstructures for the parameter sets with more extreme ratios of Young's moduli. The microstructure found with the most extreme ratio of Young's moduli was $E_x/E^0 = 0.1$, $E_y/E^0 = 0.25$, and $E_z/E^0 = 0.45$ with a ratio $E_x/E_z = \frac{2}{9}$.

Fig. 5.7 shows four examples of optimised microstructures with a range of Young's modulus ratios. The first three are on the edge of what was produced — parameter sets using these microstructures as starting points did not find satisfactory structures — while the fourth is surrounded in the parameter space by satisfactory structures. The first two have small, thin members along the axis of lowest Young's modulus while the internal structure in the third has been reduced to mere slots. If the ratio of the Young's moduli were to go higher, these small scale details may reduce in size and, without mesh refinement, may disappear entirely, changing the topology. This suggests that higher Young's modulus ratios might be possible with mesh refinement, however with the computational resources available such refinement was not feasible.

The third microstructure (Fig. 5.7c) appears to inhibit the flow of stress in the x and y directions while using a large amount of material to satisfy the E_z constraint. This suggests that the volume of material used may not be 'efficient' and higher Young's moduli could be achieved in the x and y directions without a change in volume fraction. While of interest, the macroscopic optimisation problem examined in this chapter does not consider material cost to be significant, however such optimisation problems could be considered in future work.

It is impractical to perform repeated homogenisation calculations for each point in the macroscopic domain for the macroscopic optimisation. As such, the macroscopic optimisation uses effective stiffness tensors that are trilinearly interpolated from the key microstructures' effective tensors. To assess the validity of this approximation, points are chosen mid-way between each neighbouring key microstructure and the effective stiffness tensor of the interpolated microstructure was compared to the interpolated stiffness tensor. If C_{ijkl}^{approx} is the stiffness tensor approximated from the key tensors, and C_{ijkl}^{true} is the true stiffness tensor calculated from the

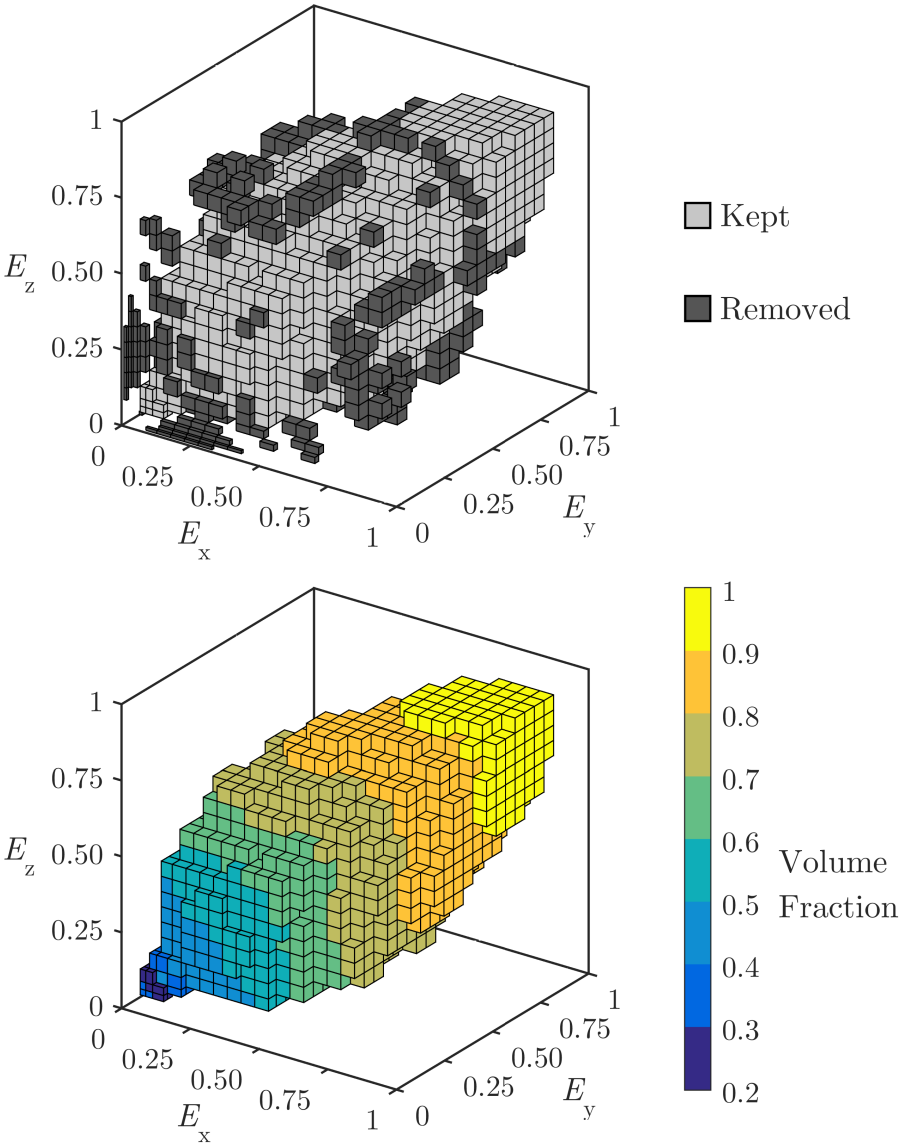

FIGURE 5.6: Obtained microstructure parameter space. A cube exists at a location if a microstructure was found matching those properties. (**top**) Microstructures were discarded if they did not contain sufficient neighbours to interpolate with. (**bottom**) Cubes are coloured by the volume fraction of the resulting microstructure. The volume fraction seems strongly dependent on the largest Young's modulus.

interpolated microstructure, then the relative error was calculated with the Frobenius norm as

$$\mathrm{err} = \sqrt{\frac{(C^{\mathrm{true}}_{ijkl} - C^{\mathrm{approx}}_{ijkl})(C^{\mathrm{true}}_{ijkl} - C^{\mathrm{approx}}_{ijkl})}{C^{\mathrm{approx}}_{mnpq} C^{\mathrm{approx}}_{mnpq}}}. \tag{5.26}$$

The distribution of the calculated errors are shown in Fig. 5.8. The microstructures are approximated satisfactorily with the majority of the approximations having relative error below

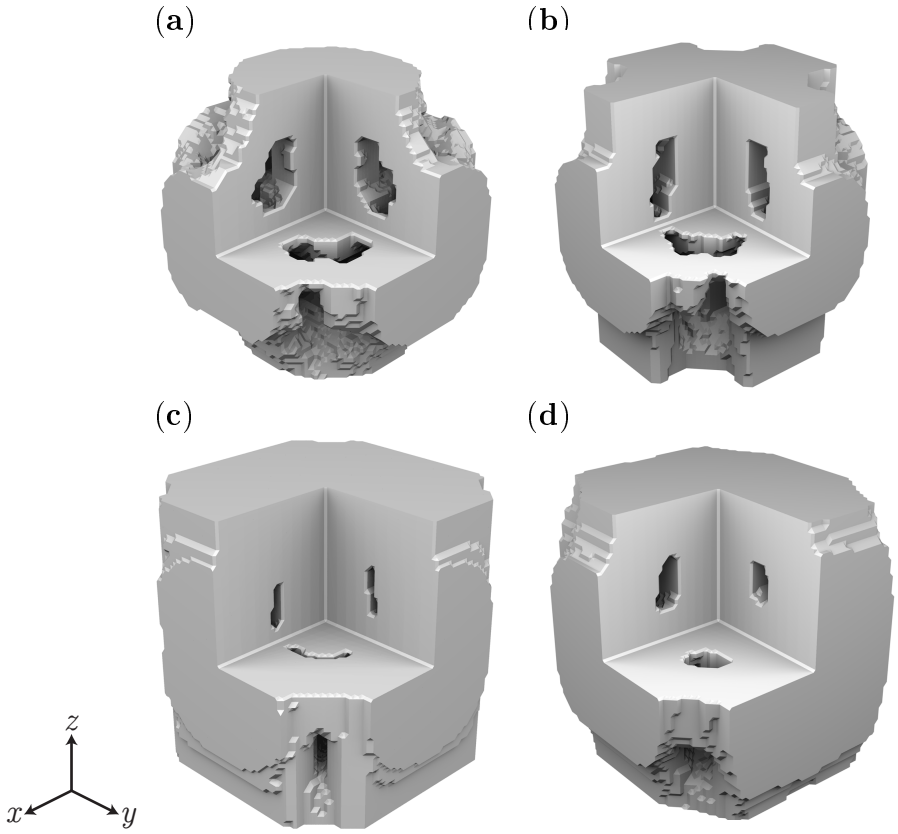

FIGURE 5.7: Some of the optimised microstructures with the front octant removed to show internal structure. (**a**) $E_x = 0.1E^0$, $E_y = 0.1E^0$, $E_z = 0.2E^0$. (**b**) $E_x = 0.1E^0$, $E_y = 0.1E^0$, $E_z = 0.4E^0$. (**c**) $E_x = 0.4E^0$, $E_y = 0.4E^0$, $E_z = 0.8E^0$. (**d**) $E_x = 0.35E^0$, $E_y = 0.5E^0$, $E_z = 0.65E^0$.

0.05. There are a small number (3.2%) with error larger than 0.1 but no more than 0.25. The high error approximations occur on the edges of the parameter space, predominantly with extreme values of solid volume fraction. The interpolation for these extreme microstructures would likely be improved with an increase in microstructure resolution.

5.3 Macroscopic Optimisation

Now that a suitable microstructure set has been developed, similar to previous chapters we utilise this set for a macroscopic optimisation using the MIMO method. As low volume fraction microstructures were difficult to produce, solid-void solutions will be difficult to obtain. A compliance optimisation problem, which typically involves regions of void (as in Chapter 3), would therefore be an inappropriate test case. We test this new multiparametric microstructure set using the bone prosthesis design problem from Chapter 4.

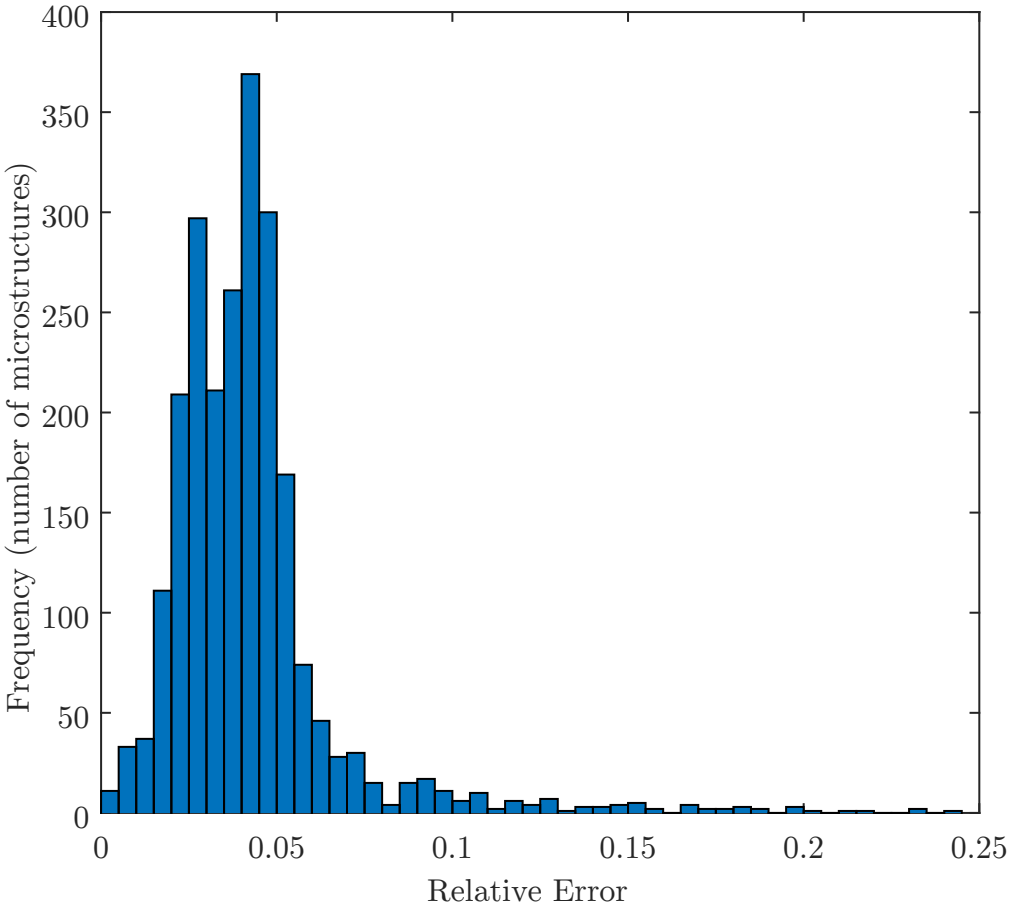

FIGURE 5.8: Error in interpolated effective material properties. Each pair, group of four, or group of eight neighbouring microstructures were interpolated between. The interpolated microstructure's effective stiffness tensor was calculated and compared to the approximated stiffness tensor with (5.26).

5.3.1 Optimisation problem

The optimisation problem is largely unchanged from that described in Section 4.2. The objective function F remains as (4.1) and the resorption m_r is quantified as (4.5). Recall,

$$F = \int_\Pi \tau^{2m}\, dS \tag{5.27}$$

$$m_\mathrm{r} = \frac{1}{|\Omega_\mathrm{B}^\mathrm{R}|} \sum_{e \in \Omega_\mathrm{B}^\mathrm{R}} \frac{1}{2} \tanh\left[a\left((1-s) - \frac{\int_e U\, d\boldsymbol{x}}{\int_e U_\mathrm{ref}\, d\boldsymbol{x}}\right)\right] + \frac{1}{2}. \tag{5.28}$$

The first major difference is that the optimisation is now no longer over a single parameter function, $\rho(\boldsymbol{x})$, but rather three, $E_x(\boldsymbol{x})$, $E_y(\boldsymbol{x})$, and $E_z(\boldsymbol{x})$. The optimisation problem is

$$\min_{E_x(\boldsymbol{x}),E_y(\boldsymbol{x}),E_z(\boldsymbol{x})} F(E_x(\boldsymbol{x}),E_y(\boldsymbol{x}),E_z(\boldsymbol{x}),\boldsymbol{u})$$
$$\text{subject to } \begin{cases} \boldsymbol{u} = \underset{\boldsymbol{u}'}{\operatorname{argmin}} \dfrac{1}{2}\displaystyle\int_\Omega \varepsilon_{ij}(\boldsymbol{u}')C_{ijkl}(E_x,E_y,E_z)\varepsilon_{kl}(\boldsymbol{u}')\,dV \\ \qquad\qquad - \displaystyle\int_{\partial\Omega} u_i' t_i\,dS \\ m_{\mathrm{r}}(\boldsymbol{u}) \leq 0.05 \\ \frac{1}{|\Omega_{\mathrm{P}}|}\int_{\Omega_{\mathrm{P}}} p(E_x,E_y,E_z)\,dV \leq p_{\mathrm{lim}}, \end{cases} \tag{5.29}$$

where $E_x(\boldsymbol{x})$, $E_y(\boldsymbol{x})$, and $E_z(\boldsymbol{x})$ are the functions that together map a location in the macroscopic design to a microstructure and its properties.

The only differences between (4.6) and (5.29) is the change in parameterisation and the addition of a further optimisation constraint to ensure that the parameters in the macroscopic description do map to admissible parameters with satisfactory microstructures. This penalty function, p, is integrated over the whole prosthesis domain Ω_{P}. Let the space of all microstructures found along with all microstructures that can be interpolated be Θ. Let the space of all other microstructures not in Θ be Θ^{c}. The function $p(E_x,E_y,E_z)$ is the distance from (E_x,E_y,E_z) to Θ. Following this definition, if $(E_x,E_y,E_z) \in \Theta$ then $p(E_x,E_y,E_z) = 0$, and if $(E_x,E_y,E_z) \in \Theta^{\mathrm{c}}$ then $p(E_x,E_y,E_z) > 0$. The primary benefit of using such a distance function is that the derivatives provide direction information to the optimiser as to which way Θ lies when a macroscopic element violates the constraint. The penalty function was smoothed with a Gaussian filter so as to remove the stepped shape of Θ that may be problematic for the optimiser. The optimisation was performed both with and without the enforcement of the penalty constraint in order to see how the macroscopic optimisation performs with a broader search space.

5.3.2 Filling the microstructural space

While the penalty function should ensure that the microstructures do exist in the final design, the optimiser may stray outside of that space temporarily. As such, the domain of C_{ijkl} needs to be $\Theta \cup \Theta^{\mathrm{c}}$, not just Θ, requiring the "effective" elastic tensors for points in Θ^{c} to be specified. The three Young's moduli used to parameterise the space along with (5.8) leaves three degrees of freedom in the elastic tensor, those related to the Poisson's ratios. We remove these degrees of freedom by matching properties with the closest microstructure in Θ.

Possible choices of "filler" tensors for Θ^{c} include a single constant tensor or matching Poisson's ratios. If a constant tensor was used then the material properties will change very rapidly at the boundary between Θ and Θ^{c} which would be detrimental to the macroscopic optimisation. The optimiser may make use of the large range of (inadmissible) effective properties on the fringe of Θ, resulting in a design that is not physically realisable, and with predicted elastic properties far from any physically realisable design. On the other hand, setting the Poisson's ratios to be equal to a nearby microstructure in Θ leads to making a choice between the mutually exclusive options of setting ν_{xy} to match or setting ν_{yx} to match.

Let (without implied summation)

$$\xi_{ij}(C_{klmn}) = \frac{(E_i + E_j)\nu_{ij}}{E_i}. \tag{5.30}$$

The value ξ_{ij} is dimensionless similar to ν_{ij} and if $E_i = E_j$ then $\xi_{ij} = \nu_{ij}$. The benefit of ξ_{ij} is that it is symmetric in i and j removing the choice present for ν_{ij}. If $\boldsymbol{a} = (E_x, E_y, E_z) \in \Theta^{\mathrm{c}}$, and $\boldsymbol{b} \in \Theta$ is the nearest admissible microstructure to $\boldsymbol{a}$, then we set

$$\xi_{ij}(C_{klmn}(\boldsymbol{a})) = \xi_{ij}(C_{klmn}(\boldsymbol{b})). \tag{5.31}$$

And so the last three degrees of freedom are removed and the full elastic tensor $C_{ijkl}(\boldsymbol{a})$ is specified, even for those parameters that do not have a matching microstructure.

5.3.3 Other microstructural details

As in Chapter 4, two isotropic base materials are tested, both having Poisson's ratio of $\nu^0 = 0.3$ and Young's moduli $E^0 = 60\text{GPa}$ and $E^0 = 100\text{GPa}$. The value of m was also varied, using $m = 1$ and $m = 2$ as in Chapter 4. The axes of the microstructure were first aligned to the macroscopic domain, and secondly with the microstructure rotated about the y axis (similar to microstructure set D in Chapter 4). The microstructure set developed in Section 5.2 will be labelled E, continuing with the lettered labelling of microstructures from Chapter 4.

A final comparison microstructure family is also tested, that of an orthotropic cross — designated microstructure set F. The orthotropic cross is similar to the cubic cross structure (set B in Chapter 4) except that the cross-sectional area of each arm is allowed to vary independently. An example can be seen in Fig. 5.9 along with the resultant directional Young's modulus. There are directions in which the stiffness is quite low in comparison to the axial stiffness, such as in the $(1, -1, 1)$ direction out of the page. We compare against this microstructure as it is one

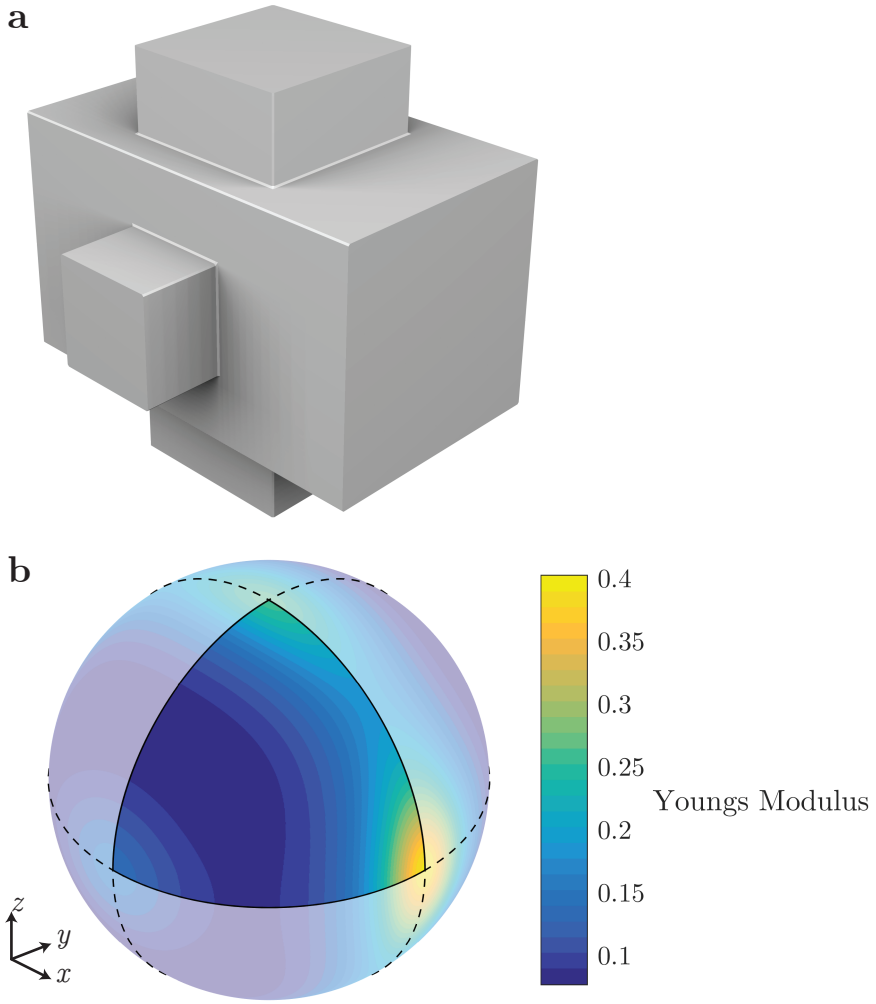

FIGURE 5.9: Example of an orthotropic cross structure. The faces have area equal to 35%, 7% and 18% of the representative cube's faces in the x, y and z directions respectively. (**a**) A single cell of the structure's geometry. (**b**) The directional dependence of the Young's modulus. Units are normalised to the base material Young's modulus. Compare to Fig. 5.2 and note that here the direction with the lowest Young's modulus is on the diagonal, approximately in the $(1, 1, 1)$ direction

of the simplest microstructures which has variance in three parameters corresponding to properties in different directions. Shape interpolation and the penalty constraint are not required for this orthotropic cross family, however to minimise the need for repeated homogenisation calculations effective properties were interpolated between a number of directly homogenised microstructures.

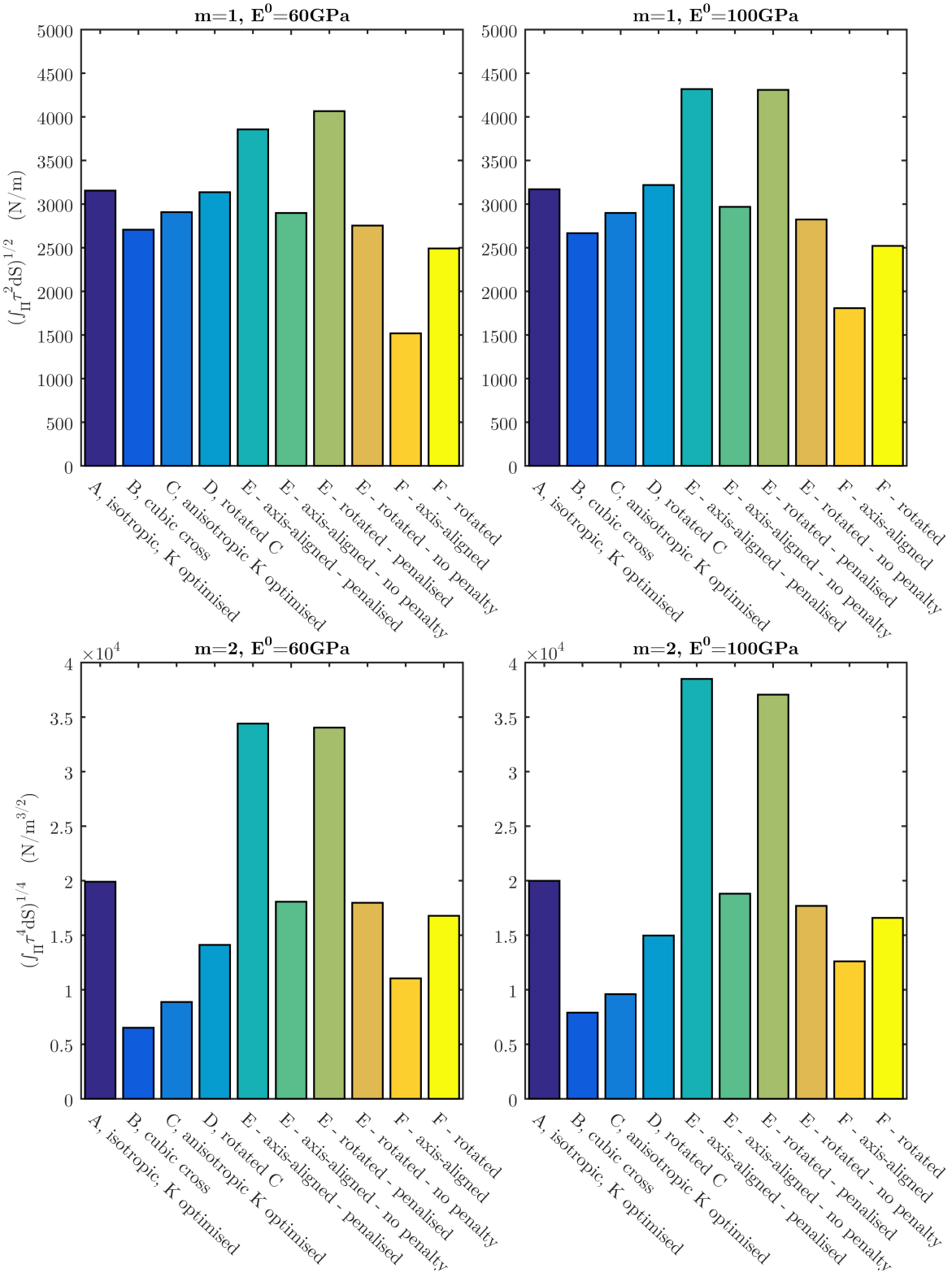

FIGURE 5.10: Visual comparison of the new multiparametric microstructure designs (sets E and F) and those found in Chapter 4. In particular, see Table 4.2 and Table 4.3. Note that these results have been rescaled from the results in the tables. By taking the $2m^{\text{th}}$ root the integral becomes the p-norm. This has been done to enable us to compare the results more easily.

TABLE 5.1: Macroscopic optimisation results for microstructure sets E and F with $m = 1$. The alignment of the microstructures is described as AA: the microstructure axes are aligned with the macroscopic domain, and rot.: the microstructure axes are rotated 45° about the y axis.

Base	Microstructure	With Penalisation			Without Penalisation		
Stiffness	and Alignment	$\int_\Pi \tau^2 dS$	m_r	Penalty	$\int_\Pi \tau^2 dS$	m_r	Penalty
60GPa	E - AA	1.49×10^7	0.05	0.11	8.40×10^6	0.05	13.28
100GPa	E - AA	1.86×10^7	0.11	0.08	8.81×10^6	0.05	13.66
60GPa	E - rot.	1.65×10^7	0.05	0.18	7.58×10^6	0.05	21.29
100GPa	E - rot.	1.86×10^7	0.11	0.10	7.97×10^6	0.05	20.26
60GPa	F - AA		—		2.31×10^6	0.05	—
100GPa	F - AA		—		3.27×10^6	0.05	—
60GPa	F - rot.		—		6.21×10^6	0.05	—
100GPa	F - rot.		—		6.36×10^6	0.05	—

TABLE 5.2: Macroscopic optimisation results for microstructure sets E and F with $m = 2$. The alignment of the microstructures is described as AA: the microstructure axes are aligned with the macroscopic domain, and rot.: the microstructure axes are rotated 45° about the y axis.

Base	Microstructure	With Penalisation			Without Penalisation		
Stiffness	and Alignment	$\int_\Pi \tau^4 dS$	m_r	Penalty	$\int_\Pi \tau^4 dS$	m_r	Penalty
60GPa	E - AA	1.40×10^{18}	0.05	0.07	1.07×10^{17}	0.05	12.23
100GPa	E - AA	2.20×10^{18}	0.11	0.06	1.25×10^{17}	0.05	13.45
60GPa	E - rot.	1.34×10^{18}	0.05	0.14	1.04×10^{17}	0.05	15.33
100GPa	E - rot.	1.89×10^{18}	0.11	0.11	9.79×10^{16}	0.05	23.55
60GPa	F - AA		—		1.49×10^{16}	0.05	—
100GPa	F - AA		—		2.52×10^{16}	0.06	—
60GPa	F - rot.		—		7.93×10^{16}	0.05	—
100GPa	F - rot.		—		7.58×10^{16}	0.05	—

5.4 Results and discussion

The final optimised objective values and constraint values are shown in Tables 5.1 and 5.2, and also graphically in Fig. 5.10. Recall that microstructure set E is the set developed in Section 5.2 parameterised by the axial Young's moduli and microstructure set F is the orthotropic cross. Some of the optimised design layouts are also shown. Two examples are presented using microstructure set E with (Fig. 5.11) and without (Fig. 5.12) the penalisation constraint active. Two other examples show designs using microstructure set F axially aligned (Fig. 5.13) and rotated (Fig. 5.14). An illustration of a microstructure set F design is shown in Fig. 5.15.

While the penalisation is effective in keeping the optimisation from using microstructures from Θ^c, it has a large adverse effect on the objective results compared to when no penalty is used.

While this difference is expected, microstructure set A outperformed microstructure set E when the penalisation was used. Microstructure set E is essentially a superset of microstructure set A, where microstructure set A is restricted to $E_x = E_y = E_z$ due to the isotropy constraint.[2] Designs utilising microstructure set A can be closely reproduced using the parameterisation for set E and so the optimal design for set E should have an objective value no worse than that of the optimised design with set A. The fact that the design with microstructure set A improves on that with the broader set E when using the penalisation suggests that the penalisation unduly interferes with the optimisation.

The designs where the penalisation is enforced (e.g. Fig. 5.12) show much less variation in microstructures used than those without the penalisation. In fact, these designs in which the penalisation is enforced appear to be almost homogeneous with a single microstructure used for the majority of the design. Different homogeneous initial macroscopic designs were tried resulting in the same microstructure used throughout suggesting that the design is not an artefact of the initial condition. The penalty function has the constant value of 0 in the neighbourhood about the widely used microstructure and so should not preference that particular microstructure due to the penalty function.

The nonlinear optimiser used is the GCMMA (Svanberg, 2002) which may be a suboptimal choice for such a complex search space. The MMA approximates the functions being optimised (both the objective and constraints) with locally quadratic functions having vertical asymptotes chosen heuristically to keep the approximation from taking too large a step. The method is made globally convergent by ensuring that each step the optimiser takes is conservative. Conservative here means that when the optimiser takes a step with the approximation function predicting a greater benefit than is realised, a smaller step is taken. In this case, when any elements have microstructure parameters near the edge of Θ, the sudden change to p being non-zero may cause the optimiser to take very small steps due to this conservative requirement. This would explain both the almost homogeneous nature of the solutions and their poor performance.

In contrast to the designs utilising the penalisation constraint, without the penalisation much variation is seen (as in Fig. 5.12). Variation in the design occurs over both long and short length scales (Fig. 5.16). Regions of rapid change over short length scales remains manufacturable so long as the length scale of the macroscopic change is larger than the microstructure length scale. The fact that the results without the penalisation scheme provide an improvement over those that do suggests there is value in extending the space of allowed microstructures. The closed cells such as those used in Chapter 3 are a family of microstructures that may be easier

[2] The elastic isotropy constraint produces microstructures for set A that are valid for set E, and both are optimised for void conductivity. In practice there are minor differences in the microstructures produced.

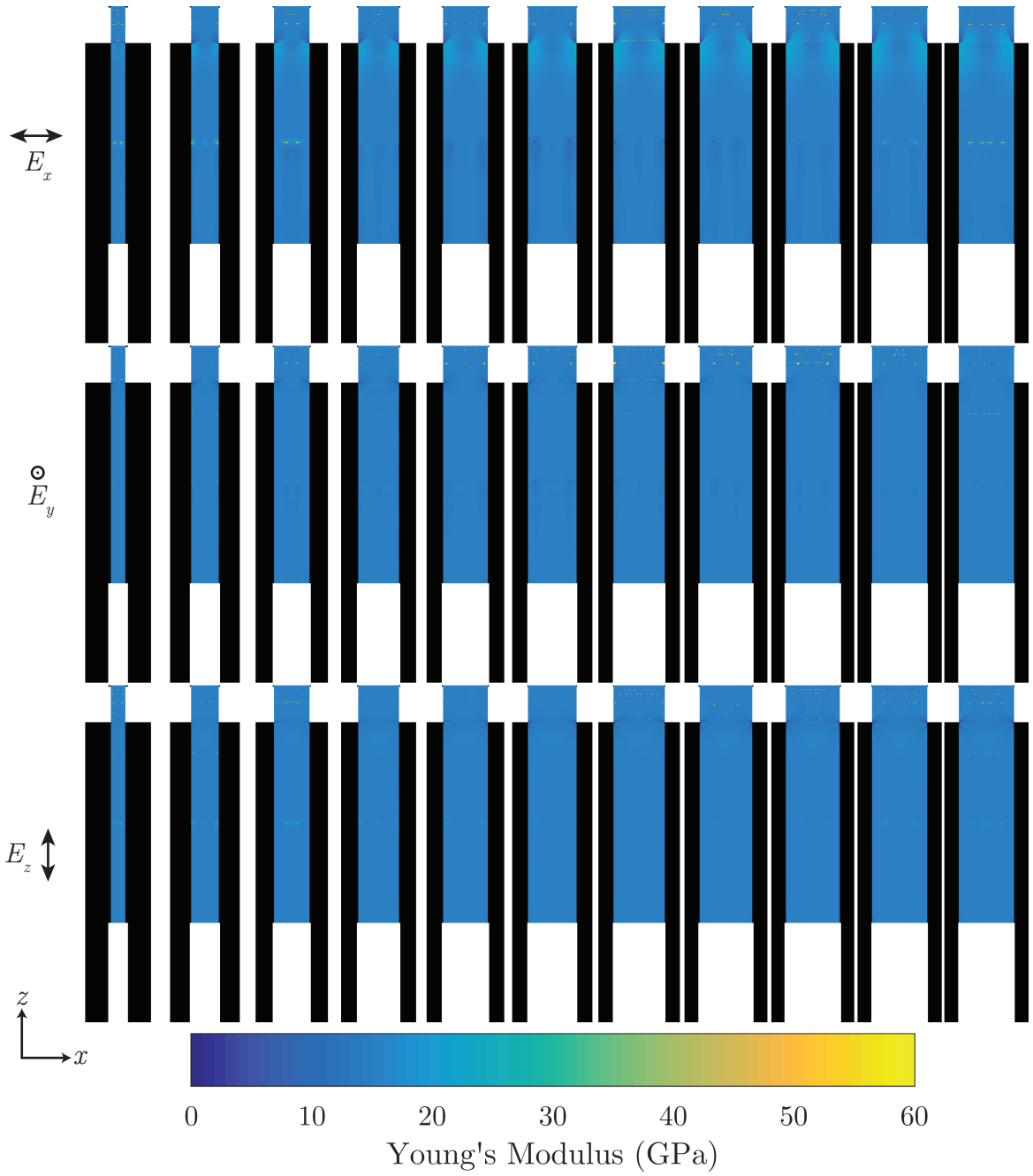

FIGURE 5.11: Macroscopic design using microstructure set E using the penalty function ($E^0 = 60$GPa, $m = 1$). Note the almost uniform microstructure choice for the full design, however there is softening above the bone-prosthetic interface, Π. The design is split into each of the parameter functions as labelled on the left. The design is further split into slices in the x-z plane ranging from the edge (left) to the middle (right) of the design.

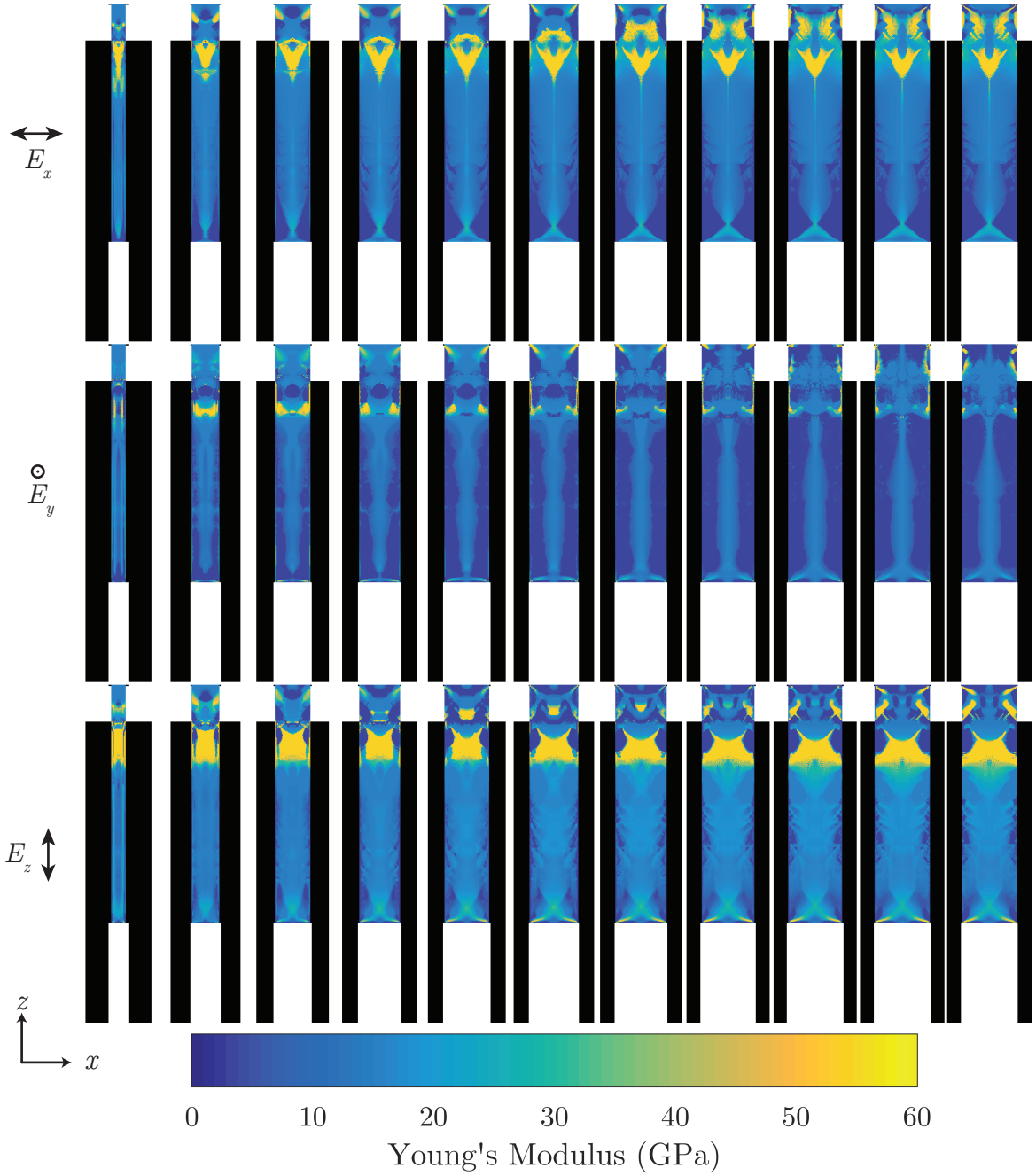

FIGURE 5.12: Macroscopic design using microstructure set E without the penalty function ($E^0 = 60$GPa, $m = 1$). There is much more variation than in Fig. 5.11. The design is split into each of the parameter functions as labelled on the left. The design is further split into slices in the x-z plane ranging from the edge (left) to the middle (right) of the design.

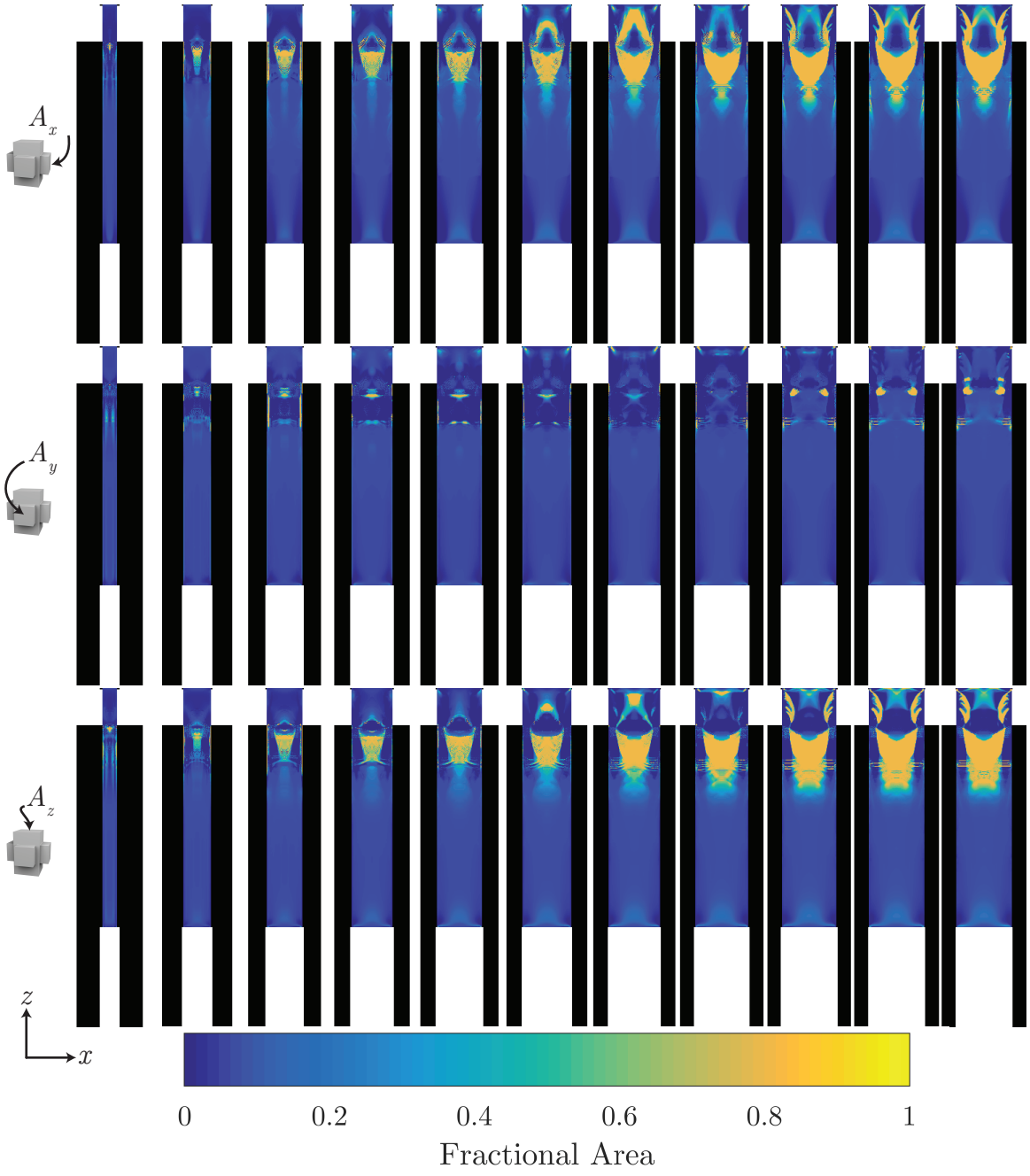

FIGURE 5.13: Macroscopic design using microstructure set F axially aligned ($E^0 = 60$GPa, $m = 1$). The displayed fractional area is the cross sectional area of the microstructure arm compared to the matching representative volume face. The design is split into each of the parameter functions as labelled on the left. The design is further split into slices in the x-z plane ranging from the edge (left) to the middle (right) of the design.

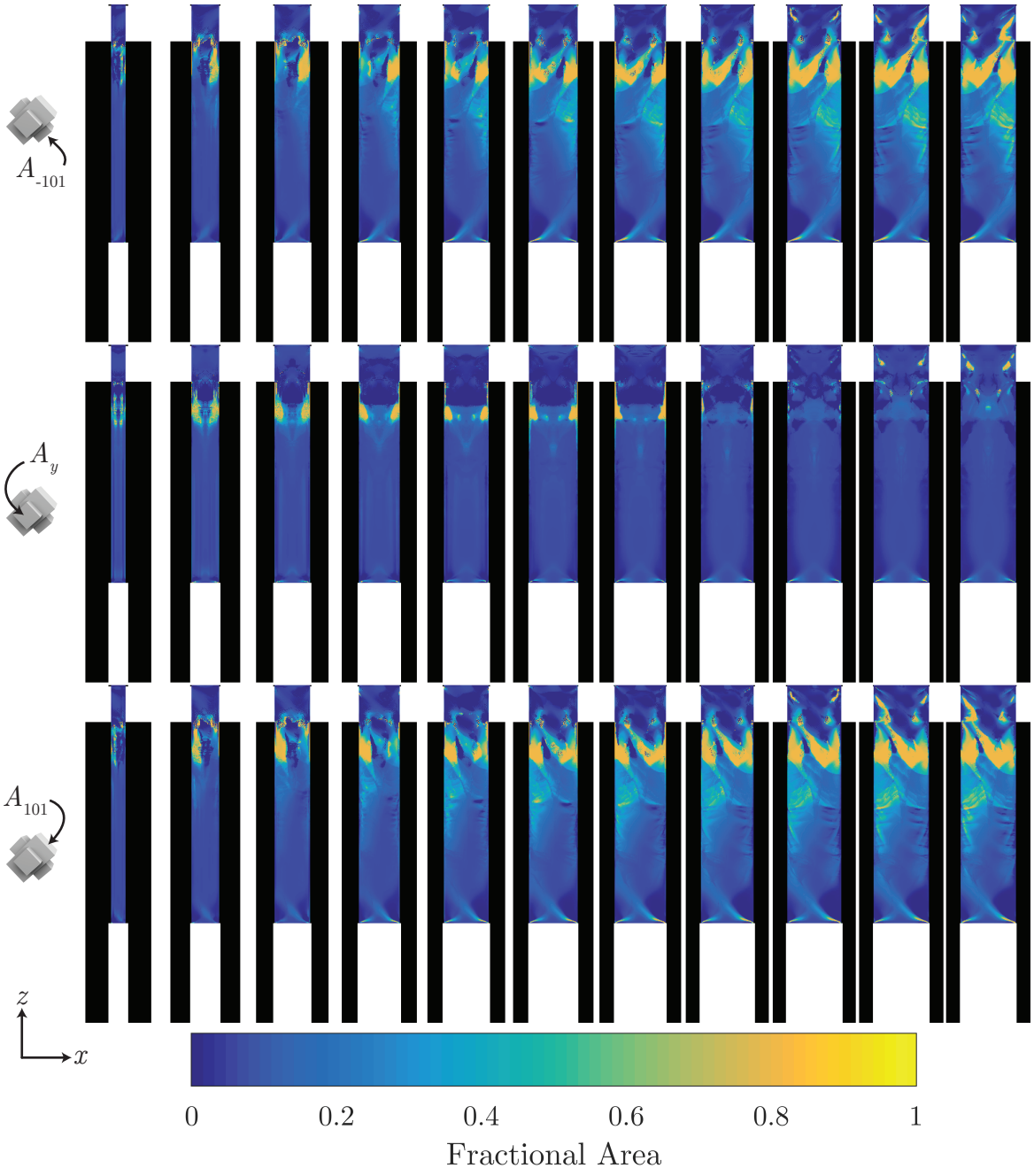

FIGURE 5.14: Macroscopic design using microstructure set F rotated by 45° about the y axis ($E^0 = 60$GPa, $m = 1$). The left-right symmetry is lost due to the rotation of the microstructures, however a new symmetry is created between A_{-101} and A_{101}. The design is split into each of the parameter functions as labelled on the left. The design is further split into slices in the x-z plane ranging from the edge (left) to the middle (right) of the design.

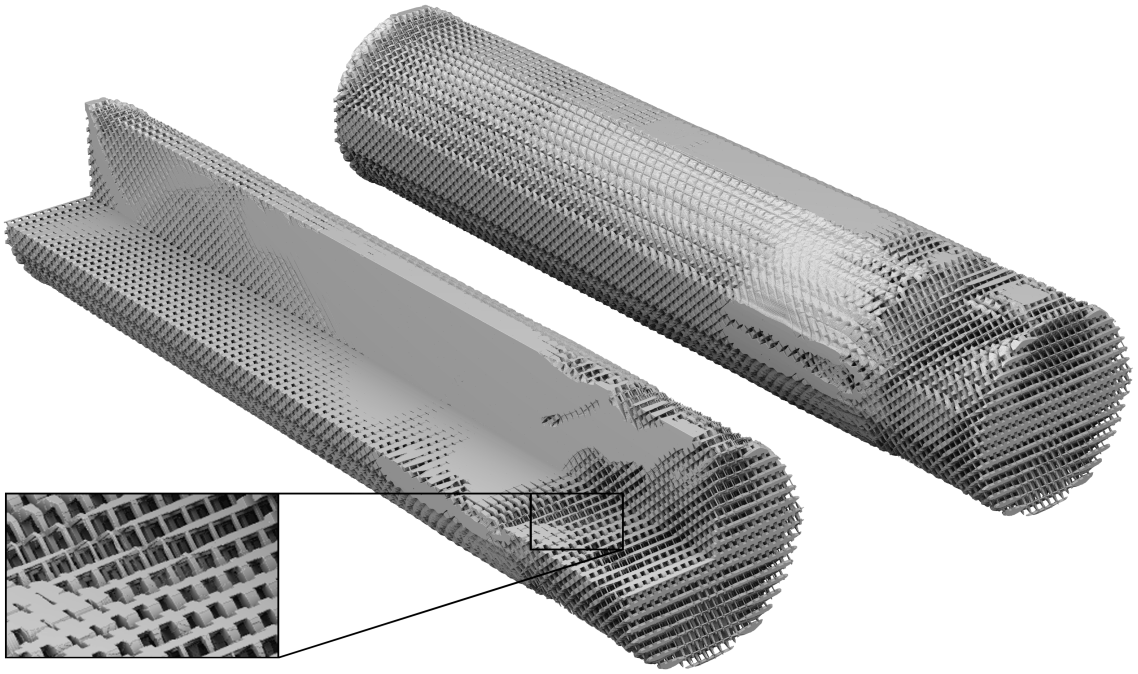

FIGURE 5.15: Multiparametric design illustration of the design in Fig. 5.14. Microstructure length scale is figurative only.

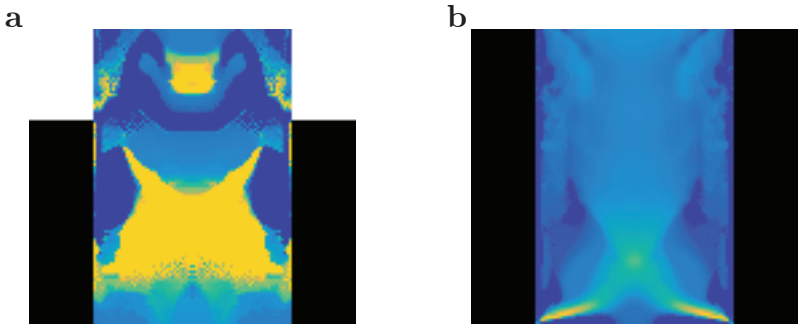

FIGURE 5.16: Zoomed view of the 60GPa, microstructure set E, no penalisation design (Fig. 5.12) showing both rapid and slow variation. (**a**) Rapid variation near the proximal end (top) of the prosthesis. (**b**) Slow variation near the distal end (bottom) of the prosthesis.

to extend into the desired microstructural parameter space. They do however pose problems to additive manufacture; SLM for example requires open cells to remove waste material.

While microstructure set E can be thought of as a generalisation of microstructure set A, microstructure set F is a true generalisation of microstructure set B, the cubic cross structure. No penalisation was necessary for microstructure set F as the set has a valid microstructure for the full range of parameters considered. Some examples of the optimised macroscopic structures can be seen in Fig. 5.13 and Fig. 5.14. Microstructure set F shows clear gains over most other microstructure sets, curiously being bettered only by microstructure set B when

$m = 2$. Clearly then, the larger multiparametric search space itself causes difficulties for the optimisation algorithm even without the presence of the penalisation constraint.

In order to ensure that no errors were made, some additional optimisations were performed using microstructure set E initialised with the solution obtained for set A and using microstructure set F initialised with the solution obtained for set B. These additional optimisations, compared to their initial designs, gave results that are no worse, and in some cases better. This confirms that better solutions exist utilising microstructure sets E and F than are found in the initial optimisations. While informative, such optimisations are not practical as their production requires a solution to already be found.

5.5 Application to FGMs

While causing some difficulties within the macroscopic optimisation, the multiparametric microstructure sets produced in this chapter are well suited to the field of functionally graded materials (FGMs). Using microstructures from the set allows variation of a number of material properties in independent directions while maintaining connectedness of the microstructures.

For example, consider a cylinder with a prescribed vertical Young's modulus (E_z) varying from the bottom to the top, and a prescribed Poisson's ratio ($\nu_{zx} = \nu_{zy}$) varying from the centre of the cylinder to the edge. There are two functional gradients along two separate axes, the ν_{zx} gradient is shown in Fig. 5.17a, while the E_z gradient is shown in Fig. 5.17b. Microstructures can be selected from set E to satisfy these two gradients.

Due to radial symmetry and the prescribed $\nu_{zx} = \nu_{zy}$, we have that $E_x = E_y$ while E_z is fixed due to its prescribed gradient. In order to select the correct microstructure, E_x (and thus E_y) must be chosen. Inverting the single parameter function $\nu_{xz}(E_x; E_z)$, the correct E_x becomes apparent. The E_x field required to satisfy the two functional gradients is shown in Fig. 5.17b while the subset of microstructures used to achieve the prescribed properties is shown in Fig. 5.18. An illustration of the full multiscale design is shown in Fig. 5.19.

Such a design is more complicated than has been addressed in the FGM literature, yet is accomplished easily with the MIMO method and the multiparametric microstructure set found in this chapter. The connectively problem tackled for the case of FGMs by Zhou and Li (2008a,b) is solved here through the interpolation approach. Unfortunately, the same trade-off applies to both the FGM examples as to the macroscopic optimisation examples: the microstructures used are less general and more constrained than could be manifested by other methods (e.g. Zhou and Li, 2008a,b). In particular, topology changes are difficult with the interpolation method.

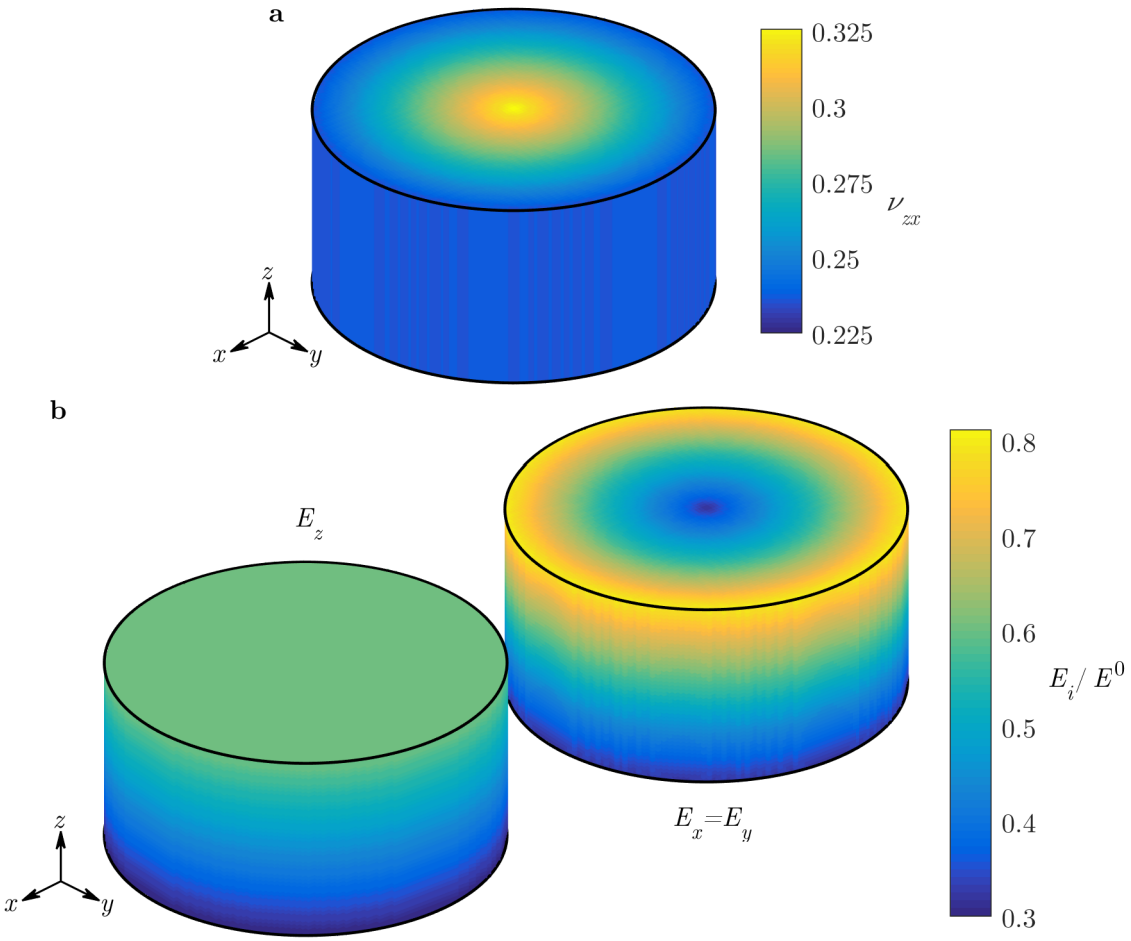

FIGURE 5.17: A functionally graded design example. (**a**) The required Poisson's ratio ν_{zx} decreases from the centre of the domain to the edge. (**b**) The required Young's modulus E_z increases from bottom to top. Also shown is the resultant Young's moduli $E_x = E_y$ that provide the specified Poisson's ratio using microstructure set E.

5.6 Conclusion

In this chapter the microstructure interpolation for macroscopic optimisation (MIMO) method was extended to make use of a higher dimensional microstructure set. This set was parameterised by the effective axial Young's moduli of the microstructures with constraints to ensure that the stiffness is well behaved in all directions, varying monotonically between the axes. The set was produced by choosing an initial key microstructure, and using it to seed the optimisations for the neighbouring key microstructures. The full continuous set was produced by trilinearly interpolating between signed distance functions representing the key microstructures.

The microstructure set was then utilised in a macroscopic bone prosthesis optimisation problem, as explored with single-parameter microstructure sets in Chapter 4. The microstructure

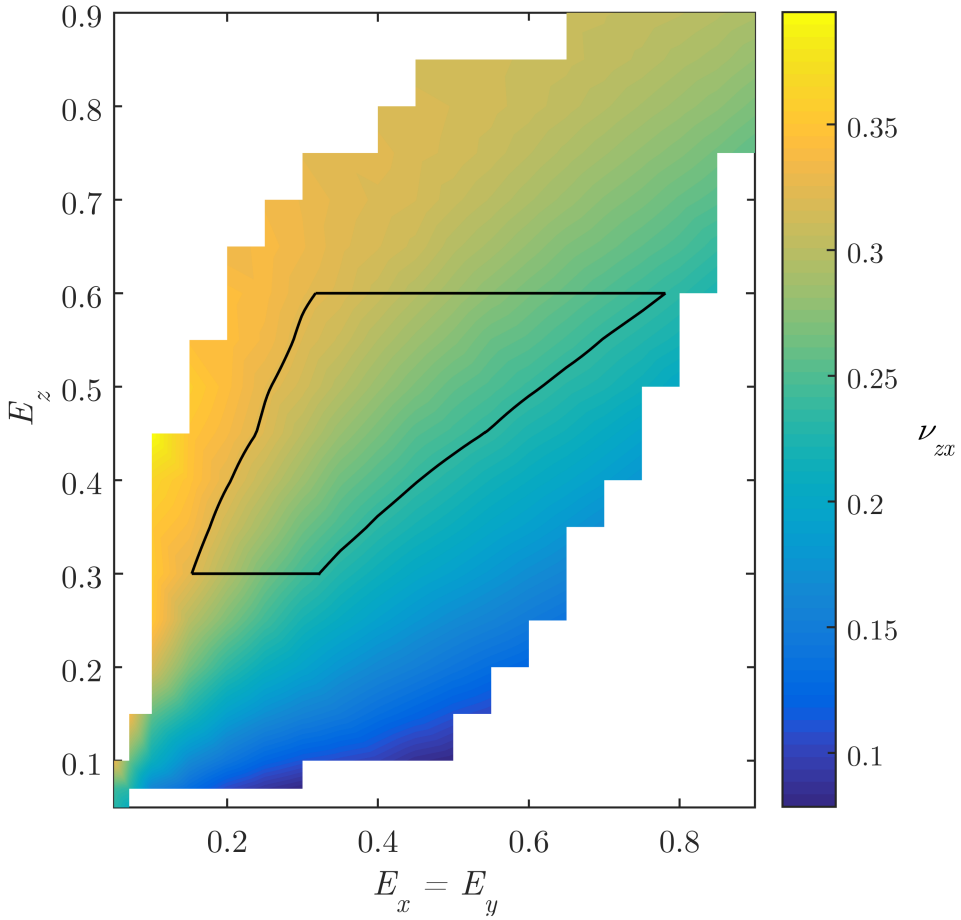

FIGURE 5.18: Parameter set used for the functionally graded example (Fig. 5.17). The Poisson's ratio ν_{zx} is shown in colour while white signifies that no structure can be interpolated for that set of parameters. The region outlined in black is the set of microstructures used for the design.

set produced did not provide a microstructure for every desired parameter choice and so a penalisation constraint was added. This constraint ensured only those parameters with a corresponding microstructure were used in the macroscopic optimisation. This constraint was found to have an adverse effect on the macroscopic optimisation, reducing the performance of the resulting designs beyond what was expected considering the experience of Chapter 4. When this penalisation was removed the optimisation produced satisfactory results, although in the case of the orthotropic cross microstructure set (F) the optimisation did not outperform previous designs using a subset of F (microstructure set B). This serves as a good illustration of the difficulties in non-linear optimisation, where there is typically no guarantee that the solution found is close to the global optimum. It suggests that more work should be done in exploring the non-linear optimisers used in the field of structural optimisation to ensure conclusions are not strongly influenced by the algorithm chosen.

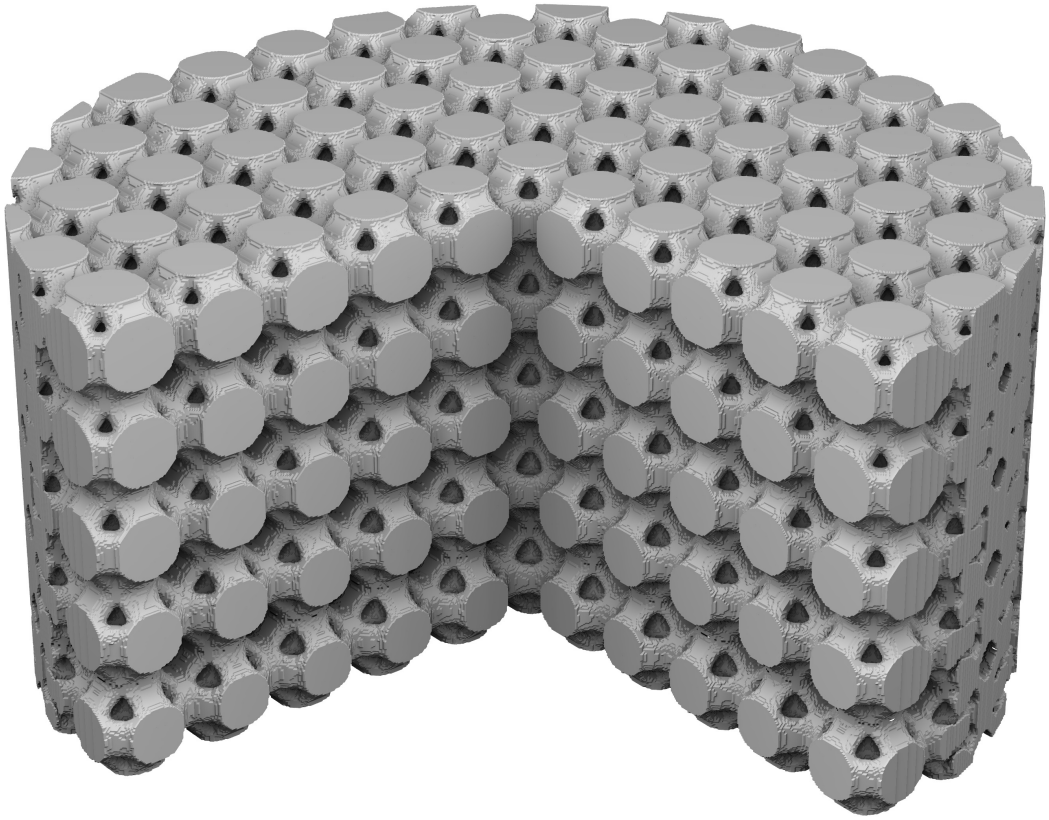

FIGURE 5.19: Illustration of a FGM design produced from the specification in Fig. 5.17. Note the varying pore sizes both vertically and radially. The front quadrant has been removed.

An example of how microstructure optimisation and shape interpolation can be applied to functionally graded materials was also given. A design example was proposed with two material properties varying in perpendicular directions and a design utilising the optimised orthotropic set of interpolated microstructures was generated fitting those requirements. The MIMO method described in this chapter could also be generalised to physics other than elasticity with microstructures parameterised by the elements of their conductivity tensor, for example, which may also prove useful applied to FGM problems.

The work in this chapter could be extended by exploring more microstructure classes. While closed cells such as those used in Chapter 3 cause difficulties for additive manufacture, it may be possible to find microstructures to fill the desired parameter space more easily. If so this would avoid some of the problems encountered with the open cells used here. Different parameterisations based on material properties other than stiffness could also be explored.

Chapter 6

Conclusion

At the beginning of this thesis we set out to develop a new multiscale design approach that ensures connectivity on the microscopic scale. This was achieved through the MIMO method, which uses *microstructure interpolation* of optimised microstructures for *macroscopic optimisation* with the material distribution method. In this concluding chapter we summarise the original results presented in the thesis and discuss the implications of the research.

6.1 Single Parameter Microstructure Interpolation

The MIMO method was developed in Chapter 3. A discrete set of key microstructures were optimised for effective bulk modulus while constrained to both be elastically isotropic and have a specified volume fraction between 0.1 and 0.9. This microstructure optimisation was performed using the level set method and produced periodic closed cells.

Shape interpolation of key microstructures produced a continuous set parameterised by the microstructure volume fraction (or density). Level set functions representing the two key microstructures were interpolated between, with interpolated microstructures defined by the level set which results in smoothly varying volume fraction. This microstructure interpolation scheme was shown to produce microstructures that vary smoothly in their geometry and also in their effective elastic properties. The full microstructure set was also shown to be close to the Hashin-Shtrikman theoretical upper bound for bulk modulus.

The full continuous interpolated set was then used in macroscopic compliance optimisation problems. A smooth function was fitted to the effective elastic properties of the microstructures to avoid repeated homogenisation calculations. In addition, derivatives of the effective properties can also be determined from the analytic expression of the fitted function. The fitted function matched the form of the Hashin-Shtrikman bounds and accurately described the effective material properties.

The macroscopic designs were optimised for compliance with point loads, distributed loads, multiple loads and worst-case loads both in two and three dimensions. The results were compared to designs optimised using the SIMP method to gauge the benefit over traditional single scale designs. The multiscale MIMO designs showed significant improvement over the single scale SIMP optimised designs in two dimensions. Significant portions of the designs used intermediate volume fraction microstructures between a solid outer shell and the load in all but one case where the optimisation produced a single-scale structure consisting of only solid and void. However, in three dimensions the MIMO designs typically used primarily solid material or void, preferencing thin vertical members over intermediate density microstructures and giving objectives comparable to the single-scale SIMP optimised designs.

6.2 Application to Bone Prosthetic Design

The MIMO method was applied to the design of femoral implants in Chapter 4. Femoral implants are typically optimised to minimise stress concentrations at the interface between the prosthetic and the existing femur, while minimising the undesirable effect of bone resorption. The MIMO method is a good fit for this problem, as it provides the ability to optimise a design with specific elastic properties throughout the domain while maintaining physical realisability. Previously optimised designs either had no method to produce the optimised material properties for manufacture (Kuiper and Huiskes, 1997), were restricted to two dimensions (Arabnejad Khanoki and Pasini, 2012), or were restricted to homogeneous designs only (Chanda et al., 2015b).

The optimisation problem considered in Chapter 4 generalised that of Kuiper and Huiskes (1997) to three dimensions using a similar objective and constraint. A number of microstructure sets were trialled, all with a connected pore space to allow for additive manufacture via SLM. The microstructure optimisations ensured a connected pore space by adding a void phase conductivity term to the optimisation. The microstructure choice was shown to be significant, as was the microstructure orientation in the case of elastically anisotropic microstructures.

The MIMO designs were shown to significantly improve upon homogeneous designs utilising only a single periodic microstructure, demonstrating merit for the MIMO method. In addition to providing benefits to the objective value, the pore space is also beneficial for bone ingrowth. Finally, the designs were shown to be physically interpretable and manufacturable through the production of a physical prototype. While the microstructure length scale was larger for the prototype than desired for clinical use, it proves that production is feasible with the continuing increases in resolution of additive manufacturing.

Some of the designs found for the bone prosthetic design problem examined in Chapter 4 made use of thin filament-like structures in the macroscopic design. Such small scale features suggest that the microstructure used was inappropriate and that the objective would benefit from using microstructures stiff in one direction while soft in another. Such a microstructure that can vary stiffness in different directions independently was explored in Chapter 5.

6.3 Multiparametric Microstructure Interpolation

In Chapter 5 we developed a microstructure set parameterised by the Young's moduli in the 3 axial directions, generalising the MIMO method. Such a parameterisation allows the microstructure to fulfil a role where different Young's moduli are required in different directions such as was found in Chapter 4. The stiffness tensors of the microstructures were also restricted so that the stiffness profile was monotonic and smoothly varying between the axes in order to allow control over the stiffness in non-axial directions. Without these further restrictions the stiffness in non-axial directions may change rapidly and irregularly throughout the microstructure set parameterisation.

As in Chapters 3 and 4 the final microstructure set was interpolated from key microstructures that were directly optimised. After optimising a single initial key microstructure, each key microstructure optimisation was initialised using a previously optimised, neighbouring key microstructure. The microstructures were rejected if the surface genus changed or if the constraints on the effective stiffness tensor were not satisfied. These restrictions were enough to ensure that the shape interpolation between the key microstructures was well behaved and produced smoothly changing effective elastic properties.

This anisotropic set was then used in the bone prosthetic optimisation problem examined in Chapter 4. An orthotropic cross structure was also used as a comparison. The broader search space clearly caused difficulties for the optimiser: while the microstructure sets used were in a sense generalisations of sets used in Chapter 4, the optimised multiparametric designs did not always improve upon the objectives obtained in Section 4.3. The implementation was thoroughly checked. When initialising the macroscopic, multiparametric optimisation with the results obtained in Chapter 4 the optimisation did no worse or improved upon objective values.

The multiparametric microstructure set developed in Chapter 5 is also amenable for use as a functionally graded material. The microstructure set can readily produce a desired functional gradient by inverting the parameter to effective material properties map. The power of the microstructure set is that it can have gradients for complementary material properties satisfied even if those gradients are not aligned, as shown in Section 5.5.

The microstructure set here is the first such set produced that is single scale, varying in multiple parameters, and has guaranteed smoothness and connective geometry. The method used to generate the set may be generalised to other material properties or microstructure families. For example, to generalise the closed cell, high modulus microstructure family used in Chapter 3, or develop a microstructure family with a range of conductivity or fluid flow properties.

6.4 Final Discussion

In this thesis we have developed, applied and extended the MIMO method. The method provided microstructure sets that vary smoothly in geometry and in microstructure properties, therefore solving the microstructure connectivity problem. A proof of concept was produced using additive manufacturing, demonstrating the viability of the method for producing physically realisable designs. The method is also very computationally efficient: the macroscopic optimisation problem can be scaled to have very high detail as no further homogenisation calculations are required once the microstructure set has been developed.

After optimisation and interpolation, the microstructure sets were used as the material for a macroscopic material distribution optimisation. In many cases using the interpolated microstructure provided a benefit to macroscopic optimisation objectives, particularly for two-dimensional compliance problems, and the bone prosthesis design problem. Two-dimensional problems are a natural fit for multiscale optimisation as designs can be produced from cutting sheet metal, a widespread manufacturing technique. In the case of the bone prosthesis problem, multiscale approaches are appropriate as the objective functions do not depend on stiffness or strength necessarily, but rather on load distribution. As such the efficiency of material used to produce stiff structures is not an immediate concern. The bone prosthetic problem also desires a monolithic structure with no large voids inside the optimisation domain. In such problems multiscale optimisation can provide the specified structural shape while still tailoring the elastic response to the problem at hand.

The method evaluation also produced some surprising results. Compliance problems in three dimensions saw little benefit over single scale designs, suggesting that a multiscale design may not be appropriate, or the microstructures used have too low stiffness to be economical. The microstructures produced may still be useful in the case where a monolithic design (with no large internal voids) is required. A disappointing result was that generalising to multiparametric microstructures did not always result in better objectives. This is an artefact of the macroscopic optimisation algorithm, highlighting the difficulties of benchmarking nonlinear optimisation methods.

In addition to being applicable to multiscale design, microstructure optimisation and interpolation was also shown to apply to the field of functionally graded materials. By using smoothly varying microstructure sets, desired effective properties can be achieved with microstructures from that set to give the properties required for functionally graded designs. We presented an example design with a prescribed E_z gradient perpendicular to a prescribed ν_{zx} gradient. The multiparametric microstructure set found in Chapter 5 was able to fulfil this design specification without modification.

The work in this thesis suggests further avenues of study. Microstructure sets here were optimised primarily for their elastic properties however the method would readily extend to producing microstructures optimised for conductance or fluid flow problems. In addition to generalisations, comparisons between multiscale optimisation methods would be of benefit to engineers; the results presented here hopefully provide enough detail for comparison. A study unifying the complex design space and objectives of Chanda et al. (2015b) with multiscale design such as by Arabnejad Khanoki and Pasini (2012) or in this thesis would also be of great interest, hopefully leading to practical prosthesis design recommendations. Finally, continued discussion and development of nonlinear optimisation algorithms for application to structural optimisation problems would provide benefits to the field of structural optimisation, both academics and practitioners, and ensure that our optimised designs are truly the best we can achieve.

Bibliography

N. Aage, E. Andreassen, and B. Lazarov. Topology optimization using PETSc: An easy-to-use, fully parallel, open source topology optimization framework. *Structural and Multidisciplinary Optimization*, pages 1–8, 2014. ISSN 1615-147X. doi: 10.1007/s00158-014-1157-0.

G. Allaire and F. Jouve. A level-set method for vibration and multiple loads structural optimization. *Computer Methods in Applied Mechanics and Engineering*, 194:2369–3290, 2005.

G. Allaire, F. Jouve, and A.-M. Toader. Structural optimization using sensitivity analysis and a level-set method. *Journal of Computational Physics*, 194(1):363–393, 2004.

G. Allaire, F. de Gournay, F. Jouve, and A.-M. Toader. Structural optimisation using topological and shape sensitivity via a level set method. *Control and Cybernetics*, 34(1):59–80, 2005.

S. Arabnejad Khanoki and D. Pasini. Multiscale design and multiobjective optimization of orthopedic hip implants with functionally graded cellular material. *Journal of biomechanical engineering*, 134:031004, 2012.

S. Arabnejad Khanoki and D. Pasini. Fatigue design of a mechanically biocompatible lattice for a proof-of-concept femoral stem. *Journal of the Mechanical Behavior of Biomedical Materials*, 22(0):65–83, 2013. ISSN 1751-6161. doi: 10.1016/j.jmbbm.2013.03.002. URL `http://www.sciencedirect.com/science/article/pii/S1751616113000805`.

S. Arabnejad Khanoki, B. Johnston, M. Tanzer, and D. Pasini. Fully porous 3d printed titanium femoral stem to reduce stress-shielding following total hip arthroplasty. *Journal of Orthopaedic Research*, 2016a.

S. Arabnejad Khanoki, R. B. Johnston, J. A. Pura, B. Singh, M. Tanzer, and D. Pasini. High-strength porous biomaterials for bone replacement: A strategy to assess the interplay between cell morphology, mechanical properties, bone ingrowth and manufacturing constraints. *Acta biomaterialia*, 30:345–356, 2016b. doi: 10.1016/j.actbio.2015.10.048.

S. Balay, W. D. Gropp, L. C. McInnes, and B. F. Smith. Efficient management of parallelism in object oriented numerical software libraries. In E. Arge, A. M. Bruaset, and H. P. Langtangen,

editors, *Modern Software Tools in Scientific Computing*, pages 163–202. Birkhäuser Press, 1997.

S. Balay, S. Abhyankar, M. F. Adams, J. Brown, P. Brune, K. Buschelman, L. Dalcin, V. Eijkhout, W. D. Gropp, D. Kaushik, M. G. Knepley, L. C. McInnes, K. Rupp, B. F. Smith, S. Zampini, H. Zhang, and H. Zhang. PETSc users manual. Technical Report ANL-95/11 - Revision 3.7, Argonne National Laboratory, 2016. URL `http://www.mcs.anl.gov/petsc`.

M. P. Bendsøe. Optimal shape design as a material distribution problem. *Structural Optimization*, 1(4):193–202, 1989.

M. P. Bendsøe and N. Kikuchi. Generating optimal topologies in structural design using a homogenization method. *Computer methods in applied mechanics and engineering*, 71(2): 197–224, 1988.

M. P. Bendsøe and O. Sigmund. Material interpolation schemes in topology optimization. *Archive of Applied Mechanics*, 69(9-10):635–654, 1999.

M. P. Bendsøe and O. Sigmund. *Topology optimization: theory, methods and applications*. Springer Verlag, 2003.

V. Birman and L. W. Byrd. Modeling and analysis of functionally graded materials and structures. *Appl. Mech. Rev.*, 60(5):195–216, Sept. 2007. doi: 10.1115/1.2777164.

B. D. Boyan, T. W. Hummert, D. D. Dean, and Z. Schwartz. Role of material surfaces in regulating bone and cartilage cell response. *Biomaterials*, 17(2):137–146, 1996.

D. E. Breen and R. T. Whitaker. A level-set approach for the metamorphosis of solid models. *Visualization and Computer Graphics, IEEE Transactions on*, 7(2):173–192, 2001.

H. Camron, R. Pilliar, and I. Macnab. The rate of bone ingrowth into porous metal. *Journal of biomedical materials research*, 10(2):295–302, 1976.

V. Challis, A. Roberts, and A. Wilkins. Design of three dimensional isotropic microstructures for maximized stiffness and conductivity. *International Journal of Solids and Structures*, 45 (14):4130–4146, 2008a.

V. J. Challis. *Multi-Property Topology Optimisation with the Level-Set Method*. PhD thesis, The University of Queensland, 2009.

V. J. Challis, A. P. Roberts, and A. H. Wilkins. Fracture resistance via topology optimization. *Structural and Multidisciplinary Optimization*, 36(3):263–271, 2008b.

V. J. Challis, A. P. Roberts, and J. F. Grotowski. High resolution topology optimization using graphics processing units (gpus). *Structural and Multidisciplinary Optimization*, 49(2): 315–325, 2014a.

V. J. Challis, X. Xu, L. C. Zhang, A. P. Roberts, J. F. Grotowski, and T. B. Sercombe. High specific strength and stiffness structures produced using selective laser melting. *Materials and Design*, 63:783–788, 2014b.

S. Chanda, S. Gupta, and D. K. Pratihar. Effects of interfacial conditions on shape optimization of cementless hip stem: an investigation based on a hybrid framework. *Structural and Multidisciplinary Optimization*, pages 1–13, 2015a. doi: 10.1007/s00158-015-1382-1.

S. Chanda, S. Gupta, and D. K. Pratihar. A genetic algorithm based multi-objective shape optimization scheme for cementless femoral implant. *Journal of biomechanical engineering*, 137(3):034502, 2015b. doi: 10.1115/1.4029061.

P. G. Coelho, P. R. Fernandes, J. M. Guedes, and H. C. Rodrigues. A hierarchical model for concurrent material and topology optimisation of three-dimensional structures. *Structural and Multidisciplinary Optimization*, 35(2):107–115, 2008.

A. D. Cramer, V. J. Challis, and A. P. Roberts. Microstructure interpolation for macroscopic design. *Structural and Multidisciplinary Optimization*, 53(3):489–500, 2016. ISSN 1615-147X. doi: 10.1007/s00158-015-1344-7.

A. D. Cramer, V. J. Challis, and A. P. Roberts. Physically realizable three-dimensional bone prosthesis design with interpolated microstructures. *J. Biomech. Eng.*, 139(3):031013, 2017. doi: 10.1115/1.4035481.

J. Deng, J. Yan, and G. Cheng. Multi-objective concurrent topology optimization of thermoelastic structures composed of homogeneous porous material. *Structural and Multidisciplinary Optimization*, 47:583–597, 2013.

P. D. Dunning, B. K. Stanford, H. A. Kim, and C. V. Jutte. Aeroelastic tailoring of a plate wing with functionally graded materials. In *55th AIAA/ASME/ASCE/AHS/ASC Structures, Structural Dynamics, and Materials Conference*, 2014. doi: 10.2514/6.2014-0344.

C. A. Engh, T. McGovern, J. Bobyn, and W. H. Harris. A quantitative evaluation of periprosthetic bone-remodeling after cementless total hip arthroplasty. *J Bone Joint Surg Am*, 74 (7):1009–1020, 1992.

H. A. Eschenauer, V. V. Kobelev, and A. Schumacher. Bubble method for topology and shape optimization of structures. *Structural optimization*, 8(1):42–51, 1994.

M. Fraldi, L. Esposito, G. Perrella, A. Cutolo, and S. Cowin. Topological optimization in hip prosthesis design. *Biomechanics and modeling in mechanobiology*, 9(4):389–402, 2010. doi: 10.1007/s10237-009-0183-0.

L. J. Gibson. The hierarchical structure and mechanics of plant materials. *J. R. Soc. Interface*, 9(76):2749–2766, 2012. doi: 10.1098/rsif.2012.0341.

J. K. Guest and J. H. Prévost. Optimizing multifunctional materials: design of microstructures for maximized stiffness and fluid permeability. *International Journal of Solids and Structures*, 43(22):7028–7047, 2006.

B. Hackl. Methods for reliable topology changes for perimeter-regularized geometric inverse problems. *SIAM Journal on Numerical Analysis*, 45(5):2201–2227, jan 2007. doi: 10.1137/060652208.

R. T. Haftka and R. V. Grandhi. Structural shape optimization — a survey. *Computer Methods in Applied Mechanics and Engineering*, 57:91–106, 1986.

Z. Hashin and S. Shtrikman. A variational approach to the theory of the elastic behaviour of multiphase materials. *Journal of the Mechanics and Physics of Solids*, 11(2):127–140, 1963.

T. He, S. Wang, and A. Kaufman. Wavelet-based volume morphing. In *Proceedings of the Conference on Visualization '94*, VIS '94, pages 85–92, Los Alamitos, CA, USA, 1994. IEEE Computer Society Press. ISBN 0-7803-2521-4.

W. C. Head, D. J. Bauk, and R. H. Emerson Jr. Titanium as the material of choice for cementless femoral components in total hip arthroplasty. *Clinical Orthopaedics and Related Research*, 311:85–90, 1995.

O. Hoffman. The brittle strength of orthotropic materials. *Journal of Composite Materials*, 1 (2):200–206, 1967. doi: 10.1177/002199836700100210.

S. J. Hollister and W. L. Murphy. Scaffold translation: barriers between concept and clinic. *Tissue Engineering Part B: Reviews*, 17(6):459–474, 2011.

C. S. Jog, R. B. Haber, and M. P. Bendsøe. Topology design with optimized, self-adaptive materials. *International Journal for Numerical Methods in Engineering*, 37(8):1323–1350, 1994.

L. Krog, A. Tucker, M. Kemp, and R. Boyd. Topology optimization of aircraft wing box ribs. In *Proc. of the 10th AIAA/ISSMO MAO Conference, Albany*, 2004.

J. Kuiper and R. Huiskes. Mathematical optimization of elastic properties: application to cementless hip stem design. *Journal of biomechanical engineering*, 119(2):166–174, 1997.

H. Li, Z. Luo, N. Zhang, L. Gao, and T. Brown. Integrated design of cellular composites using a level-set topology optimization method. *Computer methods in applied mechanics and engineering*, 309:453–475, 2016. doi: 10.1016/j.cma.2016.06.012.

A. E. H. Love. *A treatise on the mathematical theory of elasticity*. Cambridge University Press, 1944.

H. Malchau, P. Herberts, T. Eisler, G. Garellick, and P. Söderman. The swedish total hip replacement register. *The Journal of Bone & Joint Surgery*, 84(suppl 2):S2–S20, 2002. ISSN 0021-9355.

A. Michell. The limits of economy of material in frame-structures. *Philosophical Magazine*, 8 (47):589–597, 1904.

K. Michielsen and D. Stavenga. Gyroid cuticular structures in butterfly wing scales: biological photonic crystals. *Journal of The Royal Society Interface*, 5(18):85–94, 2008.

D. J. Munk, G. A. Vio, and G. P. Steven. Topology and shape optimization methods using evolutionary algorithms: a review. *Structural and Multidisciplinary Optimization*, pages 1–19, 2015. doi: 10.1007/s00158-015-1261-9.

M. Niino and S. Maeda. Recent development status of functionally gradient materials. *ISIJ International*, 30(9):699–703, 1990.

A. N. Norris. A differential scheme for the effective moduli of composites. *Mechanics of Materials*, 4(1):1–16, 1985. doi: http://dx.doi.org/10.1016/0167-6636(85)90002-X.

S. Osher and R. Fedkiw. *Level set methods and dynamic implicit surfaces*, volume 153. Springer Science & Business Media, 2006.

S. J. Osher and F. Santosa. Level set methods for optimization problems involving geometry and constraints: I. frequencies of a two-density inhomogeneous drum. *Journal of Computational Physics*, 171(1):272–288, 2001.

O. Querin, G. Steven, and Y. Xie. Evolutionary structural optimisation (eso) using a bidirectional algorithm. *Engineering Computations*, 15(8):1031–1048, 1998. doi: dx.doi.org/10.1108/02644409810244129.

A. Radman, X. Huang, and Y. M. Xie. Topology optimization of functionally graded cellular materials. *Journal of Materials Science*, 48:1503–1510, 2013.

S. P. Raya and J. K. Udupa. Shape based interpolation of multidimensional objects. *IEEE Transactions on Medical Imaging*, 9(1):32–42, 1990.

H. Rodrigues, J. M. Guedes, and M. Bendsoe. Hierarchical optimization of material and structure. *Structural and Multidisciplinary Optimization*, 24(1):1–10, 2002.

G. Rozvany. Aims, scope, methods, history and unified terminology of computer-aided topology optimization in structural mechanics. *Structural and Multidisciplinary Optimization*, 21(2): 90–108, 2001.

G. I. N. Rozvany, M. Zhou, and T. Birker. Generalized shape optimization without homogenization. *Structural Optimization*, 4(3-4):250–252, 1992.

G. I. N. Rozvany, T. Lewinski, O. M. Querin, and J. Logo. Quality control in topology optimization using analytically derived benchmarks. In *11th AIAA/ISSMO multidisciplinary analysis and optimization conference*, pages 6–8, 2006.

J. A. Sethian. *Level set methods and fast marching methods.* Cambridge University Press, Cambridge, 1999. ISBN 0 521 64557 3.

J. A. Sethian and A. Weigmann. Structural boundary design via level set and immersed interface methods. *J. Comput. Phys.*, 163:489–528, 2000. doi: 10.1006/jcph.2000.6581.

S. Shepherd, M. Avalos-Borja, and M. O. Quintanilla. Toward a chronology of haliotis fulgens, with a review of abalone shell microstructure. *Marine and freshwater research*, 46(3):607–615, 1995.

O. Sigmund. Materials with prescribed constitutive parameters: An inverse homogenization problem. *International Journal of Solids and Structures*, 31(17):2313–2329, 1994. ISSN 0020-7683. doi: http://dx.doi.org/10.1016/0020-7683(94)90154-6. URL `http://www.sciencedirect.com/science/article/pii/0020768394901546`.

O. Sigmund. Tailoring materials with prescribed elastic properties. *Mechanics of Materials*, 20 (4):351–368, 1995.

O. Sigmund. On the design of compliant mechanisms using topology optimization*. *Journal of Structural Mechanics*, 25(4):493–524, 1997.

O. Sigmund. A new class of extremal composites. *Journal of the Mechanics and Physics of Solids*, 48(2):397–428, 2000. doi: http://dx.doi.org/10.1016/S0022-5096(99)00034-4.

R. Sivapuram, P. D. Dunning, and H. A. Kim. Simultaneous material and structural optimization by multiscale topology optimization. *Structural and Multidisciplinary Optimization*, pages 1–15, 2016. doi: 10.1007/s00158-016-1519-x.

K. Svanberg. The method of moving asymptotesŮa new method for structural optimization. *International journal for numerical methods in engineering*, 24(2):359–373, 1987.

K. Svanberg. A class of globally convergent optimization methods based on conservative convex separable approximations. *SIAM journal on optimization*, 12(2):555–573, 2002.

O. Tange. Gnu parallel - the command-line power tool. *;login: The USENIX Magazine*, 36(1): 42–47, Feb 2011. URL `http://www.gnu.org/s/parallel`.

S. Torquato and A. Donev. Minimal surfaces and multifunctionality. *Proceedings of the Royal Society of London A: Mathematical, Physical and Engineering Sciences*, 460(2047):1849–1856, 2004. doi: 10.1098/rspa.2003.1269.

S. B. Vigdergauz. Energy-minimizing inclusions in a planar elastic structure with macroisotropy. *Structural Optimization*, 17(2-3):104–112, 1999.

M. Y. Wang, X. Wang, and D. Guo. A level set method for structural topology optimization. *Computer methods in applied mechanics and engineering*, 192(1):227–246, 2003.

Y. Wang, F. Chen, and M. Y. Wang. Concurrent design with connectable graded microstructures. *Computer Methods in Applied Mechanics and Engineering*, 2016.

M. Williams. Stress singularities resulting from various boundary conditions. *Journal of Applied Mechanics*, 19(4):526–528, 1952.

Y. Xie and G. P. Steven. A simple evolutionary procedure for structural optimization. *Computers & structures*, 49(5):885–896, 1993. doi: 10.1016/0045-7949(93)90035-C.

Y. M. Xie and G. P. Steven. Optimal design of multiple load case structures using an evolutionary procedure. *Engineering Computations*, 11(4):295–302, 1994. doi: 10.1108/02644409410799290.

X. Y. Yang, X. Huang, Y. M. Xie, Q. Li, and J. H. Rong. Topology optimization of composite materials with optimal stiffness and thermal conductivity. *International Journal of Optimization in Civil Engineering*, 3:397–417, 2011.

L. Zhang, D. Klemm, J. Eckert, Y. Hao, and T. Sercombe. Manufacture by selective laser melting and mechanical behavior of a biomedical ti–24nb–4zr–8sn alloy. *Scripta Materialia*, 65(1):21–24, 2011.

X. Zheng, H. Lee, T. H. Weisgraber, M. Shusteff, J. Deotte, E. B. Duoss, J. D. Kuntz, M. M. Biener, Q. Ge, J. A. Jackson, S. O. Kucheyev, N. X. Fang, and C. M. Spadaccini. Ultralight, ultrastiff mechanical metamaterials. *Science*, 344:1373 – 1377, 2014.

S. Zhou and Q. Li. Design of graded two-phase microstructures for tailored elasticity gradients. *Journal of Materials Science*, 43(15):5157–5167, 2008a.

S. Zhou and Q. Li. Microstructural design of connective base cells for functionally graded materials. *Materials Letters*, 62(24):4022–4024, 2008b.

S. Zhou, W. Li, Y. Chen, G. Sun, and Q. Li. Topology optimization for negative permeability metamaterials using level-set algorithm. *Acta Materialia*, 59:2624–2636, 2011. doi: 10.1016/j.actamat.2010.12.049.